Tailoring molecule nanostructures on insulating surfaces investigated by non-contact atomic force microscopy

Felix Loske
geboren in Bremen

Dissertation zur Erlangung des Grades
"Doktor der Naturwissenschaften"
im Promotionsfach Physikalische Chemie
am Fachbereich Chemie, Pharmazie und Geowissenschaften
der Johannes Gutenberg-Universität in Mainz

Mainz, Februar 2011

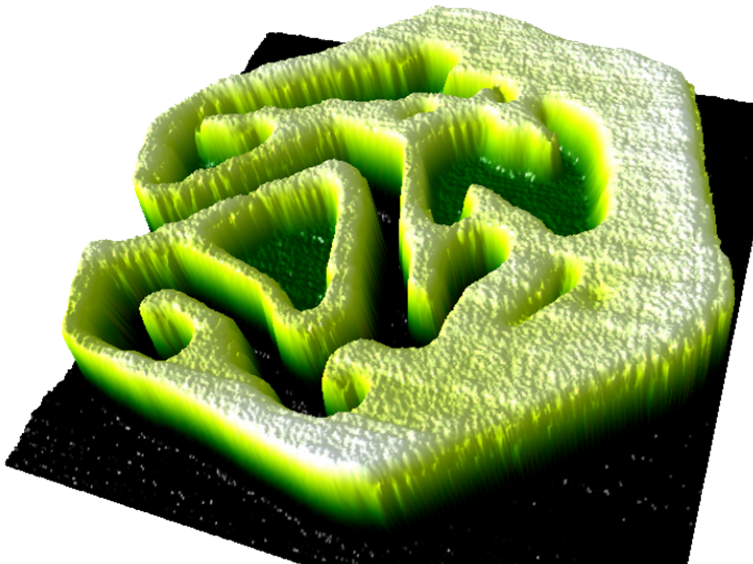

This dissertation was supervised by and was carried out at the Universität Osnabrück and the Johannes Gutenberg-Universität Mainz from April 2008 to February 2011.

D77 (dissertation Johannes Gutenberg-Universität Mainz)

dean of the faculty

1st report

2nd report

Submitted: February 2011
Oral examination: 24. March 2011

Für meine Eltern und Geschwister.

Contents

1 Introduction

This work contributes to understand the assembly of molecules on non-conductive substrate surfaces and to develop strategies to control the molecular ordering.

Through an eligible formation and ordering of molecules at surfaces, materials with novel properties and functions can be created.[1,2] A very appealing motivation is to adopt molecules as building blocks for molecular electronics for further miniaturization of electronic devices, as conventional, silicon-based manufacturing techniques have reached their resolution limit.[2,3]

To create functional structures on surfaces, two different approaches are open to explore.[1] The top-down approach is a well established and widely used technique to create structures at the nanometer scale, e.g., by lithography methods. However, top-down methods need an external control to direct the assembly. This limits the complexity and size of producible structures. In contrast, the bottom-up approach allows for more complex and smaller structures to be formed. The most direct bottom-up method is to build structures molecule-by-molecule. Thereto, a small tip at the nanometer scale is used to move particles on the surface.[4–6] However, employing this technique, the assembly of large structures is elaborate and time-consuming. Thus, instead of manually building the structures, a more practical bottom-up strategy is to exploit the intermolecular interactions and let the molecules autonomously assemble themselves. Utilizing this so-called molecular self-assembly,[7,8] manifold and complex structures have been fabricated on various surfaces, mainly metal substrate surfaces.[9] However, for the application of self-assembled structures, e.g., in molecular electronics, an insulating substrate surface is necessary. To investigate the ordering of molecules on insulating substrate surfaces in real space, non-contact atomic force microscopy (NC-AFM)[10,11] is the method of choice. NC-AFM images the surface force field and allows for high-resolution imaging at the subnanometer scale.

There's Plenty of Room at the Bottom
Richard P. Feynman

Thereto, within this thesis, NC-AFM was facilitated to investigate self-assembled molecular structures on insulating substrate surfaces. Both, sub-

strate preparation and molecule deposition, took place under a contamination-free environment (ultra-high vacuum, UHV).

The self-assembly of C_{60} molecules on two surfaces was explored. First, C_{60} molecules were investigated on the TiO_2 (110) surface. This surface exhibits parallel running troughs at the nanometer scale, which strongly steer the assembly of the molecules. This is in contrast to the second investigated surface. The CaF_2 (111) surface is atomically flat and the molecular assembly was observed to be far less affected by the surface. On this particular surface, molecular diffusion and island formation was quantitatively and qualitatively investigated at various temperatures. Compared to molecular self-assembly on metal surfaces, distinctly different island shapes were observed. This qualitative difference can be understood by an increased ability of the molecules to dewet from the insulating surface. Based on experimental evidences and theoretical considerations, a comprehensive picture of the processes responsible for the island formation of C_{60} molecules on this insulating surfaces was developed. This allows to further understand and exploit self-assembly techniques in structure fabrication on insulating substrate surfaces. To alter island formation and island structure, C_{60} molecules were codeposited with second molecule species (PTCDI and SubPc) on the CaF_2 (111) surface. Depending on the order of deposition, quiet different structures were observed to arise. Codeposition has not been investigated on insulating substrates yet. Thus, these are the first steps towards more complex functional arrangements consisting of two molecule species on insulating surfaces.

2 Non-contact atomic force microscopy

Contents

Non-contact atomic force microscopy (NC-AFM) is a comparatively new, non-destructive surface analysis tool.[10,11] The surface is scanned by a small tip, which probes the forces acting between the tip and the surface at every sampling point. This measurement is performed with a flexible cantilever with a small tip at the very end, which is excited to oscillate at its resonance frequency. In close proximity to the surface, the interaction between tip and surface changes the resonance frequency. In the frequency modulation mode, which will be exclusively discussed here, this shift in resonance frequency is the main measurement parameter, reflecting tip-sample forces. It is important to note that the surface force field does not necessarily correspond to the atomic surface topography. Unlike scanning tunneling microscopy (STM), NC-AFM is not limited to conductive surfaces and can, therefore, be applied to almost every surface. However, achieving atomic resolution with NC-AFM is rather demanding with respect to both, environment (usually ultra-high vacuum) and materials (i.e. cantilevers). In contrast, using STM atomic resolution is usually easily obtained even under ambient conditions.

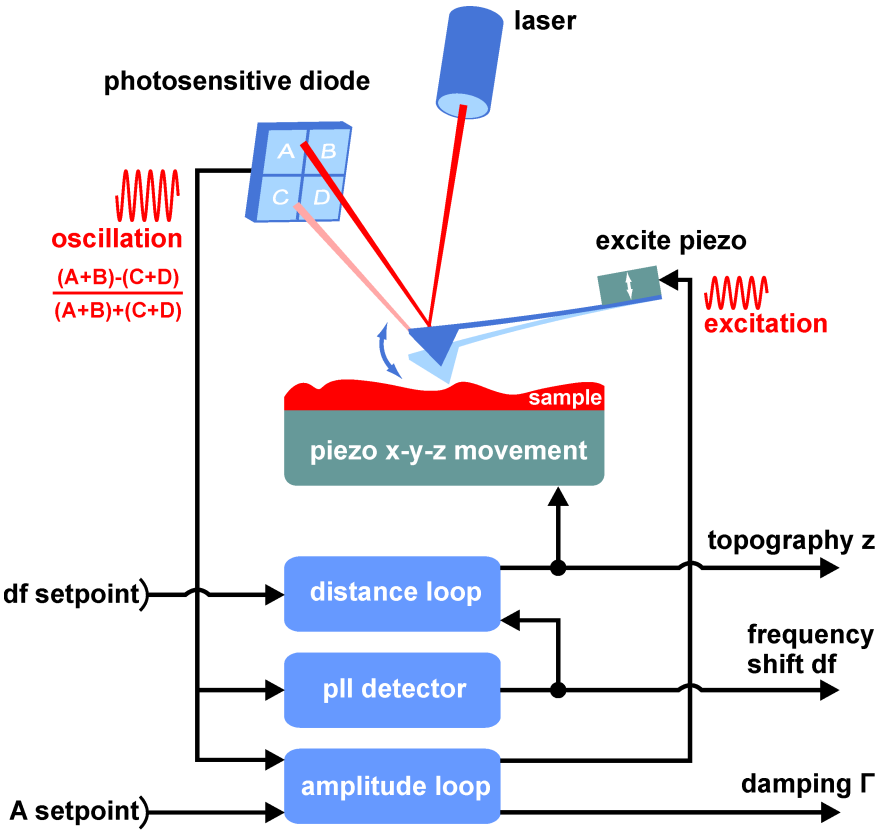

Figure 2.1: Working principal of NC-AFM in the frequency modulation mode.

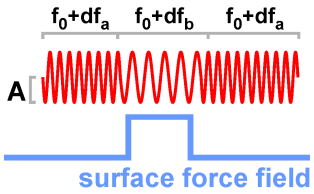

Figure 2.2: In the frequency modulation mode the current resonance frequency is shifted (frequency shift), depending on the surface force field. The amplitude of the cantilever's oscillation is kept constant, accomplished by a feedback loop.

2.1 Working principle

For NC-AFM, a silicon cantilever is mounted with one end to a piezo crystal and excited to oscillate at its resonance frequency with a constant amplitude (Fig. 2.1).

At the free end, a small etched tip is located. This tip points towards the substrate and probes the surface force field. The tip scans over the surface in close proximity, with the cantilever's resonance frequency changing according to the substrate force field, due to the interaction between the tip and surface (Fig. 2.2). The difference between the resonance frequency of the free oscillating cantilever f_0 and the current resonance frequency over a sampling point is referred to as *frequency shift*, with the abbreviation *df*. In the frequency modulation mode, this shift in resonance frequency is the main measurement parameter in NC-AFM.[11] In Fig. 2.2 the change in the momentary resonance frequency over a corrugated surface force field is shown. At the protrusion the resonance frequency is lowered by frequency shift $df_b < 0$ due to stronger attractive interaction between the tip and the surface. On both sites of the protrusion, the resonance frequency is only lowered by a frequency shift $0 > df_a > df_b$ due to a less attractive

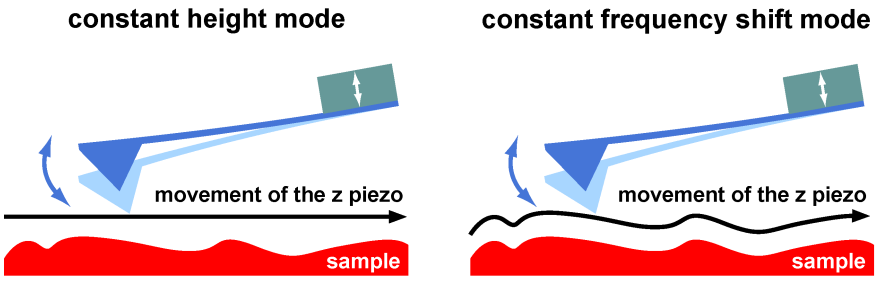

Figure 2.3: The two different modes in NC-AFM. In constant-height mode (left), the distance between tip and surface is not regulated by the distance feedback loop. Therefore, no contrast appears in the z-channel, but in the *df*-channel. In constant frequency shift mode (right), the distance feedback regulates the distance between tip and sample in a way that the measured frequency shift is kept constant at the *df* setpoint. Consequently, no contrast appears in the *df*-channel, but in the z-channel.

interaction. In this way, the surface force field is visualized. More details on the evolution of the frequency shift can be found in Refs. 12,13.

For the detection of the frequency shift, a laser points towards the end of the cantilever and is reflected to a photosensitive diode.[14,15] This photosensitive diode is usually divided into four quadrants. Vertical deflections of the cantilever can be obtained from the combination $((A + B) - (C + D)) / ((A + B) + (C + D))$ of the quadrant signals. The signal is forwarded to a phase-locked-loop (PLL) detector, which produces a voltage proportional to the difference of the frequency of the incoming signal (which is the current cantilever oscillation) and the frequency of the free oscillation, this is the frequency shift *df*. The signal from the photosensitive diode is also used for the amplitude control. A feedback loop unit assures that the cantilever always oscillates with a constant amplitude. The frequency shift is used as control variable for the distance loop. Operating in *constant-df* mode, the distance loop regulates the tip surface distance through a feedback loop unit with proportional and integral gain, keeping the frequency shift constant. Therefore, all information about the surface force field is stored in the topographic channel (Fig. 2.3).

True constant-df mode imaging is basically impossible, since the feedback loop is not always able to follow the surface force field immediately. In the *constant-height* mode, the distance loop is switched off and the information about the surface force field is stored in the *df*-channel. In a real measurement, however, usually a combination of both modes is at work.

2.2 Forces between tip and sample

The changes in resonance frequency are caused by the interaction between the tip and sample. The interactions can be roughly divided in short- and long-range forces. The goal of NC-AFM is to measure the short-range forces, as those allow for atomic resolution imaging.

Long-range forces

Van-der-Waals forces belong to the class of long-range forces. They are due to an electrostatic interaction of permanent and induced dipole moments in the tip and sample. If a temporary dipole moment is formed, this dipole moment can induce further dipoles and interacts with them. Van-der-Waals forces are always attractive under vacuum conditions. The interaction potential between two fluctuating dipoles falls with z^{-6}.[16–18]

Another long-range force is the electrostatic interaction. Electrostatic interaction between the tip and sample can be due to trapped substrate charges or, in general, due to a charged surface or tip. The electrostatic potential is proportional to z^{-1}. If tip and sample possess metallic character and are electronically connected, also the difference in the work functions (contact potential difference) contributes to the electrostatic forces. This effect, which is comparable to a capacitor, can be compensated using an appropriate bias voltage applied between tip and sample.[19] This is also applicable to insulators, but here macroscopic surface charges are compensated by the applied bias voltage. The tip geometry has also a great influence on the long-range forces and more adequate, but complex interaction terms can be found in Ref. 20. Furthermore, magnetic and capillary forces are of long-range character, but are not discussed here as they have no relevance for the present thesis.

Short-range forces

Short-range chemical forces are due to an overlap of electron orbitals of tip and surface atoms. They can be either attractive or repulsive, depending on the distance between tip and sample. For large separations, no chemical interaction exist, since the electron orbitals do not overlap. With decreasing distance the electron orbitals begin to overlap and an attractive force acts due to an energy gain from filling the bonding molecular orbitals. If the orbitals overlap even more with decreasing distance, the force gets repulsive due to Pauli repulsion from the Pauli exclusion principle.

Moreover, short-range forces can be of electrostatic nature. The short-range electrostatic forces strongly depend on the ionic tip termination at the very end of the tip. Thus, for an eligible tip, the contrast can be ruled by the microscopic electrostatic interactions, as interpreted e.g. for the

contrast formation on the TiO_2 (110) (Sec. 5.1) and CaF_2 (111) (Sec. 5.2) surface. Thus, different tip terminations result in different contrasts on the very same surface.

Units

$[V]$	=	eV
$[\epsilon]$	=	eV
$[z]$	=	m
$[z_0]$	=	m
$[f_0]$	=	Hz
$[\Delta f]$	=	Hz
$[k]$	=	$N\,m^{-1}$
$[m]$	=	kg

Total force

Both, the long-range and the short-range interactions contribute to the total force. An approximation for the interaction between two uncharged atoms, which are not covalently bound, is the *Lennard-Jones potential*. Different variations of the Lennard-Jones potential exist with respect the short-range term, but the following equation is the most common form[21]

$$V(z) = -\epsilon\left[2\left(\frac{z_0}{z}\right)^6 - \left(\frac{z_0}{z}\right)^{12}\right] \tag{2.1}$$

with z_0 being the equilibrium distance at the energy ϵ and z denoting the tip-to-sample separation. The equilibrium distance z_0 is typically about a few tenth of nanometers. The attractive part $\propto z^{-6}$ corresponds to the long-range Van-der-Waals potential and dominates the total potential at large distances. The repulsive part $\propto z^{-12}$ corresponds to the chemical interaction and dominates at small distances. Fig. 2.4 shows the combined total potential, the force and the force gradient.

If the cantilever oscillates in the non-contact regime, it experiences a force and, therefore, its resonance frequency is shifted due to a change of the effective potential (harmonic oscillator plus tip-surface interaction energy) in which the cantilever oscillates. The resonance frequency of the

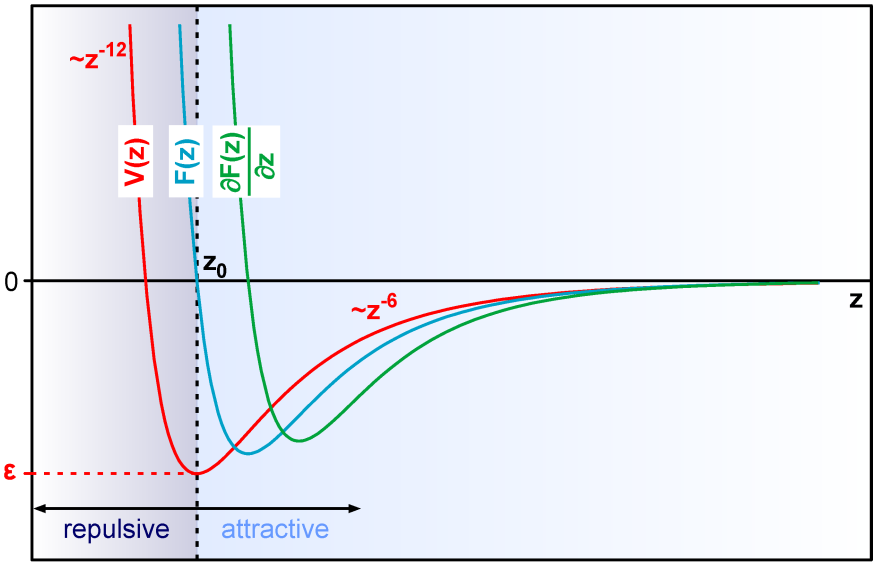

Figure 2.4: Interaction potential between two uncharged atoms, which are not covalently bound, and its first and second derivation, corresponding to force and force gradient. Equilibrium distance z_0 at the energy ϵ (see Lennard-Jones potential).

free oscillating cantilever is given by[12]

$$f_0 = \frac{1}{2\pi}\sqrt{\frac{k}{m}} \tag{2.2}$$

with k being the spring constant and m being the effective mass of the cantilever. When the tip interacts with the surface, the spring constant k in Eqn. 2.2 is substituted by an effective term, which is the sum of the original spring constant and a force gradient $k_{ts} = \partial^2 V/\partial z^2$ equivalent to the tip-sample interaction. Thus, the shift in the resonance frequency reads[12]

$$\Delta f = f_0 - \frac{1}{2\pi}\sqrt{\frac{k + k_{ts}}{m}} \tag{2.3}$$

The additional term k_{ts} may not be constant for the whole cantilever's oscillation cycle. In particular, the evolution of k_{ts} is dependent on the oscillation amplitude, the tip-sample separation and the particular tip-surface interaction potential. More elaborated considerations will not be presented here, but can be found in Ref. 12.

3 Experimental setup

Figure 3.1: (a) Omicron VT AFM 25 system.[22] (b) RHK UHV 750 system. Both system consist of a load lock Ⓐ, a preparation chamber Ⓑ and a measurement chamber Ⓒ.

Experiments are performed under ultra-high vacuum (UHV) conditions, with a base pressure better than 10^{-10} mbar. The UHV is generated and maintained with momentum transfer pumps (i.e. turbomolecular pumps in combination with rotary vane pumps) and entrapment pumps (i.e. ion pumps, titanium sublimation pumps and sorption pumps). To remove water and other adsorbed species from the inner walls of the UHV components, the system is once baked out at a temperature between 373 K and 423 K. Samples and tips are introduced through a load lock into the UHV system in order to maintain the UHV.

Two different UHV systems (Omicron VT AFM 25 and RHK UHV 750) are used for the experiments presented within this thesis, both consisting of a preparation chamber and a measurement chamber (Fig. 3.1). To reduce environmental vibrations, the systems are placed on air-damped vibrational-isolator legs. Tips and samples introduced into the UHV system are moved using a linear manipulator in both chambers. The manipulator can either be cooled by liquid nitrogen flow or heated with an embedded filament. Because samples are in thermal contact to the manipulator, they can be kept at different temperatures during preparation. For various treatments of tips and samples in the preparation chamber, the manipulator

is positioned in front of the eligible equipment. Using a sputter gun, contaminations or surface layers can be removed from tips and surfaces (e.g. TiO_2 in Sec. 5.1) by momentum transfer of accelerated Ar^+ ions. Brittle crystals can be cleaved to generate a clean surface. Thereto, both chambers are equipped with a sharp blade to scratch the side of a well-aligned crystal until the upper part breaks apart (e.g. CaF_2 in Sec. 5.2). Moreover, samples can be heated to remove surface contaminations or, at higher temperatures, induce a special reconfiguration/reconstruction of the sample's surface (e.g. TiO_2 and CaF_2 in Sec. 5.1 and Sec. 5.2, respectively). Heating of samples is accomlished either using the embedded heater of the manipulator or a resistive heating filament in the sample holder. On cleaned surfaces selected atomic or molecular species can be deposited, e.g. by sublimation (see Sec. 6.1).

Once tips and samples have been properly treated in the preparation chamber, they are transferred to the measurement chamber. In this chamber the AFM is situated, which holds a tip and sample for NC-AFM measurements (see Sec. 2). To minimize mechanical vibrations, the AFM is decoupled from the circumjacent UHV system using eddy current damping. Samples can also be cooled in the AFM, so that a sample prepared at low temperatures is continuously cooled.

Both systems are equipped with a phase-locked loop controller for frequency shift detection in the frequency modulation non-contact mode (easyPLL Plus (Nanosurf, Liestal, Switzerland) and RHK PLLpro (RHK, Troy, USA)). For NC-AFM imaging, silicon cantilevers (PPP-NCH Nanosensors, Neuchâtel, Switzerland) with resonance frequencies of about 300 kHz / 75 kHz and typical quality factors of 30,000 / 100,000 are excited to oscillations with an amplitude of 10 nm. Tips are Ar^+ ion sputtered (1 keV, 5 min) to remove contaminants. In order to minimize long-range electrostatic interactions, an appropriate bias voltage is applied to the tip. The compensating voltage is determined via Kelvin probe force spectroscopy.[23] Depending on the distance feedback loop settings, either constant frequency shift (z contrast) or constant height images (*df* contrast) are taken.[24]

Device-specific details about the mechanical cooling junctions, the cooling processes itself, the geometrical arrangements of devices and the modifications on the systems (especially the electronics) can be found in Refs. 25,26 for the Omicron VT AFM 25 system and in Ref. 27 for the RHK UHV 750 system.

4 Diffusion, nucleation and growth of molecules on surfaces

Contents

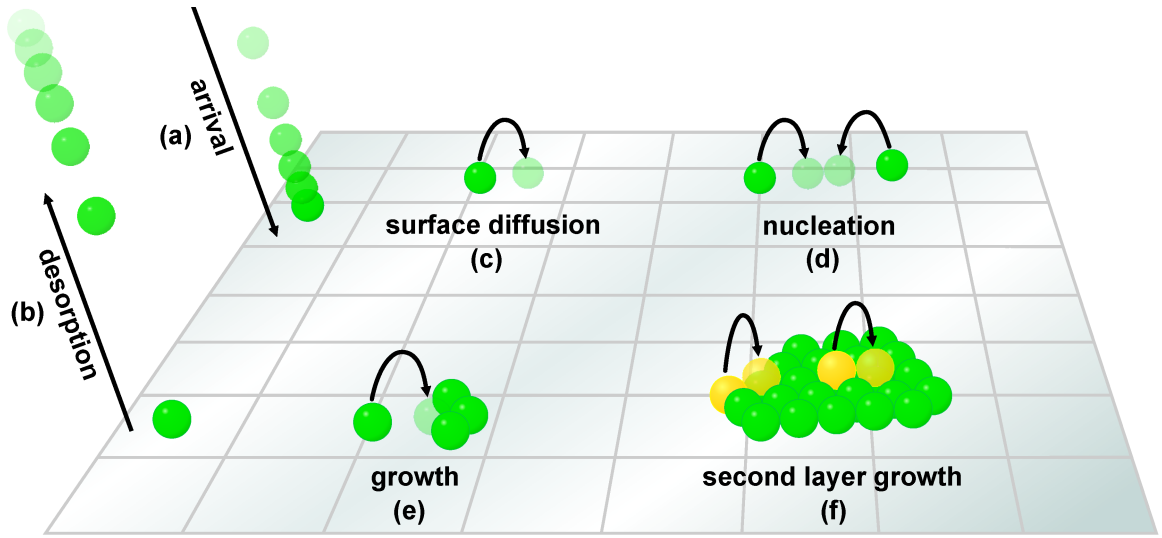

Investigating the arrangement of molecules on surfaces requires a closer inspection of the diffusion and nucleation processes both in a qualitative as well as quantitative manner.

Figure 4.1: Processes of diffusion and nucleation. Description in the main text.

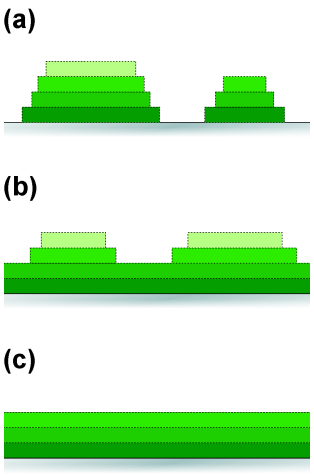

Figure 4.2: Examples for an island, layer-plus-island and layer-by-layer growth, respectively (a), (b) and (c). Each green-colored bar represents a single layer.

The processes playing a role for the diffusion, nucleation and growth of molecules on surfaces are summarized in Fig. 4.1.[28,29] Molecules deposited (e.g. by sublimation from a glass crucible) onto a surface may have the possibility to desorb again or diffuse on the surface, see (a), (b) and (c), respectively. If diffusion happens at a sufficient rate on the surface, two or more molecules can meet at adjacent sites, forming a cluster, e.g. a dimer in (d). Such clusters can either grow by capture of further molecules (see (e)) or decay by detachment of molecules. The growth is not restricted to two dimensions, but molecules can be transported to higher layers, resulting in a three dimensional morphology, like in (f). In general, also dimers and larger clusters are mobile on the surface, but the mobility decays rapidly with increasing cluster size. At high coverages, clusters can coalesce.

Three different growth modes can be distinguished at coverages exceeding one monolayer.[30] In the *island growth* mode (so-called *Volmer-Weber growth*) the transport of molecules to higher layers is favored, resulting in rough multi-layer films (Fig. 4.2(a)). This growth mode is often evident for organic molecules on insulating surfaces, reflecting a much smaller molecule-substrate interaction in comparison to the intermolecular interaction. In contrary, a stronger molecule-substrate interaction favors the *layer-by-layer growth* (so-called *Frank-van der Merwe growth*, Fig. 4.2(c)). Molecules preferentially attach to surface sites forming complete layers. The third mode is the *layer-plus-island growth* (so-called *Stranski-Krastanov growth*, Fig. 4.2(b)). It is an intermediary growth process. Initially, up to several complete layers grow in a layer-by-layer fashion. On top, the molecules grow in an island mode.

The morphology and spatial distribution of molecular arrangements is steered by the experimental conditions (e.g. temperature) as well as intrinsic properties of the molecule-substrate system (e.g. diffusion barrier). The challenging task in exploiting molecular self-assembly is to choose the appropriate molecule-substrate system, prepared and isolated under beneficial conditions.

Within this chapter, models are presented, describing the diffusion and nucleation processes. These models allow for a detailed understanding of diffusion, nucleation and growth. Suitable experiments are presented, which allow for determining the model's parameters. First, the motion of a single molecule on a surface is analyzed (Sec. 4.1). From the movement of single molecules, the nucleation and growth processes is conveyed and quantified by the analysis of island densities (Sec. 4.2 and Sec. 4.3) and island sizes (Sec. 4.4).

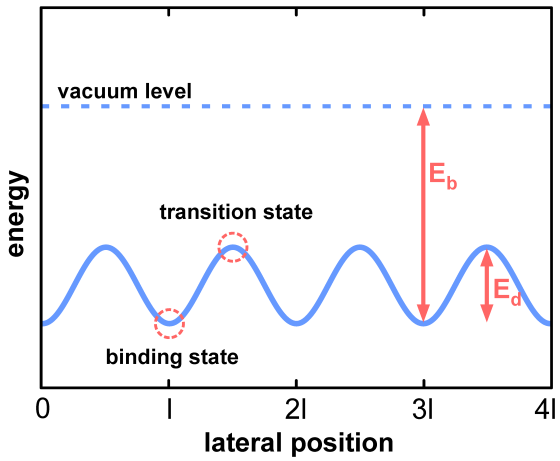

Figure 4.3: Energy landscape of a one-dimensional surface. Once a molecule sticks to the surface, it is bound with E_b. The molecules can move between distinct binding sites separated by a distance l, if they overcome a transition state through, e.g., thermal activation. The energy difference between the binding state and the transition state is the diffusion barrier E_d.

4.1 Diffusion of single molecules

An adsorbed molecule is bound to the surface with an energy E_b (see Fig. 4.3). It is able to move on the substrate in a random walk by jumping between adjacent adsorption sites. An adsorption site is a localized minimum in the surface energy landscape probed by a molecule (i.e. *binding state*). For a single jump between two adsorption sites separated by a distance l, the molecule has to overcome an energy barrier, which is the *diffusion barrier* E_d. Considering a thermally activated jump process, jumps become more/less frequent with increasing/decreasing substrate temperature T_S. In detail, the jump frequency of the molecule (*hopping rate*) ν is expected to follow a universal Arrhenius law[31–33]

$$\nu = \nu_0 e^{-\frac{E_d}{k_B T_S}} \tag{4.1}$$

with Boltzmann constant k_B. Thus, the hopping rate is governed by the ratio of diffusion barrier to temperature. The pre-exponential factor ν_0 is referred to as *attempt frequency* and contains all dynamic information. The attempt frequency can be depicted as the oscillation frequency of a molecule at its adsorption site trying to overcome the transition state. For large molecules the attempt frequency lies in the range from $10^{10}\,\mathrm{s}^{-1}$ to $10^{14}\,\mathrm{s}^{-1}$.[34–36]

A prerequisite for the applicability of the random walk picture is that the molecules have sufficient time between two jumps to equilibrate, i.e. the molecule 'forgets' where it came from and the subsequent jump is random. This requirement is fulfilled, if single jumps are rare events compared to the attempt frequency ($\nu \ll \nu_0$).[28]

After having considered the timescale of jumps in Eqn. 4.1, now, the spatial motion in the random walk of a single molecule is analyzed. Based

Units

$[\nu] = \mathrm{s}^{-1}$
$[\nu_0] = \mathrm{s}^{-1}$
$[E_d] = \mathrm{eV}$
$[T_S] = \mathrm{K}$

Constants

$k_B = 8.62 \cdot 10^{-5}\,\mathrm{eV\,K}^{-1}$

on the line of argumentation as presented in Ref. 37, first the random walk in one direction is analyzed to subsequently introduce the two dimensional one.

For the random movement of a single molecule in one dimension the mean displacement $\langle \Delta x(t) \rangle$ is defined by

$$\langle \Delta x(t) \rangle \equiv \langle x(t) - x(0) \rangle = 0 \tag{4.2}$$

The mean displacement is zero, because a molecule jumps with equal probability in both directions. However, the square of these displacements will give a non-zero and positive value, which represents the total squared distance traveled by the molecule (independent of the direction). The mean square displacement reads

$$\left\langle \Delta x(t)^2 \right\rangle \equiv \left\langle [x(t) - x(0)]^2 \right\rangle = l_x^2 M_x(t) \tag{4.3}$$

where l_x is the length of a single jump between two adsorption positions and $M_x(t)$ is the total number of hopping events till time t. The number of jumps $M_x(t)$ increases linear with time

Units

$[M_{x/y}]$	=	1
$[l_{x/y}]$	=	m
$[v_{x/y}]$	=	s^{-1}
$[t]$	=	s
$[l]$	=	m
$[D]$	=	$m^2\,s^{-1}$

$$M_x(t) = v_x t \tag{4.4}$$

The introduced constant of proportionality v_x represents the hopping rate in one dimension. Using the identity from Eqn. 4.4, Eqn. 4.3 turns into

$$\left\langle \Delta x(t)^2 \right\rangle = l_x^2 v_x t \tag{4.5}$$

Thus, the mean square displacement increases linear with time. This is obvious from the fact that the probability of finding a molecule more far away from the zero-point $x(0)$ increases with the number of jumps, which is direct proportional to time.

In analogy, for the case of isotropic diffusion in two dimensions the mean square displacement $\mathbf{r}(t) = (x(t), y(t))$ reads

$$\begin{aligned} \left\langle |\Delta \mathbf{r}(t)|^2 \right\rangle \equiv \left\langle |\mathbf{r}(t) - \mathbf{r}(0)|^2 \right\rangle &= l_x^2 v_x t + l_y^2 v_y t \\ &= l^2 v t \end{aligned} \tag{4.6}$$

With the square jump length $l^2 = l_x^2 + l_y^2$ and the hopping rate $v = v_x = v_y$ which identity is found in Eqn. 4.1. Now, the *tracer diffusion coefficient D* is defined

$$\left\langle |\Delta \mathbf{r}(t)|^2 \right\rangle = 4 \underbrace{\frac{1}{4} l^2 v}_{D} t \tag{4.7}$$

The tracer diffusion coefficient D becomes the surface area visited by the molecule per unit time and therefore reflects the mobility of a molecule

on the surface.[38] Besides the tracer diffusion coefficient D also a *collective diffusion coefficient* D_c exists. Both are numerically and conceptually distinct quantities. The tracer diffusion specifies the random walk of single, isolated molecules. In contrast, the collective diffusion describes an ensemble of mutually interacting molecules. However, for low coverages, D coincidents with D_c. The extracted factor of $\frac{1}{4}$ in Eqn. 4.7 is attributed to this fact.[28] Within the present thesis the focus is on the tracer diffusion solely.

The tracer diffusion coefficient D is a central quantity in surface diffusion.[37]

$$\boxed{D = \frac{1}{4} l^2 \nu} \tag{4.8}$$

Using Eqn. 4.1, the tracer diffusion coefficient reads

$$D = \frac{1}{4} l^2 \nu_0 e^{-\frac{E_d}{k_B T_S}} \tag{4.9}$$

In an experiment, the diffusion barrier and the attempt frequency can be determined by counting hopping events ν at various substrate temperatures T_S.[39] From Eqn. 4.1 it is apparent that by plotting the hopping rate $\ln(\nu)$ versus the inverse temperature T_S^{-1} a linear dependence results. Thus, from the slope of a linear fit of related experimental data the diffusion barrier is extracted (see Fig. 4.4)

$$E_d = k_B \frac{\partial(\ln \nu)}{\partial T_S^{-1}} \tag{4.10}$$

The axis intercept $\lim_{T_S^{-1} \to 0} \nu$ determines the attempt frequency

$$\nu_0 = \lim_{T_S^{-1} \to 0} \nu \tag{4.11}$$

Hence, for very high temperatures fulfilling $T_S^{-1} \to 0$, the hopping rate becomes equal to the attempt frequency, i.e. each attempt of a molecule to jump is successful.

Exploiting the hopping model through Eqn. 4.10 and Eqn. 4.11 is a widely used approach to quantify adsorbate diffusion.[39] Using this method, diffusion has been studied extensively for atomic species on metallic surfaces and results have been reviewed in Ref. 29,37–41. The model does not immediately apply to the diffusion of molecules. Molecules have inner degrees of freedom and can reveal a high asymmetry in structure as well as in their interaction with the surface. Thus, the diffusion can be highly asymmetric, e.g. resulting the molecular rows.[42] In such cases, the application of the simple hopping model is restricted. For some organic molecules on metal surfaces, however, the diffusion parameters were nevertheless

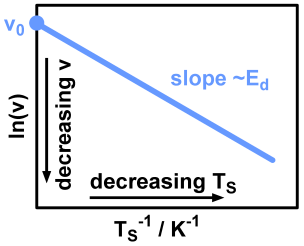

Figure 4.4: Exemplary sketch of the hopping rate $\ln \nu$ versus the inverse substrate temperature T_S^{-1}. The slope defines the diffusion barrier E_d and the axis intercept at $T_S^{-1} \to 0$ defines the attempt frequency ν_0.

determined by direct observation of hopping events.[34–36,39,40] These studies have revealed diffusion barriers for organic molecules on metallic substrates often being considerably larger than 800 meV, a barrier height that allows for monitoring single adsorbate jumps at room temperature.[34,36,39] For instance, a value of 1400 meV has been found for diffusion of C_{60} on Pd(110).[35]

In general, the diffusion barrier of organic molecules on insulating surfaces is much smaller than on metallic surfaces,[39,43,44] as evidenced by a strong clustering of organic molecules on insulating surfaces.[45–47] Due to the small diffusion barrier, monitoring of individual adsorbate jumps is, therefore, not feasible at room temperature. Moreover, in the case of small diffusion barriers, a direct observation of single hopping events may be influenced by the interaction between the imaging tip and molecule, as observed in STM[48–50] and NC-AFM imaging.[51–54]

To overcome these drawbacks for weak molecule-substrate interactions, an alternative method has been established to determine the parameters of diffusion from experiment. These method will be presented and discussed in the following sections.

4.2 Island densities

As described in the previous section, single molecules can diffuse on surfaces through thermal activation. Hence, there is a probability that two diffusing molecules meet at adjacent lattice sites, forming a nucleus stabilized by intermolecular interactions. Once a nucleus has formed, it can grow further by capture of diffusing molecules, thus forming an island. However, a nucleus or island can also decay by detachment of molecules. Within this section, these dynamic processes of nucleation and growth will be described and addressed in a quantitative manner. This section is based on Ref. 28 and Ref. 29. The constructed model will be applied to a molecule-insulator system in Sec. 8.1.

For the following simplified formalism the case of *complete condensation* (no desorption from the surface, i.e. the desorption rate $R = 0$ vanishes) is assumed. This yields that the total coverage θ increases with the deposition rate F and is directly proportional to the time t

$$\theta = \Omega F t \tag{4.12}$$

Ω is the area of an adsorption site on the surface. Moreover, single molecules are assumed to be the only mobile species (the mobility of larger clusters is neglectable small), i.e. dimers and larger clusters are not mobile on the surface but can grow/decay by capture / detachment of single molecules.

In a first step, the net rates Γ_s at which clusters of size $s+1$ emerge from clusters of size s by capture of a single molecule are under consideration. The net rates can be written as

$$\Gamma_s = \sigma_s D n_1 n_s - \gamma_{s+1} n_{s+1} \tag{4.13}$$

The first term constitutes the forming of clusters with size $s + 1$ from clusters with size s. It is proportional to the density n_1 of single molecules and the density n_s of clusters with size s. The dimensionless *capture number* σ_s expresses the affinity of a cluster with size s to absorb a single molecule. The diffusion coefficient D accounts to the mobility of single molecules on the surface and was subject in the previous section (see Eqn. 4.9)

The second term models the decay of clusters with size $s + 1$ to cluster with size s and is, therefore, lowering the net rate Γ_s. It is proportional to the density n_{s+1} of clusters with size $s + 1$. γ_{s+1} is the rate, at which molecules detach from clusters with size $s + 1$.

From the net rates Γ_s the time evolution of the density of single molecules n_1 can be written as

$$\frac{\mathrm{d}n_1}{\mathrm{d}t} = F - 2\Gamma_1 - \sum_{s=2}^{\infty} \Gamma_s \tag{4.14}$$

Units

$[\theta]$	=	1
$[\Omega]$	=	m^2
$[F]$	=	$\mathrm{m}^{-2}\,\mathrm{s}^{-1}$
$[R]$	=	$\mathrm{m}^{-2}\,\mathrm{s}^{-1}$
$[t]$	=	s
$[\Gamma_s]$	=	$\mathrm{m}^{-2}\,\mathrm{s}^{-1}$
$[\sigma_s]$	=	1
$[D]$	=	$\mathrm{m}^2\,\mathrm{s}^{-1}$
$[n_s]$	=	m^{-2}
$[\gamma_s]$	=	s^{-1}

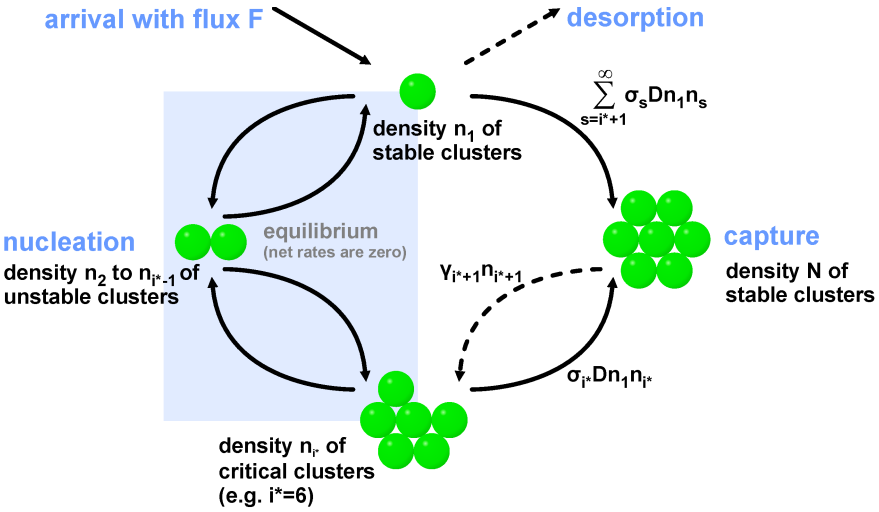

Figure 4.5: Competitive processes during nucleation on a surface. The arrows mark the exchange of a single molecule. Desorption of molecules from the surface is excluded in the model provided in the main text. The density of stable clusters does not decay within time, but grows by capture of further single molecules from critical clusters.

The density n_1 of single molecules grows with the arrival of molecules on the surface (deposition rate F). It decays by the formation of dimers from two single molecules (this accounts to two times Γ_1) and the capture of single molecules by larger clusters with sizes $s \geq 2$.

For all larger clusters $s \geq 2$ the time evolution of cluster densities is given by

$$\frac{dn_s}{dt} = \Gamma_{s-1} - \Gamma_s \qquad (s \geq 2) \tag{4.15}$$

The density n_s of clusters of size s grows with the net rate Γ_{s-1} and decays with the net rate Γ_s.

Basically, Eqn. 4.13, Eqn. 4.14 and Eqn. 4.15 fully describe the nucleation process. However, the equations contain too many unknown variables. Hence, further simplifications are necessary. By introducing the *critical cluster size* i^*, the clusters are classified in *stable* and *unstable* ones. All cluster larger than the critical size $s > i^*$ are defined as stable. Molecules, once captured, cannot detach from stable clusters. Thus, the detachment rate of molecules vanishes for stable clusters, i.e. $\gamma_s = 0$ for $s \geq i^* + 1$. Stable clusters can only grow, but not shrink in size.

For smaller clusters, i.e. unstable clusters $s \leq i^*$, the detachment of single molecules is assumed to occur sufficiently rapidly to establish a equilibrium between the different cluster sizes with $s \leq i^*$. Thus, Γ_s vanishes for $1 \leq s \leq i^* - 1$. An overview of the competitive processes, can be seen in Fig. 4.5.

Note, that the critical cluster size i^* depends on deposition parameters (such as flux F and substrate temperature T_S during deposition) and is not an intrinsic constant for the molecule-substrate system.

The *total density* N of stable clusters is given by

$$N = \sum_{s=i^*+1}^{\infty} n_s \tag{4.16}$$

Using $\gamma_s = 0$ for $s \geq i^* + 1$, the time evolution of N simplifies (see App. A) to

$$\frac{\mathrm{d}N}{\mathrm{d}t} = \sigma_{i^*} D n_1 n_{i^*} \tag{4.17}$$

The term $\sigma_{i^*} D n_1$ corresponds to the average flux of single molecules to a cluster of size i^*. Moreover, the evolution in the total density of stable clusters depends on the density n_{i^*} of cluster at the critical size.

After having conveyed the evolution of cluster of size $s \geq i^* + 1$, the evolution of the density of single molecules n_1 is further simplified. Introducing the *average capture number* $\bar{\sigma}$

$$\bar{\sigma} = \frac{1}{N} \sum_{s=i^*+1}^{\infty} n_s \sigma_s \tag{4.18}$$

the evolution of n_1 reads (see App. B)

$$\frac{\mathrm{d}n_1}{\mathrm{d}t} = F - \sigma_{i^*} D n_1 n_{i^*} - \bar{\sigma} D n_1 N \tag{4.19}$$

The term $\bar{\sigma} D n_1$ relates to the average flux of single molecules to stable clusters. Hence, the density n_1 of single molecules decreases with the rate of single molecules captured by critical clusters (thus forming a stable clusters) and the rate of single molecules captured by stable clusters. The density n_1 of single molecules increases with the deposition rate.

Finally, the regime with cluster sizes $2 \leq s \leq i^*$ has to be analyzed. As noted before, the net formation rates Γ_s vanish for these cluster sizes. This equilibrium is inducing the detailed balance relation (*Walton relation*) between the unstable clusters[55]

$$\Omega n_s \approx (\Omega n_1)^s \, \mathrm{e}^{\beta E_s} \tag{4.20}$$

The term Ωn_s can be interpreted as the probability that an adsorption site Ω is occupied by a cluster of size s. This probability is approximately equal the probability $(\Omega n_1)^s$ of finding s independent single molecules at adjacent sites (forming a cluster of size s) times a statistical term, depending on the percentage of the cluster binding energy E_s to the temperature $\beta = 1 / k_B T_S$. The cluster binding energy is the energy which is gained by forming/dispersing a cluster of size s, i.e. $E_1 = 0$.

Putting these simplifications together, the processes condense from that sketched in Fig. 4.5 to the ones in Fig. 4.6.

Units

$[N] = \mathrm{m}^{-2}$

$[\bar{\sigma}] = 1$

$[T_S] = \mathrm{K}$

$[\beta] = \mathrm{eV}$

$[E_s] = \mathrm{eV}$

Constants

$k_B = 8.62 \cdot 10^{-5}\,\mathrm{eV\,K^{-1}}$

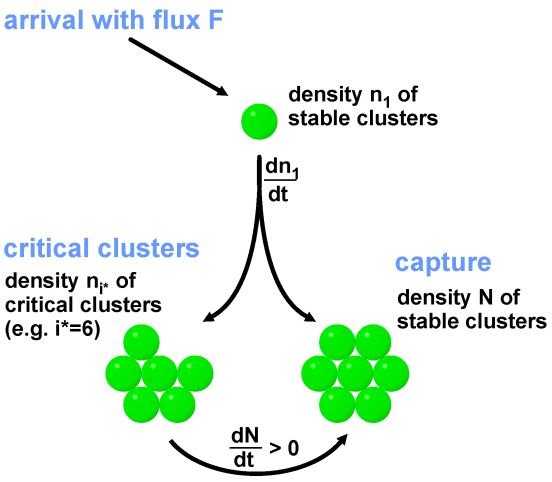

Figure 4.6: Simplified model of the competitive processes during nucleation on a surface. The arrows mark the exchange of a single molecule.

Combining Eqn. 4.17, Eqn. 4.20 and Eqn. 4.19 brings forth the differential equation

$$\frac{dN}{dt} = \frac{\sigma_{i^*}}{\bar{\sigma}^{i^*+1}} \Omega^{i^*-1} \left(\frac{F}{D}\right)^{i^*} F e^{\beta E_{i^*}} N^{-(i^*+1)} \tag{4.21}$$

This differential equation is solved (see App. C) by

$$\hat{N} \equiv \Omega N = \underbrace{\left[(i^*+2)\frac{\sigma_{i^*}}{\bar{\sigma}^{i^*+1}}\theta\right]^{\frac{1}{i^*+2}}}_{\eta(\theta,i^*)} \left(\Omega^2 \frac{F}{D}\right)^{\frac{i^*}{i^*+2}} e^{\beta \frac{E_{i^*}}{i^*+2}} \tag{4.22}$$

which constitutes the central result of nucleation theory.[56–58] An important scaling relation is evident in Eqn. 4.22, i.e. the island density per adsorption site $\hat{N}$ scales with the flux F and the ability of the molecules to diffuse on the surface D through a *scaling exponent* $\frac{i^*}{i^*+2}$

$$\hat{N} \sim \left(\frac{F}{D}\right)^{\frac{i^*}{i^*+2}} \tag{4.23}$$

Using Eqn. 4.9, the result from Eqn. 4.22 can be rewritten to

$$\hat{N} = \eta(\theta, i^*) \left(4\frac{\Omega^2 F}{l^2 \nu_0}\right)^{\frac{i^*}{i^*+2}} e^{\beta \frac{E_{i^*}+i^* E_d}{i^*+2}} \tag{4.24}$$

Theoretical considerations in Ref. 57 reveal that the prefactor η varies slowly upon changing the coverage θ and the critical island size i^*. The prefactor can be approximated to $\eta \approx 0.25$ for low coverages ($\theta \approx 0.1$) and small critical island sizes ($1 \leq i^* \leq 5$).

4.3 Experiments on island densities

From Eqn. 4.24 it is evident that the island density for a molecule-substrate system can be tuned in experiment through two parameters, namely the flux F and the substrate temperature T_S. Thus, analyzing the island densities in experiment at various fluxes and temperatures yields the scaling exponent, the attempt frequency ν_0 and the diffusion barrier E_d.

Temperature-dependent island densities

Eqn. 4.24 allows to reveal the diffusion barrier E_d and the attempt frequency ν_0 from a temperature-dependent analysis of island densities. In the first place, this kind of experiment was performed by Bott et al. in Ref. 49. A short outline of this experiment is given in the following. A small amount of molecules is deposited onto the surface, using a fixed flux F and coverage θ. During deposition, the substrate temperature T_S is held at a fixed value (typically between room temperature and liquid nitrogen or liquid helium temperature). After deposition, the sample is quenched to a temperature, at which diffusion is entirely frozen, and imaged by scanning probe microscopy. This experiment is carried out for different substrate temperatures T_S. For each experiment, the island density per adsorption site of the deposited species $\hat{N}$ is counted and plotted against the substrate temperature T_S at deposition (see Fig. 4.7). From Eqn. 4.24 it is apparent that the slope $\ln \hat{N}$ versus T_S^{-1} determines the diffusion barrier to

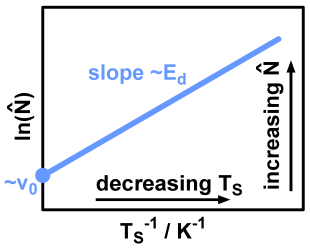

Figure 4.7: Exemplary sketch of the island density $\ln \hat{N}$ versus the substrate temperature T_S^{-1}. The slope defines the diffusion barrier E_d and the axis intercept at $T_S^{-1} \rightarrow 0$ defines the attempt frequency ν_0.

$$E_d = k_B \frac{i^* + 2}{i^*} \frac{\partial \hat{N}}{\partial T_S^{-1}} - \frac{E_{i^*}}{i^*} \tag{4.25}$$

and the axis intercept $\hat{N}_0 = \lim_{T_S^{-1} \rightarrow 0} \hat{N}$ gives the attempt frequency

$$\nu_0 = 4F \frac{\Omega^2}{l^2} \left(\frac{\eta}{\hat{N}_0} \right)^{\frac{i^*+2}{i^*}} \tag{4.26}$$

Using this approach, the diffusion barrier has been determined for a few molecular systems on metallic and semi-conducting surfaces.[59,60] On insulating surfaces, however, quantitative analysis of molecular diffusion has been performed very rarely so far.[61–63]

Flux dependent island densities

Using Eqn. 4.24, the scaling exponent and therefore the critical island size i^* can be revealed from flux dependent analysis of island densities. In contrast to the previously described method, the temperature T_S is the same for

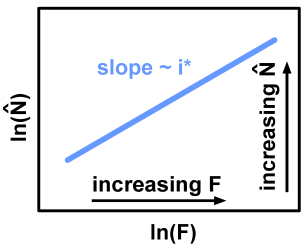

Figure 4.8: Exemplary sketch of the linear dependence of the island density $\ln \hat{N}$ on the flux $\ln F$. The slope defines the critical island size i^*.

all flux experiments. Instead, the flux F is varied using a fixed coverage θ. For each experiment, the resulting island density per adsorption site $\hat{N}$ is counted and plotted against the flux F (see Fig. 4.8). From Eqn. 4.24 it is apparent that the slope $\ln \hat{N}$ versus $\ln F$ determines the scaling exponent to

$$\frac{i^*}{i^* + 2} = \frac{\partial \ln \hat{N}}{\partial \ln F} \tag{4.27}$$

Using this method, the scaling exponent has been determined for some molecular systems on various surfaces.[64–67]

Tuning the flux is rather demanding, because the coverage on the surface must be the same for each different flux. Hence, for each flux the deposition time must be validated to ensure a constant coverage. However, another method is open to determine the critical island size. This method is based on the analysis of island size distributions, as described in the following section.

4.4 Island size distribution

Considering the steady state nucleation regime with an island size distribution n_a (n_a denotes the density of islands with size a), the dynamic scaling hypothesis[68–71] states that n_a scales with the following three parameters: the coverage θ, the mean island size A and a scaling function $f_{i^*}(a / A)$

$$n_a = \theta A^{-2} f_{i^*}(a / A) \tag{4.28}$$

The scaling function depends solely on the critical island size and the ratio of a / A, but not on the coverage. An empirical function on the basis of kinetic Monte Carlo simulations has been constructed[72]

$$f_{i^*}(a / A) = c_{i^*}(a / A)^{i^*} \exp\left(-i^* b_{i^*}(a / A)^{1/b_{i^*}}\right) \tag{4.29}$$

where c_{i^*} and b_{i^*} are fixed through the normalization conditions

$$\int_0^\infty f_{i^*}(a / A)\mathrm{d}(a / A) = \int_0^\infty (a / A) f_{i^*}(a / A)\mathrm{d}(a / A) = 1 \tag{4.30}$$

To obtain the critical island size from experiment, the island size distribution n_a is analyzed for different coverages θ at a fixed temperature T_S and compared to the theoretical island size distributions given by $f_{i^*}(a / A)$ for different i^* given by Eq. 4.29. This is exemplary sketched in Fig. 4.9. The experimental data is plotted together with the theoretical functions $f_{i^*}(a/A)$ for $i^* = 1, 2, 3$. To determine i^*, the particular scaling function is make out, which best fits the experimental data. In this case $i^* = 2$ may be assigned.

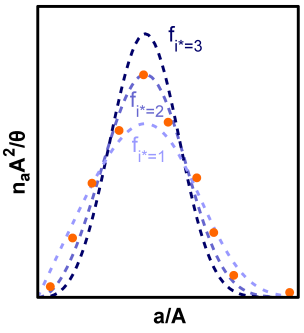

Figure 4.9: Exemplary sketch of an experimental island size distribution compared to theoretical functions $f_{i^*}(a / A)$ for $i^* = 1, 2, 3$. The experimental data is best fitting $i^* = 2$ in this case.

5 Surfaces

Contents

The assembly of molecule species, which will be presented in Sec. 6, was explored on two different substrate surfaces within this thesis. These surfaces are the TiO_2 (110) and the CaF_2 (111) surface. They were chosen because they present significantly different surface properties, having rather different influence on the molecular self-assembly.

TiO_2 is a covalently bonded crystal and exhibits a reactive (110) surface. The TiO_2 (110) surface shows a rectangular lattice and is corrugated, consisting of troughs running along the surface. Molecules are expected to show anisotropic assembly in the troughs. On the surface, a high density of steps and atomic defects is evident, which may act as nucleation sites and therefore influence the molecular assembly.

In contrast, CaF_2 is an ionic crystal and exhibits an inert (111) surface. The CaF_2 (111) surface shows a hexagonal lattice and is atomically flat with large terraces. Therefore, the assembly of molecules on this surface is not expected to be templated as strongly as on the corrugated TiO_2 (110) surface. Moreover, the CaF_2 (111) surface is free of defects and exhibits only a low density of step edges. Thus, molecular diffusion is less hindered than on the TiO_2 (110) surface.

Thus, both surfaces show rather different characteristics on the surface corrugation, the reactivity and the defect density. These mentioned surface characteristics are decisive for molecular self-assembly. Experiments on the molecular arrangement on these surfaces will be presented in Sec. 7-10.

In this section, both surfaces will shortly be introduced. The surface preparation and properties as well as specific NC-AFM imaging characteristics will be presented.

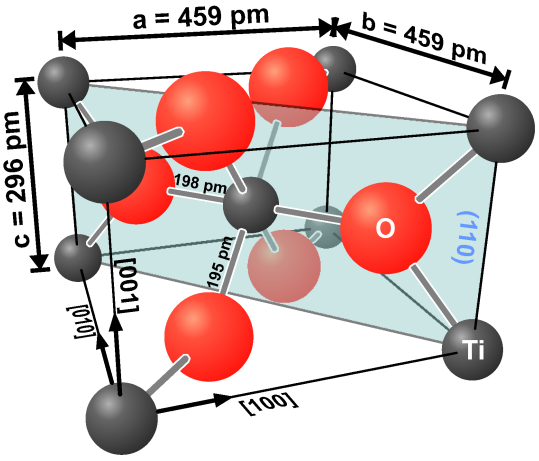

Figure 5.1: Ballstick model of the tetragonal crystal system of rutile TiO_2 with the lattice parameters $a = b = 459$ pm and $c = 296$ pm and two different Ti-O bond length (198 pm und 195 pm). The (110) plane is sketched.

5.1 Rutile TiO_2 (110) surface

Titanium dioxide is one of the most intensively studied oxides, representing a prototypical system for transition metal oxides. It presents a wide range of catalytic applications, photocatalytic as well as electrocatalytic.[73,74] Titanium dioxide can crystallize in three different modifications, which are *rutile*, *anatas* and *brookit*. Both the rutile and the anatas form belong to the class of tetragonal crystals, whereas brookit is an orthorhombic crystal. Rutile is structurally assigned to the space group $P4_2/mnm$ of the ditetragonal-dipyramid crystal class (D_{4h}) with the lattice parameters $a = b = 459$ pm and $c = 296$ pm.[75,76] The titanium atoms are surrounded in an octahedral form by six oxygen atoms. The octahedron is distorted, resulting in two different Ti-O bonding length (198 pm and 195 pm).[75] Every oxygen atom is planar threefold coordinated and part of three octahedrons (Fig. 5.1).

Preparation and surface properties

Rutile TiO_2 samples used in this work are crystals of highest available quality (MTI, Richmond, USA). The surface is very reactive and thus needs to be thoroughly cleaned after insertion into the UHV system. Surface contaminations are removed by repeated cycles of sputtering with argon cations at a kinetic energy of 1 keV and subsequent annealing at 1100 K for fifteen minutes.

The TiO_2 (110) surface is characterized by protruding bridging-oxygen rows running in [001] direction with a periodicity of 649 pm in $[\bar{1}10]$ direction and the parallel titanium rows, which are centered between the bridging-oxygen rows (Fig. 5.2).

Directly after preparation, surface defects appear as vacancies in the bridging-oxygen rows.[77] Water molecules of the residual gas can adsorb on the surface and dissociate on oxygen vacancies, forming hydroxyls.[78,79]

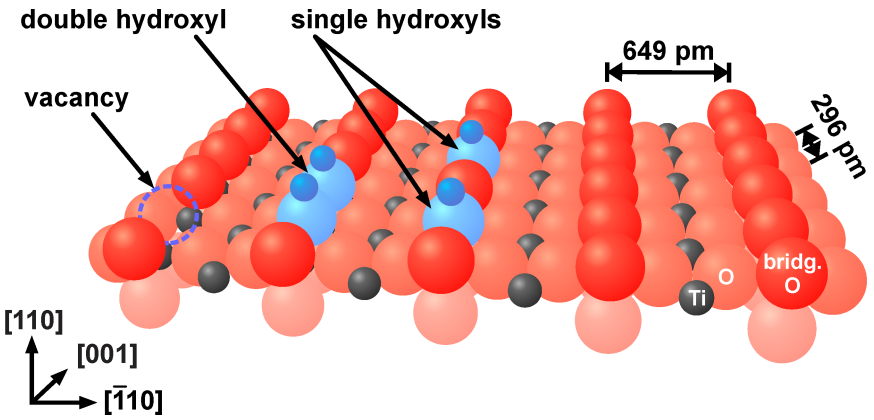

Figure 5.2: On the TiO_2 (110) surface vacancies as well as double and single hydroxyl defects exist on the bridging-oxygen rows.

Vacancies, single hydroxyls and double hydroxyls can be seen on the surface as defects (Fig. 5.2). The hydroxyls are stable at room temperature. At temperatures above 520K, hydroxyls recombine again and desorb as water molecules.[80]

Contrast formation in NC-AFM imaging

As mentioned before, NC-AFM measurements do not necessarily reveal the real surface topographic structure of the investigated substrate. The contrast formation of NC-AFM is strongly affected by the tip morphology and termination. For TiO_2 (110), different contrasts have been reported.[81–84] The four most common, which have occured during this study, will be presented shortly in the following (Fig. 5.3).

An anion at the tip apex results in a higher negative frequency shift over the positively charged titanium rows in comparison with the more negatively charged bridging-oxygen rows. The positively charged defects on the bridging oxygen rows appear as bright features in-between the bright titanium rows (Fig. 5.3(a)).[81] From the size of the imaged defects, it can be determined whether this defect is an oxygen vacancy, a single hydroxyl or a double hydroxyl.[77] With a cation at the tip apex the contrast is inverted. The bridging-oxygen rows are imaged bright with the defects appearing as dark spots in the bright rows (Fig. 5.3(b)). Both contrasts were observed experimentally and confirmed by calculations.[81] The third contrast mode cannot be explained with pure electrostatic interactions. In this contrast mode the bridging-oxygen rows are imaged bright and the hydroxyls are emerging as brighter spots on these rows (Fig. 5.3(c)).[82] Vacancies are imaged dark. Recently, a fourth contrast was observed, which resembles the contrast formation of the previous mode, but additionally uncovers the titanium rows in between the bridging-oxygen rows as faint bright rows (Fig. 5.3(d)).[26,83]

Thus, the appearance of the defects can be used for chemical identifica-

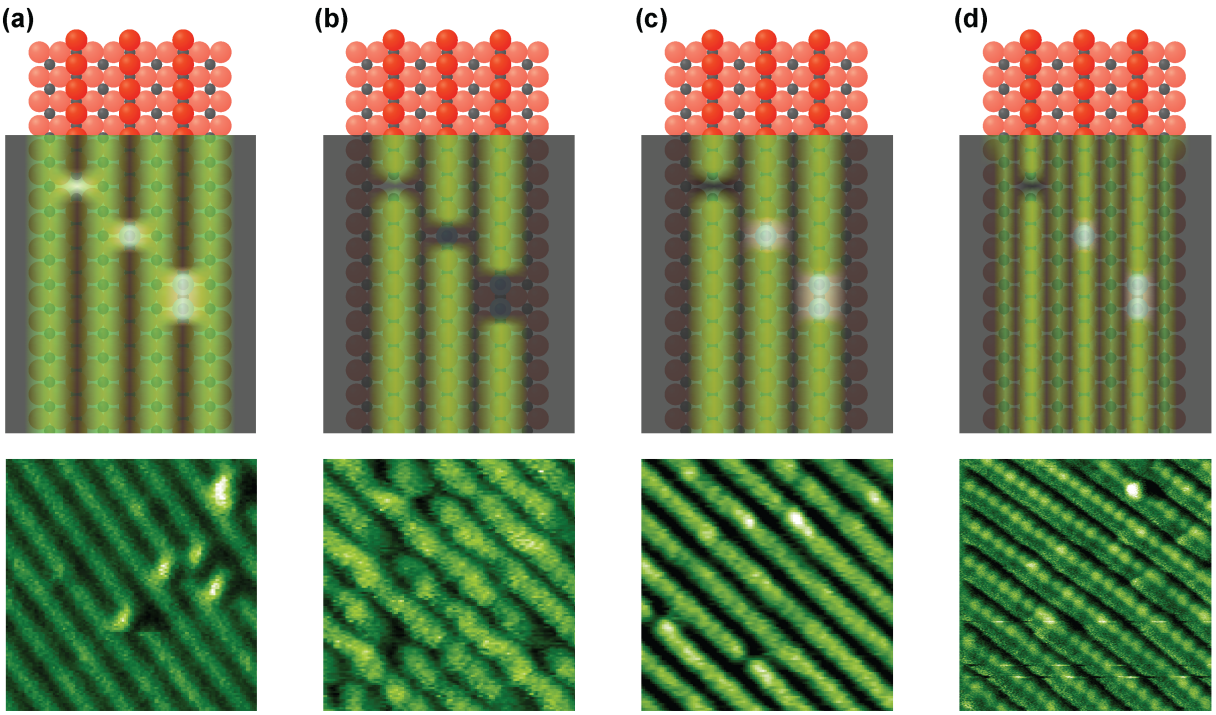

tion and for clarification whether the titanium or the bridging-oxygen rows are imaged bright. However, the tip termination can change during scanning when the tip picks something up from the surface. Also molecules of the residual gas can stick to the tip apex and change the contrast.

Figure 5.3: Schematic drawings (upper panel) and NC-AFM images[85] (lower panel) of the four different contrasts in the *df*-channel corresponding to different tip terminations.

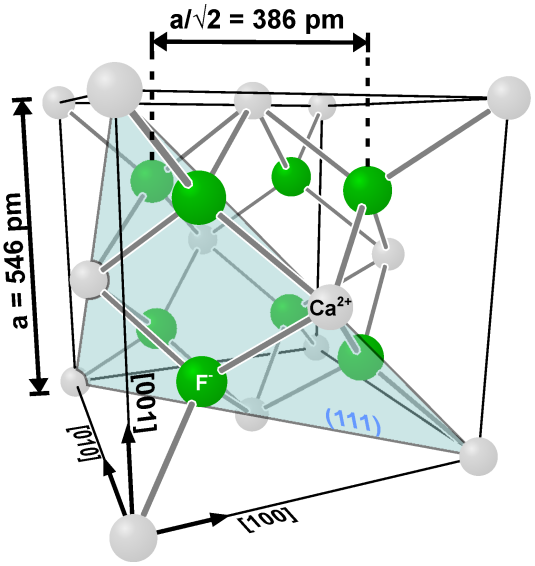

Figure 5.4: Ballstick model of the cubic crystal system of CaF_2 with the lattice parameter a = 546 pm. The (111) plane is sketched.

5.2 CaF_2 (111) surface

Large, monocrystalline calcium fluoride crystals can synthetically be grown with highest purity.[86] Calcium fluoride a widely used material for lenses, e.g. in lithography.[87] CaF_2 is structurally assigned to the space group $Fm\bar{3}m$ of the cubic crystal class (O_h) with the lattice parameter a = 546 pm.[88] The calcium cations are surrounded in a cubic form by eight fluorine anions. Every fluorine anion is tetrahedrally coordinated (Fig. 5.4).

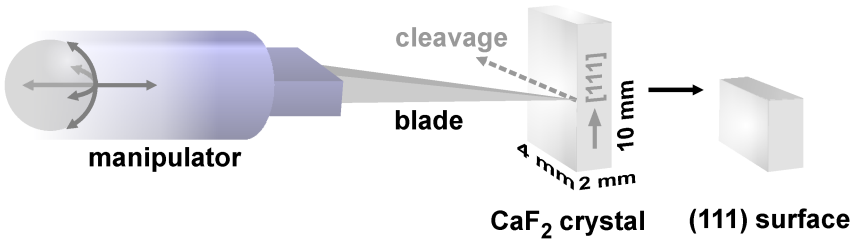

Figure 5.5: Preparation of the (111) surface of a CaF_2 crystal with typical dimensions of 2 mm x 4 mm x 10mm. A sharp blade is scribed parallel to the (111) surface until the upper part breaks apart. This method reveals large atomically flat terraces.

Preparation and surface properties

The (111) surface of a CaF_2 crystal (Korth Kristalle, Altenholz, Germany) is prepared by cleavage. For that purpose a sharp blade is used to scribe the crystal parallel to the (111) surface until the upper part breaks apart (Fig. 5.5).[89] Cleavage under ambient conditions would lead to a rapid degradation of the surface.[90] Thus, cleavage is performed under UHV conditions, revealing large atomically flat terraces often larger than 4 μm^2. To remove trapped charges from the surface, the sample is heated for 1.5 h at 425 K before measurements.[91]

Along the [111] direction the crystal consists of layers of fluorine and calcium (Fig. 5.6). Although the layers are charged, there is no net dipole moment perpendicular to the surface. The layers are stacked in the order $(F^-–Ca^{2+}–F^-)–(F^-–Ca^{2+}–F^-)–(...)$. A sequence $F^-–Ca^{2+}–F^-$ of layers is called a *triple layer* and has a height of $a/\sqrt{3}$ = 315 pm. At cleavage, a separation at adjacent triple layers (i.e. adjacent fluorine layer) is energetically favorable, therefore, the CaF_2 (111) surface is always fluorine terminated and step heights are multiples of the triple layer height.[91,92]

The CaF_2 (111) surface itself is characterized by a threefold symmetry and a periodicity of $a/\sqrt{2}$ = 386 pm. Both, fluorine and calcium ions are arranged in a hexagonal manner on the (111) surface. In contrary to the bulk CaF_2 crystal, the fluorine and calcium ions of the first layer are less coordinated (three- and sevenfold, respectively).

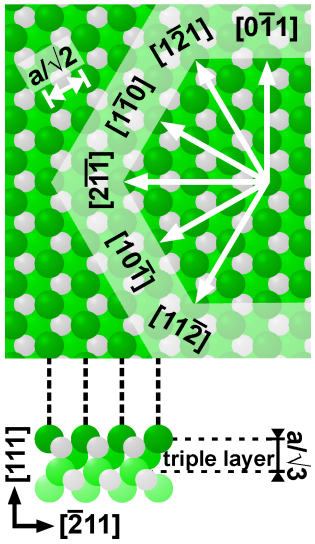

Figure 5.6: Sketch of the CaF_2 (111) surface. The periodicity $a/\sqrt{2}$ = 386 pm and directions on the surface are given. A side view of the model parallel to the [0$\bar{1}$1] direction shows the stacking sequence of triple layers.

Contrast formation in NC-AFM imaging

As observed for the TiO_2 (110) surface, different tip terminations can alter the tip-sample interaction and therefore the appearance of the surface in NC-AFM imaging. Actually, two different contrasts are known on the CaF_2 (111) surface, ascribed to electrostatic interactions between the surface and different ionic tip terminations. Both contrasts have been observed experimentally and have been confirmed by calculations.[93–95]

An anion at the tip apex results in a stronger attractive interaction between the tip and the Ca^{2+} ions. Thus, a higher negative frequency shift is measured on the Ca^{2+} ions than on the F^- ions. This results in a brighter appearance of the Ca^{2+} sublattice compared to the F^- sublattices. The Ca^{2+} ions reveal a disc-like shape.

With a cation at the tip apex, the contrast is inverted. This means, the F^- ions of the corresponding two sublattices in the first triple layer are imaged bright, resulting in a triangular contrast pattern (Fig. 5.7). Hence, by determining the contrast, the orientation and directions of the surface relative to the imaging tip can be assigned unambiguously.

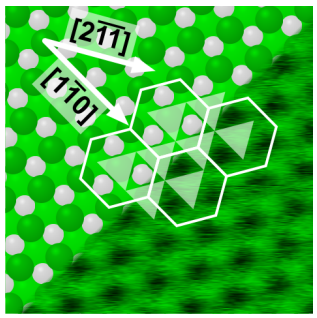

Figure 5.7: Composition of a model of the CaF_2 (111) surface and an NC-AFM image (frequency shift channel) to point out the contrast with a cation at the tip apex. The fluorine sublattices appear as a regular arrangement of triangular features.

6 Molecules

Contents

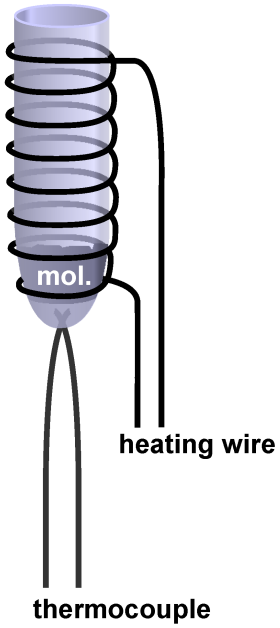

Figure 6.1: Knudsen cell with wound wire for resistive heating and enclosed thermocouple for temperature measurement.

Three different molecule species (C_{60} , SubPc and PTCDI) were probed on surfaces in the context of this thesis. Molecules were deposited on the surfaces by sublimation from home-built Knudsen cells (Fig. 6.1). A Knudsen cell consists of a glas crucible with a wound tungsten wire for resistive heating and an embedded thermocouple. Because the thermocouple is not directly at the molecules, the measured temperatures do not necessarily match with the temperature of the molecules, but correlate with it. The deposition rates were estimated with a quartz crystal deposition monitor (Inficon). The sublimation enthalpy E_S can be obtained by monitoring the deposition rate ν_D versus the temperature T_C of the cell. Following the Arrhenius law from Eqn. 4.1, the sublimation enthalpy is determined from the slope m of $\ln \nu_D$ versus T_C^{-1}

$$E_S = k_B m \tag{6.1}$$

as exemplified in Fig. 4.4.

In the following, each molecule species is descibed and motivated shortly. Additional, the sublimation enthalpies are determined from experiment.

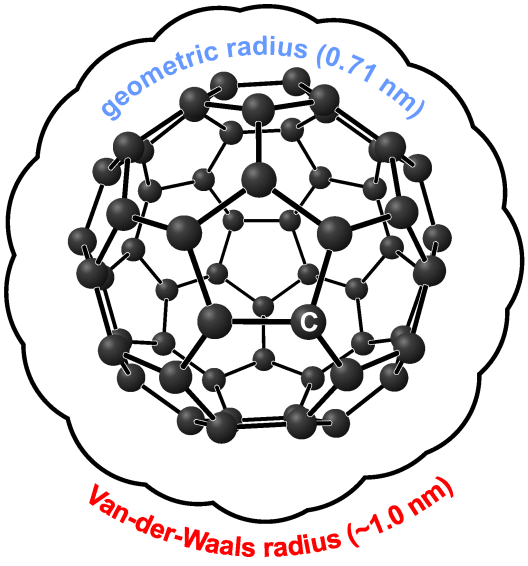

Figure 6.2: The C_{60} molecule consists of sixty carbon atoms in the vertices of a truncated icosahedron. Geometric (0.710 nm) and Van-der-Waals ($\approx$1.0 nm) radii are sketched.

6.1 C_{60}

The C_{60} molecule belongs to the class of fullerenes, which includes all spherical molecules consisting exclusively of carbon. Other carbon modifications are graphite, graphene (single layer of graphite), diamond and carbon nanotubes. The C_{60} molecule consists of sixty carbon atoms, which are located in the vertices of a truncated icosahedron (I_h-Symmetry).[96] In this way, twelve pentagonal and twenty hexagonal subdivisions are spanned, with every pentagon surrounded by five hexagons such that no two pentagonal areas abut (Fig. 6.2).

Crystalline C_{60}

C_{60} molecules adopt different phases according to pressure and temperature. At normal pressure and temperatures below 249 K, the C_{60} molecules arrange in a simple-cubic pattern.[97] Above, C_{60} molecules order in a face-centered cubic way. For even higher temperatures, the vapor phase is adopted. For the purpose of this work the face-centered cubic structure is relevant, as this is the structure of the bulk C_{60} molecules at room temperature. The nearest neighbor distance was estimated to be 1.00 nm with the C_{60} molecules rotating very fast at their lattice position (rotating frequency $>10^9$ s^{-1} at room temperature).[98–100] The mass density of crystalline C_{60} can be calculated and equals 1.68 g/cm^3, being consistent with experiments.[98]

For the sublimation enthalpy, experiments in Fig. 6.3 yield a value of (2.00 ± 0.05) eV following Eqn. 6.1. This value is in good agreement with calculations (2.01 eV[101]) and other experiments (1.74 eV[102]).

Assembly of C_{60} on various surfaces

The intermolecular interaction as well as the interaction of the molecules with the surface are decisive for the equilibrium structure of the molecular arrangement on surfaces. A dominant intermolecular interaction would let the molecules cluster in an island growth mode, arranged incommensurate to the surface lattice. Considering the face-centered cubic bulk structure of C_{60} molecules at room temperature,[103] the molecules would arrange in a lateral close-packed way on the surface like the (111) plane of the bulk C_{60} structure, driven by intermolecular Van-der-Waals interactions between the C_{60} molecules. With a dominant surface-molecule interaction, however, the surface would template the molecules to optimize the substrate-overlayer interaction.

The resulting molecular arrangement is governed by the subtle balance between intermolecular and molecule-surface interactions. On metals, the interaction between C_{60} molecules and the surface has been investigated to be predominantly ionic due to partial charge transfer.[104,105] On some semiconductor surfaces the surface-molecule interaction was determined to be of strong covalent nature.[106,107] Insulator surfaces exhibit Van-der-Waals interactios with the C_{60} molecules, which are in general weaker than ionic or covalent interactions. Recently, C_{60} molecules have been examined with NC-AFM on alkali halides, revealing an unusual morphology.[108] The adsorption of C_{60} on metal oxides has been examined as well. Moreover, the molecular arrangement has been studied on the TiO_2 (110) (1×2)-cross-link surface using STM, revealing an one-dimensional ordering of the C_{60} molecules in the troughs between the added rows of the reconstruction.[109]

A summary of results for C_{60} monolayer systems can be found in Ref. 110, including many further references. However, three different systems (insulating, semiconducting and conducting substrate) will be shortly introduced in the following. On the KBr(100) surface, the interaction with C_{60} molecules is of weak and predominantly Van-der-Waals character. Thus, on this surface, C_{60} molecules tend to form islands at substrate step edges,

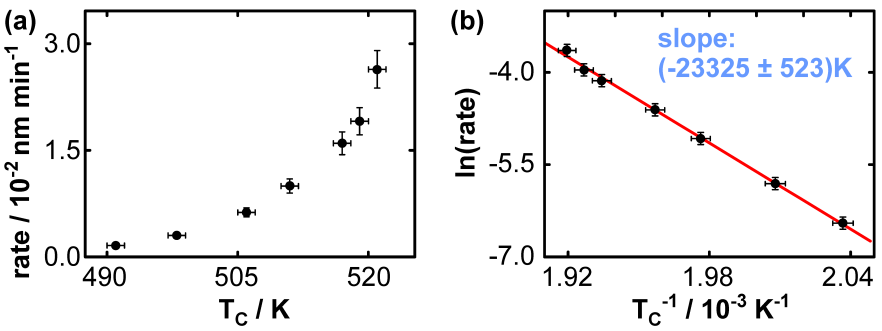

Figure 6.3: Deposition rates of C_{60} at different temperatures with line of best fit.

which have been identified as hexagonally close-packed (8×3) islands.[111] The islands are of an unusual morphology. Compact multilayer islands with incomplete upper layers as well as branched islands with disconnected regions are present.[108] The latter ones consist of a first layer with a second layer rim at the substrate-island edges. Thus, first layer regions are enclosed by a second layer rim. These kind of island originates from a molecular dewetting process of the C_{60} molecules on the surface. On the Cu(111) surface the C_{60} substrate interaction is of intermediate strength and predominantly ionic. The C_{60} molecules diffuse easily on the surface and nucleate at substrate step edges.[105] From the step edges two dimensional islands grow in a close-packed manner towards the upper terrace. Upon annealing at 570 K, a well ordered close-packed overlayer is formed, exhibiting a (4×4) superlattice. The C_{60} molecules do not rotate at their lattice position as in the C_{60} bulk, but are fixed with a hexagonal face facing down towards the surface. Only at defects or kink sites, the C_{60} molecules rotate due to broken symmetry. The interaction of C_{60} with the Si(111) (7×7) surface is of covalent character. The C_{60} molecules interact strongly with the dangling bonds of the surface and are, therefore, immobile at room temperature. Consequently, the step edges play no special role in the binding process.[107,112–114] Also partial charge transfer from the surface to the molecules occurs, which also contributes to the strong interaction with the surface.[115] Single C_{60} domains can be achieved by careful growth on the heated substrate (470 K).[112] Heating of the substrate increases the mobility of molecules on the surface. Thus, C_{60} molecules can nucleate to form islands.

These examples show that C_{60} molecules interact very differently with different substrates. Within this thesis, the adsorption of C_{60} molecules on insulating surfaces will be explored.

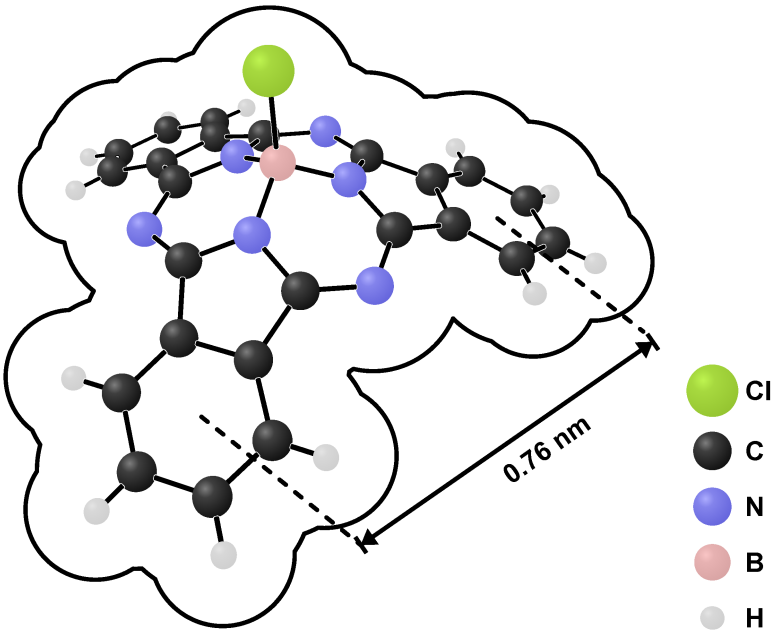

Figure 6.4: The SubPc molecule is cone shaped and consist of three isoindoline compounds arranged around a central boron-chlorine unit.

6.2 SubPc

Chloro[subphthalocyaninato]boron(III) (SubPc) [116–118] is a cone shaped molecule consisting of a central boron-chlorine unit connected to three isoindoline compounds (Fig. 6.4). The boron-chlorine bond length is 0.19 nm and the distance between the centers of the carbon rings is 0.76 nm. [117,119] An axial dipole moment is evident, with the negative charge at the chlorine atom. [120]

Crystalline SubPc

At room temperature, SubPc molecules arrange in an orthorhombic pattern mainly driven by intermolecular Van-der-Waals interactions. [117,118] The density has been determied to 1.52 g/cm^3. [117] For the sublimation enthalpy, the experiments presented in Fig. 6.5 yield a value of (2.57±0.16) eV following Eqn. 6.1. In literature, the sublimation enthalpy of crystalline SubPc has not been reported yet.

Assembly of SubPc on various surfaces

Similar to the before mentioned case of C_{60} on different substrate surfaces, also SubPc molecules interact very differently with different surfaces. Three different SubPc-substrate systems will be outlined shortly in the following, ordered by ascending interaction strength between molecules and the substrate surface.

On the KBr(001) surface, the interaction is very small, which yields a high mobility on the surface at room temperature.[121] This is evident from NC-AFM images revealing a strong clustering of the molecules at substrate step edges. No SubPc islands have been observed on terraces. However, if templating the surface, e.g. by creating small rectengular pits in the surface, molecules can be trapped. The area of a pit is filled with a single monolayer of SubPc molecules. Molecules are tilted with the chlorine head pointing downwards to the surface and arrange in adjacent rows inside the pits.

Submonolayer coverages of SubPc have been deposited on the Cu(100) surface.[122,123] During deposition, the substrate has been kept at room temperature, whereas it has been cooled to liquid nitrogen temperatures for STM measurements. Molecules arrange in a single layer with a highly ordered square (5×5) superstructure on the surface. However, molecules can adsorb in two distinct configurations. They can adsorb with the chlorine head pointing downwards to the surface and with the chlorine head pointing away from the surface. Depending on the applied bias voltage between STM tip and sample, molecules can be switched reversibly between both configurations. This flip-flop switching may be used, e.g., to store information.

On the Si(111)(7×7) surface, SubPc molecules have been deposited with the substrate held at room temperature.[124] Measurements have been performed at room temperature using STM. Like C_{60} molecules on this particular surface, SubPc molecules are almost immobile. This can be explained by the strong interaction of the surface's dangling bonds with the molecule. Molecules adsorb with the chlorine head facing down to the surface. Some molecules were observed to break apart. This is attributed to the strong interaction with the surface.

In summary, the interaction of SubPc with insulators seems to be small compared to metal or semiconducting surfaces. Additional nucleation sites, e.g. pits, are needed to induce a steered assembly on the surface. On metal surfaces, the interaction is intermediate, resulting in nicely ordered structures, not only on the Cu(100) surface, but also on Ag(111) and

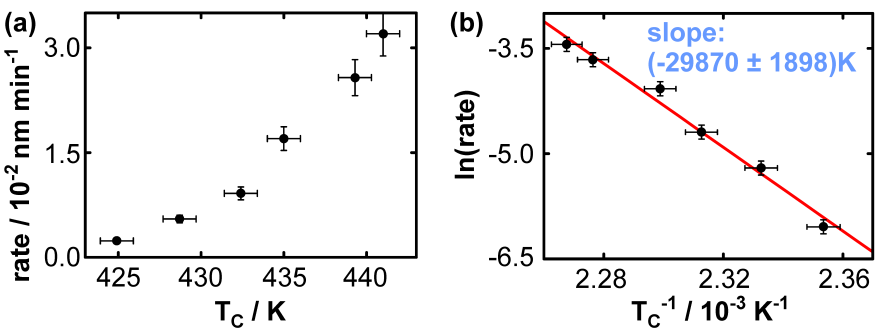

Figure 6.5: Deposition rates of SubPc at different temperatures with line of best fit.

Au(111) surfaces.[119,125–130] On the semiconducting Si(111)(7×7) surface, the molecule-substrate interaction is increased. The dangling bonds of this particular surface are interacting very strongly with the SubPc molecules. Thus, molecules are immobile and no ordered layers or islands form as diffusion is hampered on this surface.

Within this thesis, the adsorption of SubPc molecules on an insulating substrate surface is investigated. To direct the assembly of SubPc molecules, a subsequent and simultaneous codeposition of C_{60} molecules is explored. Experiments and further motivation for this bimolecular system are presented in Sec. 9.

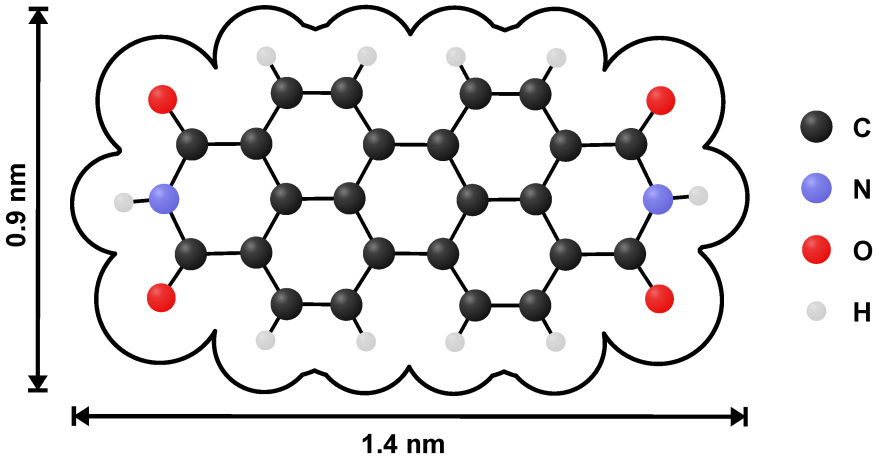

Figure 6.6: PTCDI is a planar molecule with an elongated and rectangular outer shape. It consists of fused six-membered benzene rings with a functionalized head/tail to facilitate intermolecular hydrogen-bonding.

6.3 PTCDI

The 3,4,9,10-perylenetetracarboxylic diimide (PTCDI) molecule is a planar molecule with an elongated, rectangular outer shape (Fig. 6.6). It mainly consists of fused six-membered benzene rings. However, at each, the head and tail, two carbon atoms are oxygen terminated and a carbon atom is substituted by a nitrogen atom.

Crystalline PTCDI

The arrangement of the molecules in their bulk crystalline structure is monoclinic and mainly driven by intermolecular hydrogen-bonding due to the molecule's oxygen and hydrogen terminations.[131–133] In the $(10\bar{2})$ plane of the three-dimensional packing, molecules are arranged in adjacent rows and rotated about $\pm 12°$ in alternating rows, as sketched in Fig. 6.7(a). Thus, each molecule is bonded with four hydrogen bonds within the rows. The interaction within the rows is stronger than between adjacent rows. Thus, PTCDI crystallites grow with needle-like shapes. The three-dimensional packing emerges from a stacking of the $(10\bar{2})$ plane. The density has been determined to $1.68\,\mathrm{g/cm^3}$.[133] For the sublimation enthalpy, the experiments presented in Fig. 6.8 yield a value of $(1.81 \pm 0.11)\,\mathrm{eV}$ following Eqn. 6.1. In literature, the sublimation enthalpy of crystalline PTCDI has not been reported yet.

Assembly of PTCDI on various surfaces

On various surfaces PTCDI molecules adopt different phases. In total, three different phases were reported from experiments, summarized in Ref. 134. All phases are driven by hydrogen-bondings. In the canted phase,

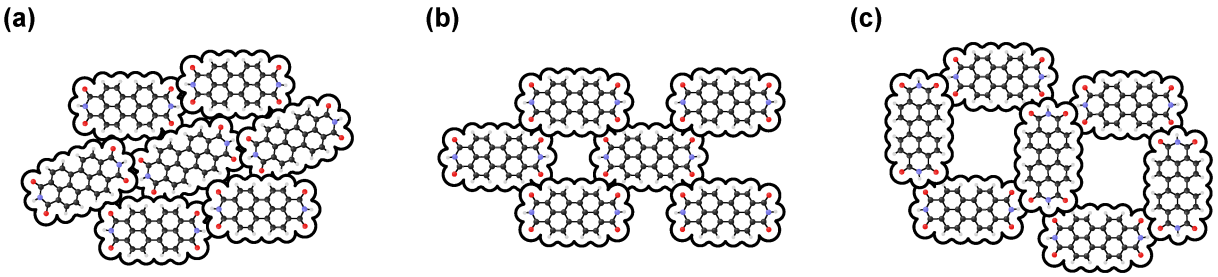

Figure 6.7: Schematic sketch of different phases PTCDI molecules adopt on various surfaces. All phases are governed by hydrogen bonding. (a) Canted phase. (b) Brick wall phase. (c) Domino phase.

molecules arrange in adjacent rows like sketched in Fig. 6.7(a). Molecules are rotated about ±12° in-plane with respect to the rows' direction. Thus, the arrangement is very similar to the $(10\bar{2})$ surface of a bulk PTCDI crystal. The intermolecular interactions along a row are assumed to be stronger than the interaction of molecules in adjacent rows. This anisotropy may be reflected in elongated island shapes. In the brick wall phase, the molecules also arrange in adjacent rows like sketched in Fig. 6.7(b). However, in comparison to the canted phase, intermolecular separations are larger within the rows and the molecules are not rotated, but aligned parallel the row's direction. The brick wall phase has only been observed on the NaCl(001) yet.[135] In the domino phase, the molecules are aligned to one another in a square pattern with succeeding molecules rotated by ninety degrees to each other (Fig. 6.7(c)). The domino phase has so far only been observed on the Au(111).[134] Comparing these three arrangements, the brick wall phase is assumed to be the energetically least favorable one. This is evident from experiments and calculations.[134,135]

Directly after deposition on the NaCl(001) surface at room temperature, two distinct types of island exist.[135] The first type are needle-shaped islands, which are two or more layers in height due to dewetting. They consist of molecules arranged in the canted phase. The second type are square-shaped islands, which are usually one layer in height and exhibit a brick wall phase. The latter type of island is metastable and dissolves in favor for the needle-shaped islands at room temperature within days.

Deposition of PTCDI on the Au(111) surface at room temperature yields islands, which are one layer in height.[134,136,137] The islands exhibit different phases of arrangement. All three phases, namely the canted, brick wall and domino phase, are coexisting on this particular surface. However, three more phases are predicted from calculations.[134]

PTCDI molecules have also been investigated on the HOPG,[138] MoS_2,[138] Pt(100),[133,139] Ag/Pt(111),[140] Ag/Si(111),[141] and the H-terminated Si(111) surfaces,[142] all revealing a canted arrangement of the molecules. Therefore, the canted arrangement seems to be the energetically most favorable structure.

Within this thesis, the adsorption of PTCDI molecules on an insulating

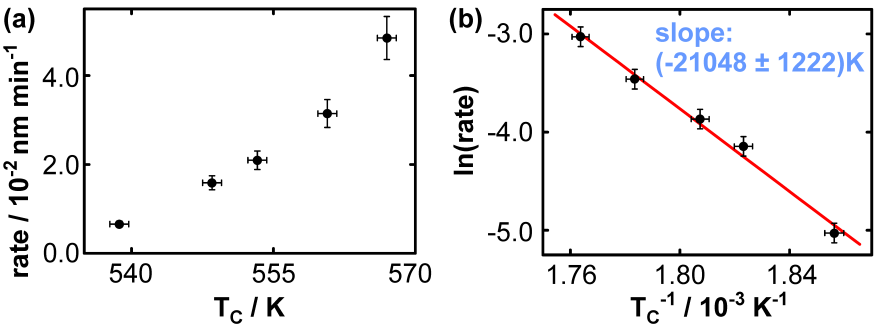

Figure 6.8: Deposition rates of PTCDI at different temperatures with line of best fit.

substrate surface is investigated. To direct the assembly of PTCDI molecules, a subsequent and simultaneous codeposition of C_{60} molecules is explored. Experiments and further motivation for this bimolecular system are presented in Sec. 10.

7 C_{60} molecules on the TiO_2 (110) surface

Contents

In this part, the principles of adsorption of C_{60} molecules on the rutile TiO_2 (110) surface are studied by non-contact atomic force microscopy under ultra-high vacuum conditions. After preparation of the bare substrate according to Sec. 5.1, C_{60} molecules were deposited with a rate of 0.12 ML/min (1 ML equals to 0.2 C_{60} molecules per TiO_2 (110) unit cell) onto the surface, which was held at room temperature (see Sec. 6.1).

For using molecules in future molecular electronic, systems are needed that provide highly ordered as well as contaminant and defect-free layers.[143,144] Such a system might be provided by C_{60} molecules on the TiO_2 (110) surface. Therefore, first, C_{60} islands/layers on the TiO_2 (110) surface are produced and characterized (Sec. 7.1). Islands were of striking perfection with a low density of defects. This is surprising as the TiO_2 (110) surface exhibit a rather large density of intrinsic defects.[25,77]

In NC-AFM imaging on C_{60} islands, an inversion of the imaging contrast while reducing the tip-sample distance was found. This imaging contrast

is discussed and explained with the help of model simulations in the proceeding section (Sec. 7.2).

After creation of nearly defect-free C_{60} islands in the first step and clarification of NC-AFM imaging contrasts in the second step, the third step is dedicated to modifying these well-ordered C_{60} islands (Sec. 7.3). The inner structure of several islands is modified by the AFM tip as well as whole islands are removed.

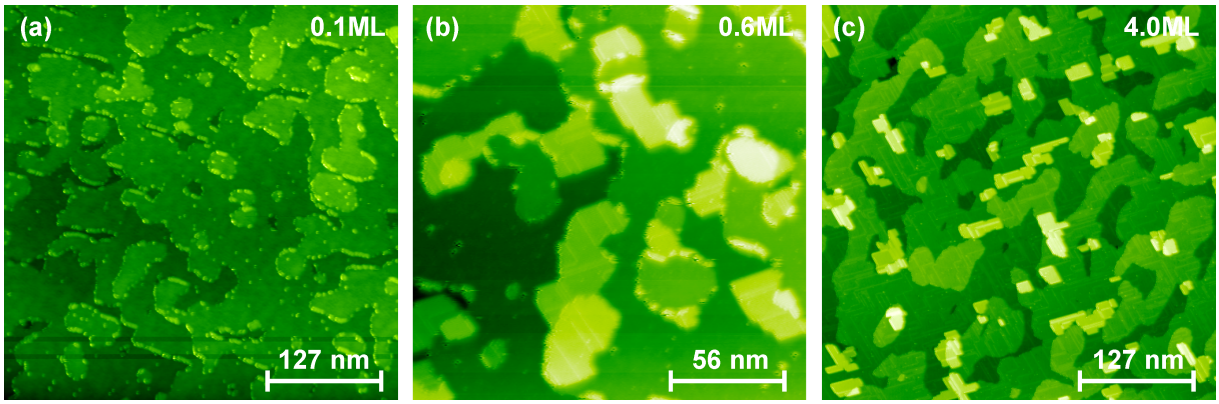

Figure 7.1: C_{60} on TiO_2 (110) at different coverages (topography images). (a) 0.1 ML C_{60} , 440 nm x 440 nm. (b) 0.6 ML C_{60} , 194 nm x 194 nm. (c) 4.0 ML C_{60} , 440 nm x 440 nm.

7.1 Growth of ordered C_{60} islands

In this section, the growth mode of C_{60} on the TiO_2 (110) surface is analyzed. A closer look will be taken at the superstructure and defects of C_{60} islands, including domain boundaries.

Growth mode

Upon submonolayer deposition, molecules are observed to preferentially adsorb at step edges as shown in Fig. 7.1(a). With increasing coverage, islands appear to grow from substrate step edges onto the lower terraces as seen in Fig. 7.1(b). By far the most islands are attached to a substrate step edge and only very few grow directly on terraces, the latter islands are ascribed to nucleation at defect sites. For a statistical analysis, the shape of the islands is investigated in more detail. In total 381 islands from eight different images taken at different submonolayer coverages were analyzed. A histogram of the aspect ratios (length divided by the width for the best fitting rectangle) is depicted in Fig. 7.2. This histogram reflects the overall rather compact shape of the C_{60} islands. For higher coverages, large C_{60} islands are formed in a Stranski-Krastanov growth mode (Sec. 4), covering the entire substrate as seen in Fig. 7.1(c). Single C_{60} molecules on terraces are observed rarely; some of them are evident in Fig. 7.3(a). These individual molecules are assumed to be anchored at surface defects. The density of the most prevalent surface defects, namely single and double hydroxyls originating from oxygen vacancies amounts to 4% ML for this particular sample after 19 cycles of sputtering and annealing (note: 1 ML of defects equals to one defect per TiO_2 (110) unit cell).[77] As this density is much higher than the density of the individual C_{60} molecules observed in the experiments, the fixed C_{60} molecules must be anchored at other defect sites that are not yet identified. These fixed molecules are supposed to act as nucleation seeds for the growth of the few C_{60} islands found on terraces.

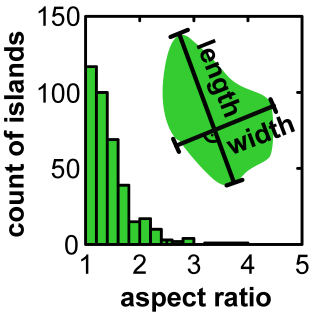

Figure 7.2: Distribution of aspect ratios of island shapes.

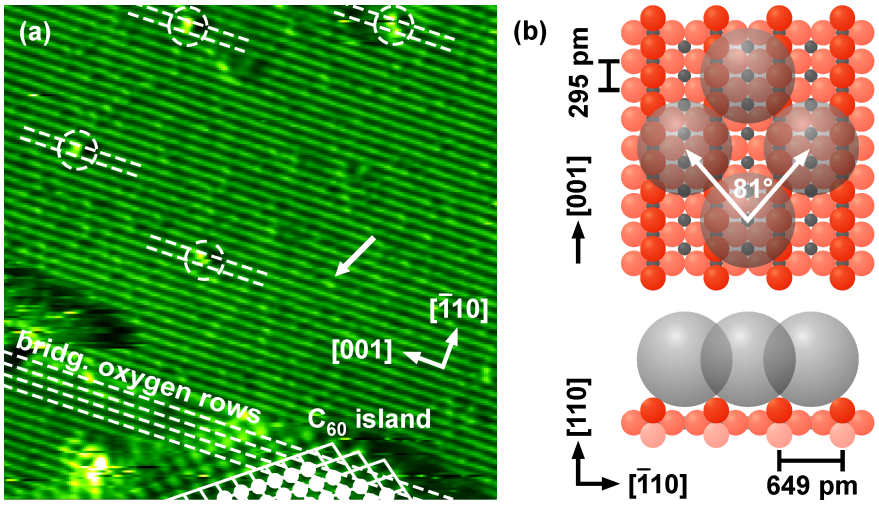

Figure 7.3: (a) Single C_{60} molecules and C_{60} islands on an area of 25 nm x 25 nm (frequency shift contrast). Single C_{60} molecules (dashed circles) and hydroxyl defects (one is indicated by an arrow) on a terrace (upper part) and C_{60} island attached to a step edge (lower part) are shown. (b) Model of the C_{60} island structure. The C_{60} molecules are sketched with their Van-der-Waals radii (≈1.0 nm).[98] The molecules are centered in the troughs formed by the bridging oxygen rows. The exact lattice site within the troughs, however, cannot be determined and is arbitrary in the given model.

C_{60} superstructure

In the lower part of Fig. 7.3(a) a C_{60} island edge is shown. The bridging oxygen rows can be identified by the position of hydroxyl defects, which are known to form on the bridging oxygen rows from oxygen vacancies through water adsorption.[77,82] In this particular image the bright (larger negative frequency shift) rows correspond to the substrate bridging oxygen rows running along the [001] direction, since surface defects (single and double hydroxyls) appear as brighter spots on these rows (one is indicated by an arrow).[82] In the upper half of the image, four additional features are found (dashed circles) that are much larger than typical surface defects. These features are ascribed to single C_{60} molecules, adsorbed between the bridging oxygen rows (dashed lines). In the lower half of the image, a C_{60} island anchored to a substrate step edge is shown. A comparison of C_{60} covered and uncovered areas yields that also molecules within an island adsorb in the troughs formed by the bridging oxygen rows. The C_{60} molecules arrange in a centered rectangular superstructure, as sketched in Fig. 7.3(b). The angle spanned by the basis vectors of the superstructure amounts to (81±2)°. The nearest-neighbor distance between the molecules is measured to (1.00±0.02) nm, the same as in the bulk C_{60} crystal (1.00 nm).[99] As atomic resolution is lost at C_{60} island edges, the exact adsorption site in [001] direction cannot be determined. The measured dimensions do, however, agree with a c(5×2) superstructure within the error of the length measurements. It was not possible not resolve any structure within the molecules, which might be due to the fact that the molecules possess sufficient thermal energy for rotating around their center as in bulk C_{60}.[100] These findings suggest that the assembly at room temperature is driven by the C_{60} intermolecular interaction, while the substrate

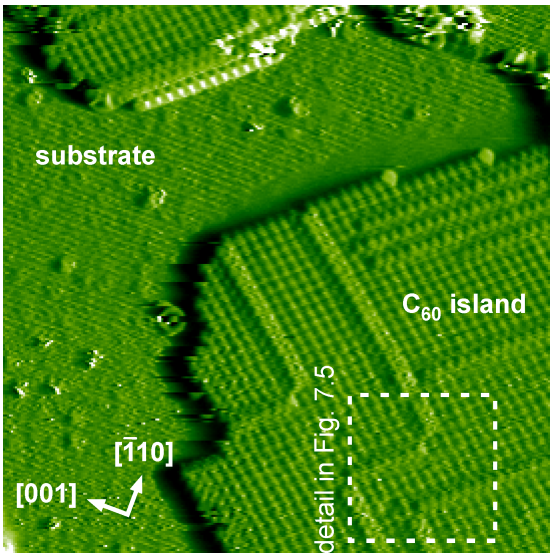

Figure 7.4: Frequency shift image showing a typical C_{60} island. Frame size is 48 nm x 48 nm. Backward scan (from right to left) taken at a frequency shift setpoint of -9.8 Hz.

is templating the molecules in between the bridging oxygen rows. Moreover, the C_{60} molecules seem to possess sufficient kinetic energy to diffuse on the surface. Consequently, the island growth requires nucleation sites such as step edges or pinned molecules.

A recent study using STM on the TiO_2 (110) 1×2 cross-link reconstructed surface has revealed a similar behavior.[109] In this study, the C_{60} molecules have been observed to anchor at the cross-link sites and to grow along the [001] direction in the troughs. The observed C_{60} adsorption position on top of the Ti rows agrees with the findings in this study. It has been argued that C_{60} anchors to the undercoordinated Ti cations while the intermolecular interaction is governed by van-der-Waals interaction, in good agreement with what is observed on the unreconstructed surface.

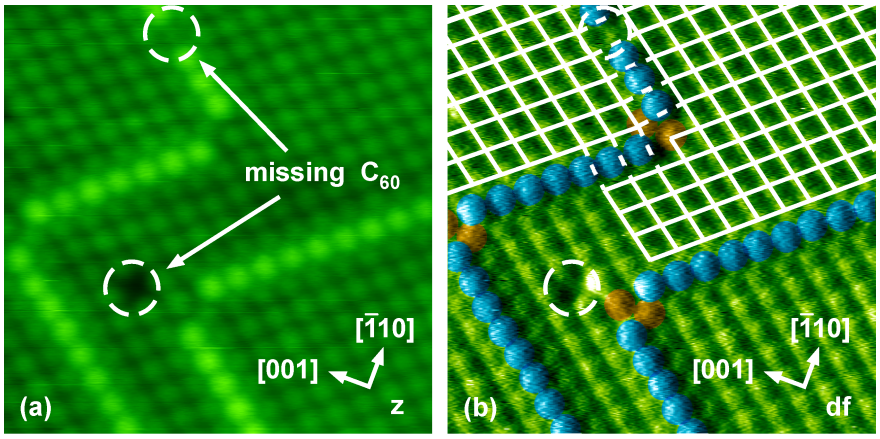

Figure 7.5: Anti-phase boundaries due to stacking faults. C_{60} island, showing domain boundaries and defects in topography (a) and frequency shift channel (b); 14 nm x 14 nm. Two defects are marked: a missing C_{60} molecule within a protruding strand and a single missing molecule within a C_{60} island.

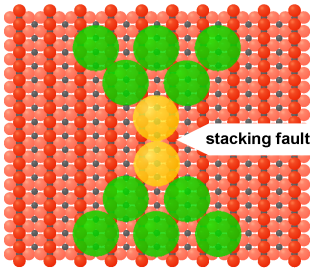

(a)

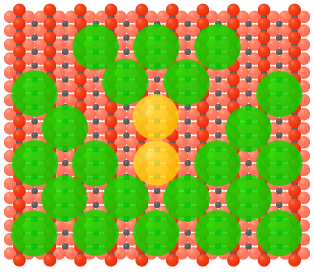

(b)

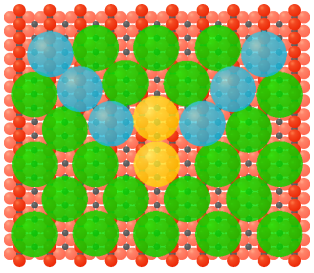

(c)

Figure 7.6: Anti-phase boundaries due to stacking faults. (a) C_{60} molecules causing a stacking fault are colored yellow. (b) During island growth a gap is created between two islands growing together, which cannot be occupied by C_{60} molecules. (c) C_{60} molecules adsorb on this gap (colored blue), resulting in protruding rows of single C_{60} strands, running in the [2$\bar{2}$5] and [$\bar{2}$25] directions.

Domain boundaries and defects on the C_{60} islands

An impression of the regular order and shape of the islands is shown in Fig. 7.4, exhibiting an island after 0.5 ML deposition. A closer inspection of the C_{60} islands reveals bright straight lines of C_{60} molecules, running parallel to the basis vectors of the superstructure along the [2$\bar{2}$5] and [$\bar{2}$25] directions (Fig. 7.5). These lines are also observed at higher coverages, as shown in Fig. 7.7, representing the molecular ordering after 4.0 ML deposition. The straight lines consist of single strands of molecules slightly protruding from the C_{60} islands. Since these lines do not occur periodically in any way, it can be excluded that they are due to a lattice mismatch between the C_{60} superstructure and the substrate unit cell. Neither underlying surface defects such as oxygen vacancies or hydroxyls can be the reason, considering that the defect density is much higher than the number of protruding lines. A plausible explanation for these lines of protruding molecules are, however, anti-phase boundaries originating from stacking faults.

It is proposed that such domain boundaries originate from two islands growing together. If two molecules are in close contact within a trough, an anti-phase boundary is created as illustrated by the yellow-colored C_{60} molecules in Fig. 7.6(a). This stacking fault results in a gap between the two islands that cannot be occupied by C_{60} molecules due to the limited space (Fig. 7.6(b)). However, molecules adsorb on top of these boundaries between two coalescing islands (colored blue in Fig. 7.6(c)). More precisely, these molecules lie on the imaginary center of the area spanned by four molecules (two of each island), which corresponds to a maximization of the number of nearest-neighbors.

Considering the size of the C_{60} islands and the typical density of surface hydroxyl defects, which is in the range of 2% ML to 6% ML in our experiments[77], surface defects do exist underneath the C_{60} islands. On the C_{60} islands, however, structural imperfections other than domain boundaries are observed only very rarely. These C_{60} island defects are single missing molecules as those shown in Fig. 7.5. The number of C_{60} island defects is by far too small to account for the number of underlying substrate defects, indicating that surface defects do not perturb the island growth. Our results, therefore, demonstrate that defect-free C_{60} layers can be prepared on a surface with an initially high density of surface defects.

Conclusion

In summary, it is evident that C_{60} molecules are mobile on the rutile TiO_2 (110) surface at room temperature. Single C_{60} molecules diffuse over the surface and require nucleation sites for island growth, such as step edges or substrate defects. Molecules adsorb in the troughs formed

by the bridging oxygen rows of the substrate. The C_{60} island superstructure is found to be centered rectangular with an angle of (81±2)° spanned by the basis vectors, in agreement with a c(5×2) superstructure. Although the underlying TiO_2 (110) surface is known to exhibit a high density of defects, the C_{60} islands are almost free of defects and have a regular, compact shape.

The system introduced here offers a great potential for the deposition of highly ordered monomolecular layers of C_{60} on an insulating substrate. Deposition in a nano-stencil system[145] would facilitate the fabrication of shaped nano-pads for molecular electronic applications e.g. as molecular contacts.

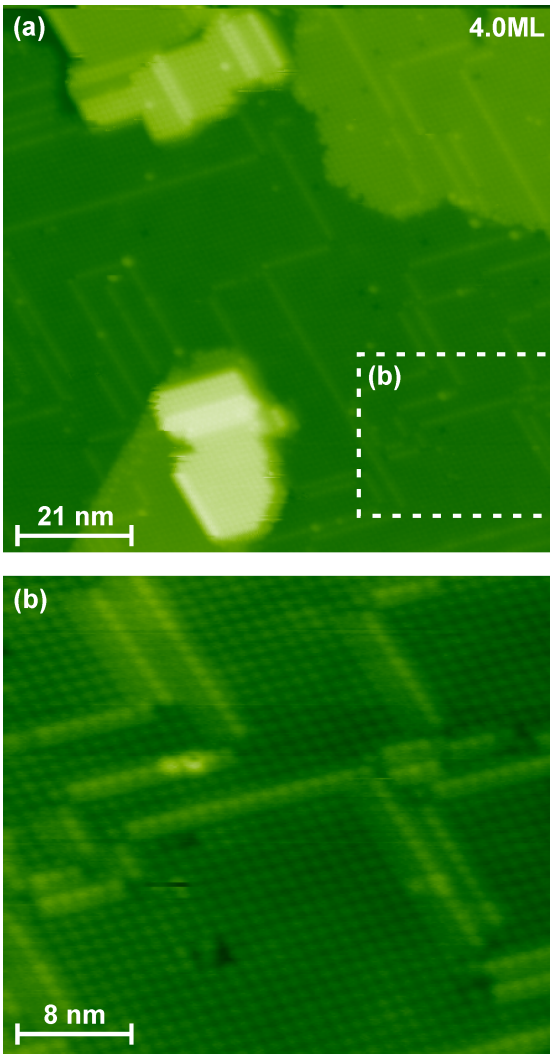

Figure 7.7: NC-AFM images (topography) of C_{60} on TiO_2 (110) at a coverage of 4.0 ML. Different plain C_{60} terraces are evident with protruding rows running along the surface, which ware assigned to domain boundaries.

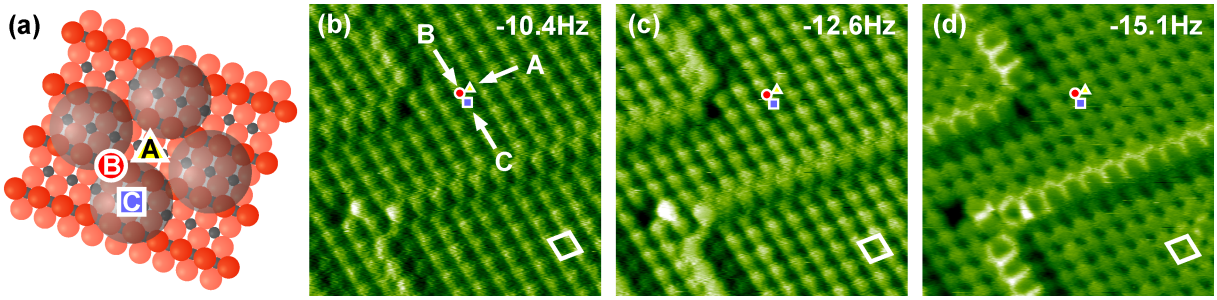

7.2 Contrast inversion on C_{60} islands

In this section, the distance dependent contrast on C_{60} islands in NC-AFM imaging is analyzed. While STM images the surface electronic structure, the surface force field is probed with NC-AFM. Compared to STM, however, the understanding of contrast formation in NC-AFM is far less mature. Understanding and interpreting experimental NC-AFM data has been addressed recently investigating both, bare as well as adsorbate-covered surfaces.[13,81,94,146–148] Contrast formation of single C_{60} molecules has been studied on Si(111) (7×7), revealing C_{60} molecules that are imaged as depressions.[107] In this study it has been suggested that this contrast inversion might originate from a jump of the tip above the C_{60} molecule, entering into the regime of negative slope in the $df(z)$ curve. Also when imaging extended C_{60} islands on Si(111) (7×7) contrast inversion was observed and assumed to be due to a change in the vibration amplitude compared to the topography signal.[114]

Here, the interaction between C_{60} molecules within a C_{60} island on rutile TiO_2 (110) and the scanning probe tip is studied. The contrast formation was studied in dependence on the tip-sample distance. Far away from the sample surface, each C_{60} molecule is imaged as a bright feature. When decreasing the tip-sample distance, the contrast changes, eventually resulting in C_{60} molecules imaged as depressions. The resulting relation between measured frequency shift values at defined positions on the molecular island versus the tip-sample distance is plotted as frequency shift-distance ($df(z)$) curves. The results reveal crossing points in the $df(z)$ curves at different surfaces positions, explaining why contrast inversion is observed on the C_{60} molecules upon decreasing the tip-sample distance. Simulations based on a simple model system were performed, closely resembling the experimental observations. Comparing these simulations with the experimental results allows for gaining insight into the interaction between C_{60} molecules and the scanning probe tip. In particular, the observed change in contrast can be assigned to crossing points in the attractive region of tip-sample interaction, i.e., the observed contrast inversion is not due to

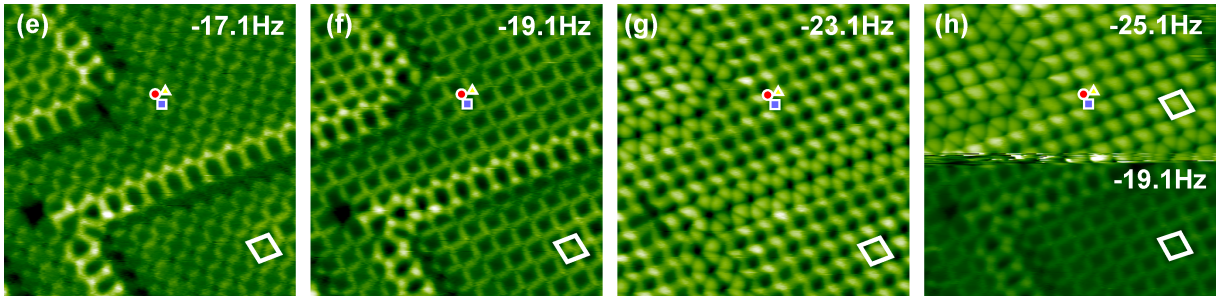

Figure 7.8: Contrast inversion on a C_{60} island. Series of quasi constant height images upon decreasing the tip sample distance. Frame size is 12 nm x 12 nm. Forward scan (from left to right) images with the frequency shift setpoint noted in the images. The frequency shift setpoint was increased successively from image (b) to (h), inducing a change in imaging contrast. Three positions are marked in every image, corresponding to the positions indicated in the schematic shown in (a). At these positions, the measured frequency shift was analyzed and compiled in Fig. 7.9(a), comparable to *df*(*z*) curves.

entering into the repulsive regime. This study emphasizes the fact that a detailed distance-dependent analysis is usually required for unambiguously identifying molecular positions within a molecular island.

In the present experiments, the distance feedback was not switched off completely as it is needed to compensate for sample tilt and thermal drift in *z*-direction. Consequently, all images shown here are taken with slow feedback loop settings in which the vertical movement following the corrugation of the molecules within an island is in the order of ±5 pm, resulting in quasi constant height mode images, i.e., the *df* contrast is presented. In the following, distance-dependent *df* curves are discussed, thus, presenting *df*(*z*) curves would be the most direct way of data presentation. However, the experiments require site specificity which is only provided when lateral drift is negligible. Usual AFM setups without special precautions such as atom tracking [149] do not provide high enough drift stability. In order to arrive at meaningful data, the measured *df* values are presented in dependence on the *df* setpoint. This approach is justified as the tip-sample distance is controlled by the frequency shift setpoint, which represents the average frequency shift of the *df* images. As measurements are exclusively in the attractive regime (will be proven later) the frequency shift setpoint is monotonically dependent on the tip-sample distance. Thus, the *df* setpoint serves as a measure for the tip-sample distance in the experiments. The images are displayed such that bright areas correspond to high attractive interaction while dark corresponds to less attractive or even repulsive interactions. [13]

Experimental Results

As established in the previous section, C_{60} molecules are known to arrange in a rhombic superstructure on the rutile TiO_2 (110) surface with an angle of (81±1)° and with the C_{60} molecules lying centered in the troughs formed by the bridging oxygen rows, as shown in Fig. 7.3. Protruding molecular rows are observed on the C_{60} islands, which are ascribed to domain boundaries originating from stacking faults. The molecules in the domain boundary are directly surrounded by six other C_{60} molecules; four

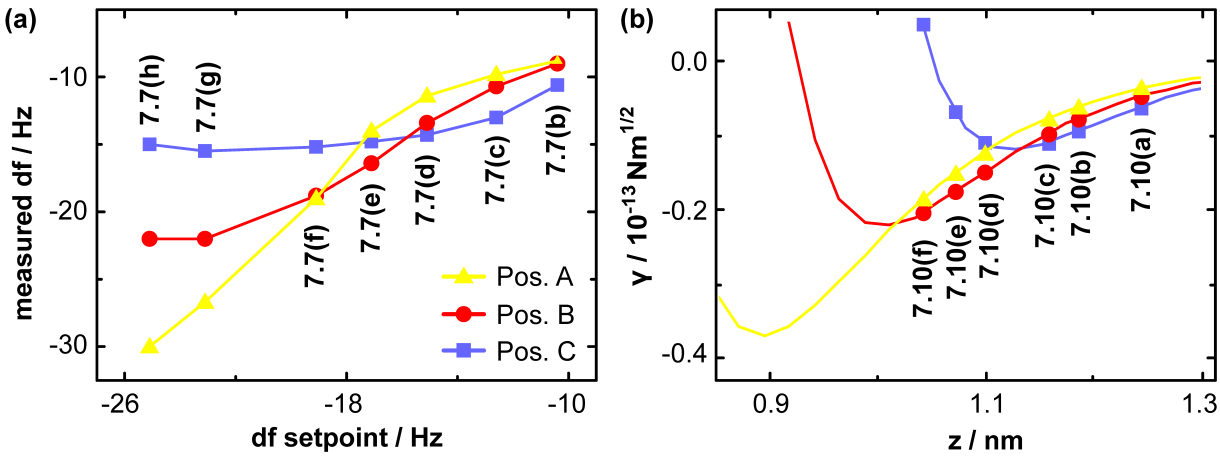

Figure 7.9: (a) Experimentally obtained frequency shift at defined sample positions plotted against the preset frequency shift setpoints. The error of the displayed frequency shift values amounts to ±0.3 Hz approximately. The curves are comparable to *df*(*z*) curves as the frequency shift setpoint is related to the mean height over the surface. (b) Corresponding simulated frequency shift versus distance curves at the same positions on the C_{60} islands. Note that γ is directly proportional to *df*.

in the underlying C_{60} islands and two in the domain boundary.

In Fig. 7.8(b) a zoom into the marked area from Fig. 7.4 is depicted, showing a C_{60} layer with domain boundaries. In the following images (c)-(h) the tip-sample distance was decreased successively by changing the frequency shift setpoint from -10.4 Hz to -25.1 Hz. When scanning at different frequency shift setpoints, different contrasts on the molecular island are observed. This evolution in contrast was reproducible obtained when retracting the tip afterwards. In particular, no sign for a tip change was observed in Fig. 7.8(a)-(g), i.e., the observed changes in contrast can be ascribed to the change in tip-sample distance solely. In the middle of Fig. 7.8(h) the tip interacted strongly with the C_{60} island. However, the contrast in NC-AFM imaging was the same afterwards, which can be obtained by comparing Fig. 7.8(f) with the lower part of Fig. 7.8(h). The increased interaction in the middle of Fig. 7.8(h) will be analyzed in the following section (Sec. 7.3). In general, imaging was observed to be rather stable, especially when compared to imaging on bare TiO_2 (110). One explanation for these stable imaging conditions could be an initial transfer of C_{60} molecules to the very end of the tip. All images would then be obtained with a rather stable C_{60} tip apex.

To follow the steps of change in contrast, three different positions on the molecular island are marked in different colors in the schematic in Fig. 7.8(a): position A (triangle) is in the center of the C_{60} unit cell, position B (circle) between two nearest-neighbor C_{60} molecules and position C (square) on top a C_{60} molecule. The same positions are also indicated in the NC-AFM images in Fig. 7.8(b)-(h). For each NC-AFM image, the measured frequency shifts at these three positions were averaged over eight unit cells and plotted against the preset frequency shift setpoint for each image (Fig. 7.9(a)). The error of this values amounts to ±0.3 Hz approximately. Within the range of tip-sample distances considered here, the mea-

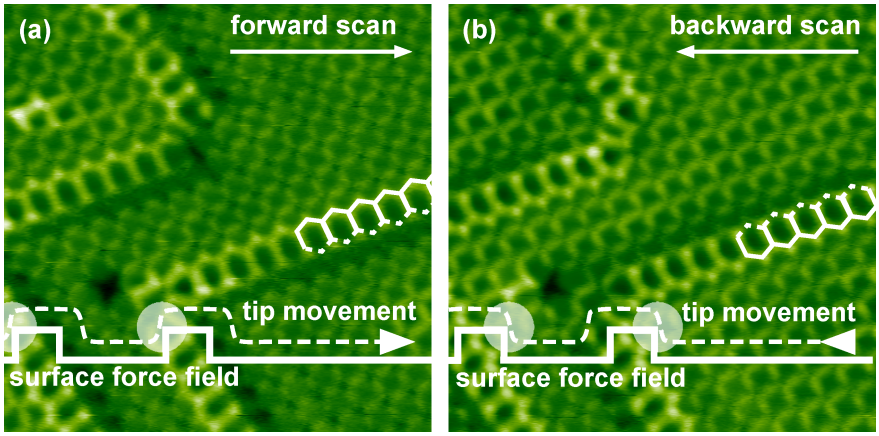

Figure 7.10: Comparison of forward and backward scans. Quasi constant height images with frequency shift setpoint -17.1 Hz. Frame size is 12 nm x 12 nm. (a) Forward scan (from left to right): the tip approaches the domain boundary from the left side, resulting in a domain boundary structure that appears open on the lower right side. (b) Backward scan showing a structure that is open on the upper left side. Combining both, forward and backward scans, the overall structure of the domain boundary reveals a hexagonal shape.

sured frequency shifts represent a monotonically increasing curve. This indicates that measurements are in the attractive regime solely.[13] Between the images in Fig. 7.8(c) and (d) the tip-sample distance was decreased by changing the frequency shift setpoint from -12.6 Hz to -15.1 Hz. This results in a less corrugated appearance of the C_{60} molecules in Fig. 7.8(d), as the difference in measured frequency shift at positions C and B is reduced. In the image in Fig. 7.8(e), taken at a frequency shift setpoint of -17.1 Hz, the contrast has changed. Now position B between the C_{60} molecules is brighter than position C on the C_{60} molecules, which can also be seen in the crossing of the corresponding curves in Fig. 7.9(a). Position A in the center of the unit cell appears, however, still as darkest position. This corresponds to the least attractive interaction at sample position A.

Upon further decreasing the tip-sample distance by changing the frequency shift setpoint to -19.1 Hz (Fig. 7.8(f)) position A gets as bright as position B, while position C on top of a C_{60} molecules appears darkest. Finally, in Fig. 7.8(g) and (h) position A becomes brightest. Thus, in comparison to Fig. 7.8(b) the contrast has inverted completely. In Fig. 7.8(b) the order in attractive tip-molecule interaction is A, B, C whereas in Fig. 7.8(h) it is C, B, A. This is also seen in the curves given in Fig. 7.9(a).

The same change in contrast is observed at the domain boundaries. As the boundaries are protruding from the underlying C_{60} layer, the contrast inversion takes place already at larger tip-sample distances, since the tip approaches the protruding features more closely compared to the C_{60} island. The contrast pattern on top of the domain boundaries shows a hexagonal structure, corresponding to the four directly surrounding C_{60} molecules of the underlying C_{60} layer and the two neighboring molecules in the domain boundary.

This hexagonal structure appears not completed, but open at the rear side relative to the fast scan direction (Fig. 7.8(d)-(f)). This can be accounted to a feedback effect, which can be clearly seen when comparing

forward and backward scans of an image, as shown in Fig. 7.10(a) and (b), respectively. When considering the forward scan (fast scan direction from left to right) the tip is approaching the left-hand site of the domain boundary very closely. Scanning with slow feedback loop settings, the tip is retracted slowly a few 10 pm, resulting in a slightly larger tip-sample distance at the right-hand side of the domain boundary. Therefore, the bright rim is not seen at the right-hand side of the domain boundary. The same effect is observed vice versa in a backward scan, resulting in a hexagonal structure that is open to the left as shown in Fig. 7.10(b).

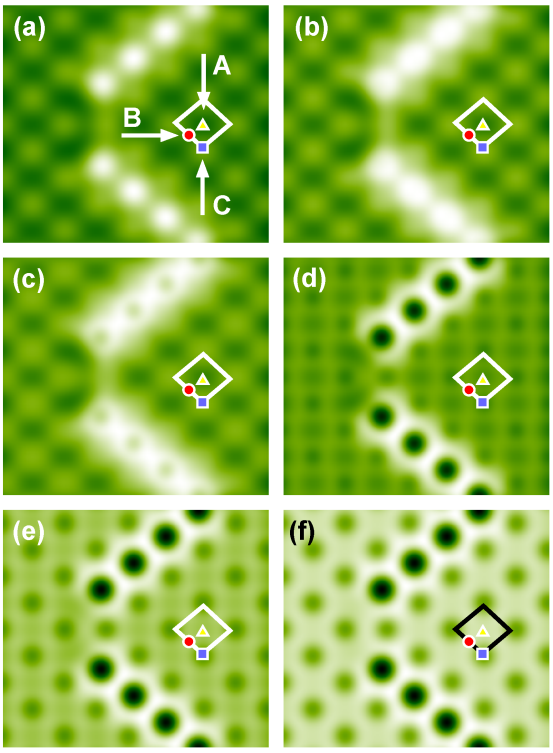

Figure 7.11: Simulated images showing the normalized frequency shift at different tip-sample distances over a C_{60} island with a domain boundary.[150,151]

Model Simulations

To gain insight into the observed contrast formation and to rule out influences of the feedback loop, simulations were performed using a simple model based on a Morse potential. This potential is used for modeling a pairwise, additive interaction between each single C_{60} molecule and the probing tip. For the simulations it is assumed that a single C_{60} is pinned to the tip. This is motivated by the experimentally observed stable imaging conditions mentioned before, which are rather unique for C_{60} molecules on TiO_2 (110) compared to bare TiO_2 (110). The model was set up and simulated by (Johannes Gutenberg-Universität Mainz).[150,151] The

simulation results are shown in Fig. 7.11(a)-(f). In Fig. 7.9(b) the normalized frequency versus distance curves are shown. The heights, at which the images in Fig. 7.11(a) to (f) were calculated, are indicated in Fig. 7.9(b) by the corresponding symbols. The simulated images nicely reproduce the experimentally observed contrast formation. At distances far away from the surface, the C_{60} molecules appear bright, while upon approaching the tip towards the sample results in a contrast inversion. In Fig. 7.11(f), the on top position of the C_{60} molecules appears dark while the area in between C_{60} molecules is imaged bright. Thus, this simulation confirm that the experimentally observed contrast is due to change in tip-sample interaction at different tip-sample distances. In particular, we can conclude that the used slow feedback loop settings do not influence the qualitative behavior, as our true constant-height simulation results show an excellent agreement with the experimental results.

Besides the images, our simulations also confirm the experimentally observed $df(z)$ curves in a sense that we can reproduce the order of the crossing point in the three curves at positions A, B and C. We see, however, that the simulated curves deviate from the experimental ones as the simulated $df(z)$ curves at position C show negative slope at the crossing points of A and B. This is in contrast to what is observed experimentally and illustrates the limits of this simple model. It has been reported before that the Morse potential fails to model the repulsive regime as elastic contact forces have to be considered.[152]

Conclusion

The contrast formation of C_{60} molecules on the rutile TiO_2 (110) is studied at different tip-sample distances. When imaging the molecules far away from the surface, the on top position appears bright while the area in between four molecules is imaged dark. Upon approaching the tip towards the surface, this contrast changes and is eventually inverted. The observed contrast inversion was simulated using a simple model system based on a Morse potential. The study reveals that contrast inversion is observed due to crossing points in the frequency shift-distance curve. In the present case, these crossing points are not related to the onset of the repulsive regime. This study illustrates that an unambiguous identification of molecular positions within a molecular island using NC-AFM can require distance-dependent measurements of the contrast formation.

7.3 Manipulation of C_{60} islands

In this section, the manipulation of C_{60} islands with NC-AFM is presented and analyzed. Employing self-assembly in combination with direct patterning methods such as manipulation might allow for creating an broad variety of structures. The most direct fabrication method of nanostructures is tip-induced manipulation,[6] since the tip is controllable at the subnanometer scale.

Atomic and molecular manipulation has been studied extensively on metal surfaces using scanning tunneling microscopy (STM) and a rather comprehensive understanding of the manipulation process has been achieved.[4,5,153–155] Using NC-AFM, however, controlled manipulation of single atoms and atom size defects has been achieved in very few cases only. Compared to manipulation using the STM, only limited understanding has been gained so far based on experimental data[51–53,156–160] and theoretical calculations.[161–163] Lateral manipulation can be triggered by lowering the energy barriers for hopping processes due to attractive interactions between tip and surface adatoms[52,161] or due to repulsive interaction between the tip and surface adsorbates/atoms.[51] Like in STM, pulling[164] as well as pushing[53] manipulation mechanisms were proposed. In contrast to previous manipulation experiments using non-contact atomic force microscopy, well-controlled manipulation of large molecules is demonstrated here.

The system of C_{60} molecules on the rutile TiO_2 (110) surface is investigated with NC-AFM at room temperature. Tip-induced modification of C_{60} islands due to clear repulsive interactions between tip and molecules is demonstrated. Thereby, pits in well-ordered islands were created and domain boundaries were moved on the islands. Additionally, altering and removal of complete C_{60} island is demonstrated.

Manipulation on C_{60} islands

The starting configuration is the close-packed C_{60} island as presented in Fig. 7.5. As mentioned above, the protruding molecular rows are ascribed to domain boundaries originating from stacking faults. In Fig. 7.12(a), the image shown in Fig. 7.5(a) is reproduced.

When scanning on the C_{60} islands, holes were created into these islands by scanning at increased frequency shift setpoints. An example is shown in Fig. 7.12(a) and (b). Image (a) was recorded at a frequency shift setpoint of -10.4 Hz. From this point, the frequency shift setpoint was increased stepwise in the following images, resulting in contrast inversion as discussed in the previous section. The corresponding images can be seen in Fig. 7.8(b)-(h). Very stable imaging was possible until a setpoint of -25.1 Hz

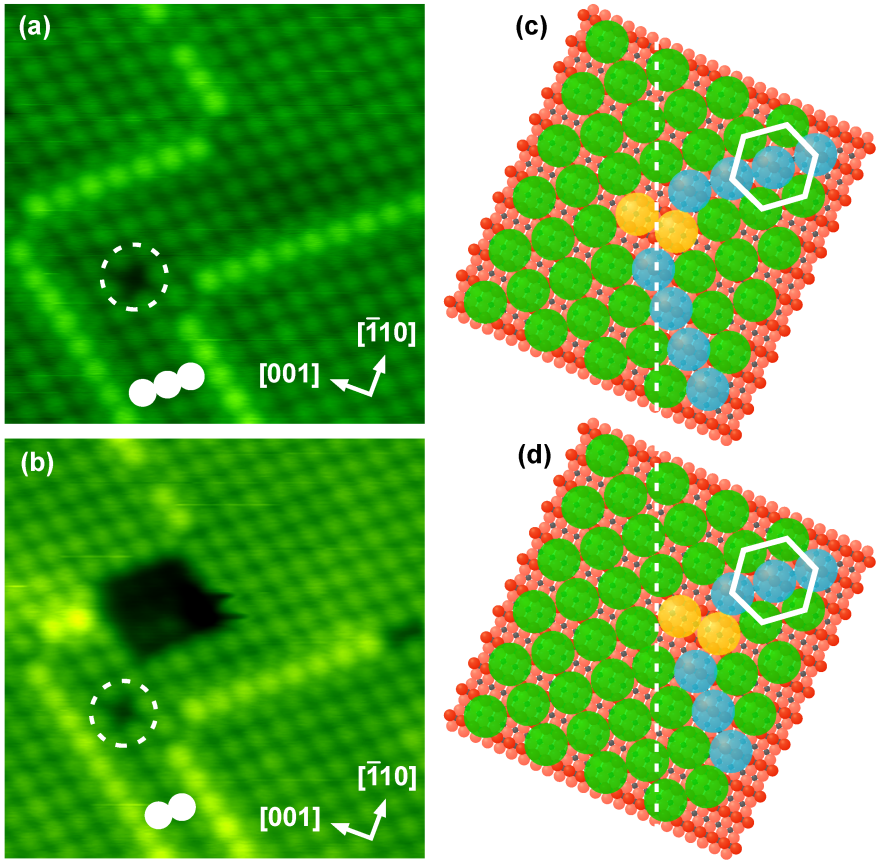

Figure 7.12: Comparison of two NC-AFM forward-scan images (14 nm x 14 nm, topography) at a frequency shift setpoint of -10.4 Hz (a) before and (b) after a stepwise increase of the frequency shift setpoint to -25.1 Hz (this series can be seen in the previous section). At a frequency shift setpoint of -25.1 Hz, the interaction between tip and C_{60} molecules induced an almost quadratic hole by the removal of seventeen molecules (twelve from the plain C_{60} island and five from the upper domain boundary). Additionally, a reordering of the left domain boundary was observed. In both images (a) and (b), a single missing C_{60} molecule is marked as a reference point. A model of the situation before and after the reordering of a domain boundary is sketched in (c) and (d), respectively

was reached (Fig. 7.8(h)). At this setpoint, the tip interacts sufficiently with the C_{60} molecules to remove C_{60} molecules from the island.

In Fig. 7.13(a) and (b) (which is the middle part of Fig. 7.8(h)) the frequency shift channel (left panel) and the dissipation channel (right panel) are shown for the backward and forward scan, respecively. The upper part in the NC-AFM images in Fig. 7.13 was scanned at a setpoint of -25.1 Hz. Near the stacking fault (see area enclosed by the dotted lines), manipulation occurs. In the lower part of the image, the frequency shift setpoint was lowered to -19.1 Hz, again resulting in stable imaging. The contrast is the same again as was seen at -19.1 Hz before the manipulation process (Fig. 7.8(f)).

The frequency shift images for the forward and backward scan show full contrast inversion at a setpoint of -25.1 Hz (i.e., the C_{60} molecules appear dark while the areas in between the molecules appear bright). In the dissipation channel molecular contrast is faintly seen.

In the following, every scan line in between the area where manipulation happened (see area enclosed by the dotted lines) of the frequency shift and dissipation images (each with forward and backward scan) is analyzed

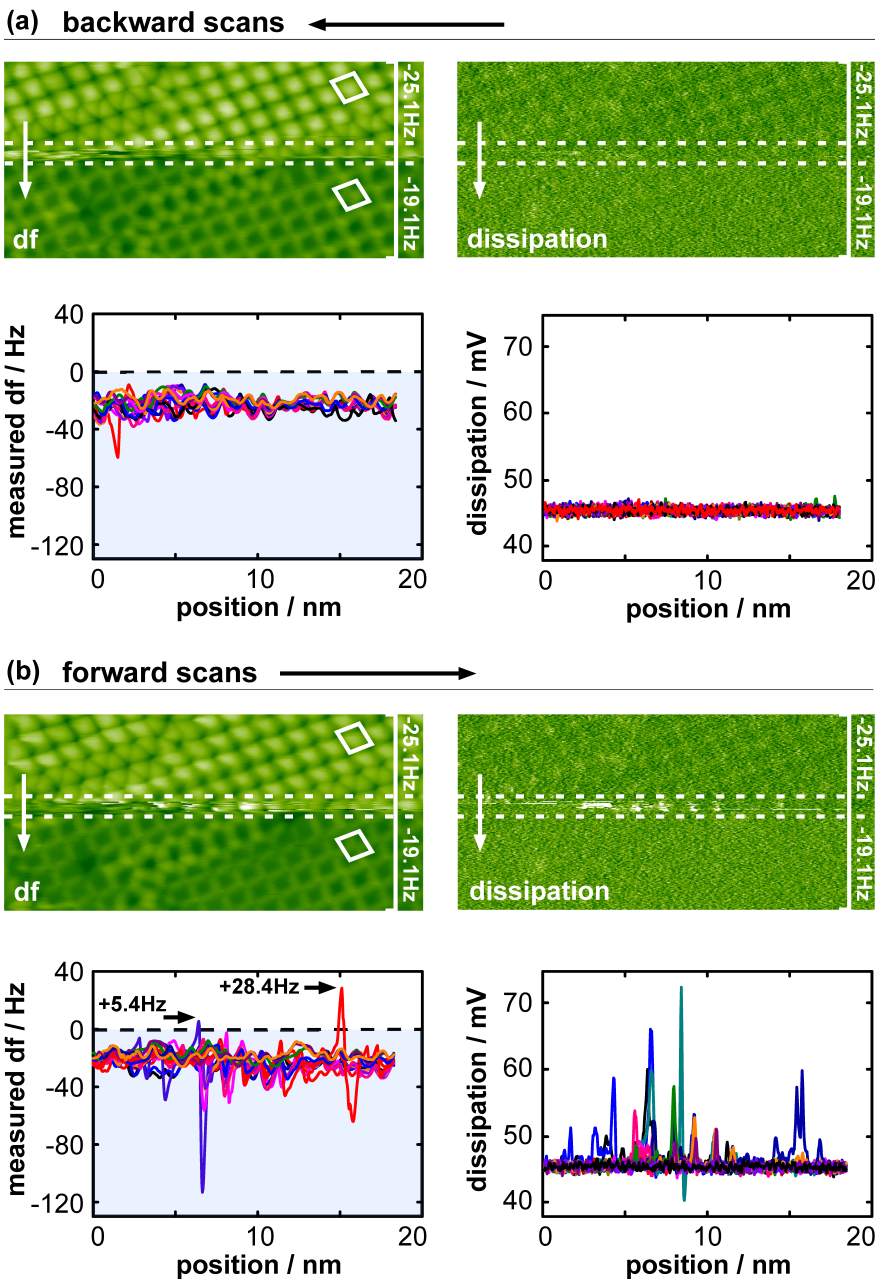

Figure 7.13: Backward (a) and forward scan (b), both with frequency shift channel (left panel) and dissipation channel (right panel). In the upper part of the NC-AFM images, the frequency shift setpoint was set to -25.1 Hz as indicated in the images. After the manipulation happened in the area enclosed by dotted lines, the frequency shift was set to -19.1 Hz for stable imaging. Below each NC-AFM image the linescans of the dotted area are plotted. Analyzing the area where manipulation was achieved reveals two line scans of the frequency shift channel in the forward scan with a positive frequency shift, which is related to a repulsive interaction between tip and molecules.

in Fig. 7.13.

The linescans in the backward scan of the frequency shift channel do not reaveal any remarkable deviations from the expected corrugation. Also the dissipation channel of the backward scan do not expose any indications for a manipulation process. However, two linescans in the forward scan of the frequency shift channel reveal significant positive frequency shifts, cor-

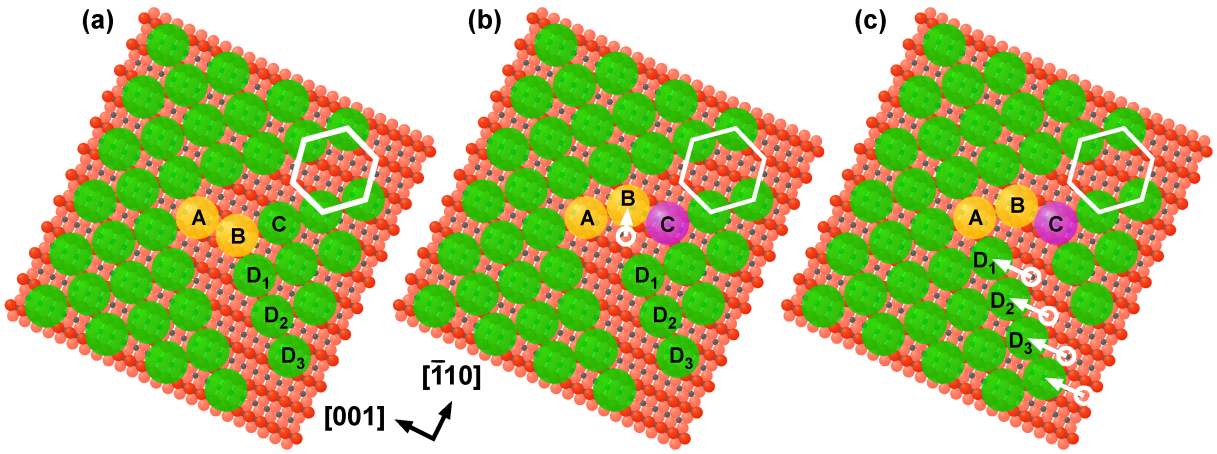

Figure 7.14: Model of the movement of a domain broundary with a C_{60} island. In (a) the situation before manipulation is shown. The molecules A and B are forming the stacking fault. From (a) to (b) the stacking fault molecule B was kicked over the bridging oxygen row to a new adsorption site, now forming a stacking fault with molecule C. After the movement of the stacking fault, the whole domain boundary moves successively, as sketched in (c). The molecules D_n move along the substrate troughs from the lower part of the island to its upper part.

responding to a repulsive interaction between tip and molecules.[13] This can be related to the observed manipulation process. Also the dissipation channel doubles its value in some linescans, indicating a strong energy dissipation at the manipulation process.

The situation after the manipulation (Fig. 7.12(b)) was recorded at the same frequency shift setpoint as the first image before manipulation (Fig. 7.12(a)). Comparing both images, an almost quadratic hole was created by removal of twelve C_{60} molecules from the plain island and five molecules from the upper domain boundary. In addition, a reordering of the lower left domain boundary was induced. This boundary moved one repeat distance closer to the encircled vacancy in the molecular island (indicated by three/two white circles between the domain boundaries). As the domain boundaries originate from stacking faults, the observed reordering must be caused by a movement of the associated stacking fault during the manipulation process. In Fig. 7.12(c) and (d) the situation before and after the movement of the domain boundary are sketched. The movement of the domain boundary is modeled in more detail in Fig. 7.14(a)-(c). From situation (a) to (b) the molecule B is moved across a bridging oxygen row, thus forming a new stacking fault with molecule C. This movement is assumed to be tip induced since breaking the stacking fault and moving the molecule over the bridging oxygen row is suspected to require additional energy. In the next step, the molecules D_n diffuse along the substrate troughs from one part of the island to the other, indicated by arrows in (c). Thus, (c) resembles the situation after manipulation as sketched in Fig. 7.12(d).

Comparing Fig. 7.14(b) and (c), it is evident that all molecules D_n are three-fold coordinated in the C_{60} layer in (c). In (b) the molecule D_1 directly at the stacking fault is only two-fold coordinated. Therefore, a maximization of coordination is thought to be the driving force for the

movement of the molecules D_n to the upper part of the island. This process is more likely thermally activated than tip induced, since the domain boundary moves along its whole length (Fig. 7.12(a) and (b)) and not only in the area, where the increased tip sample interaction occurs (Fig. 7.13).

The reordering of this domain boundary is accompanied by a rather large mass transport, as $1 + 2 \times n$ molecules need to change position in order to shift the whole boundary, with n being the number of C_{60} molecules in length on the domain boundary. Additionally, one C_{60} molecule needs to be removed, otherwise the boundary cannot moved.

The above presented manipulation process is reprocible as demonstrated in Fig. 7.15. Image (a) shows a well-ordered island with straight outer edges and some domain boundaries running along the island surface. Now, the tip-sample interaction was increased in the upper part of this islands, by scanning with increased frequency setpoints. As a result, a hole was induced in this part of the island. The procedure was reproduced in (c) in the lower part of the C_{60} island. It is assumed that the removed molecules from the holes attach to the right island edge. Fig. 7.15(d) proves that only the island of interest (encircled) was modified and all surrounding islands keep faultless in perfect order. Thus, holes can easily be induced in well-ordered C_{60} islands, without degrading the imaging tip.

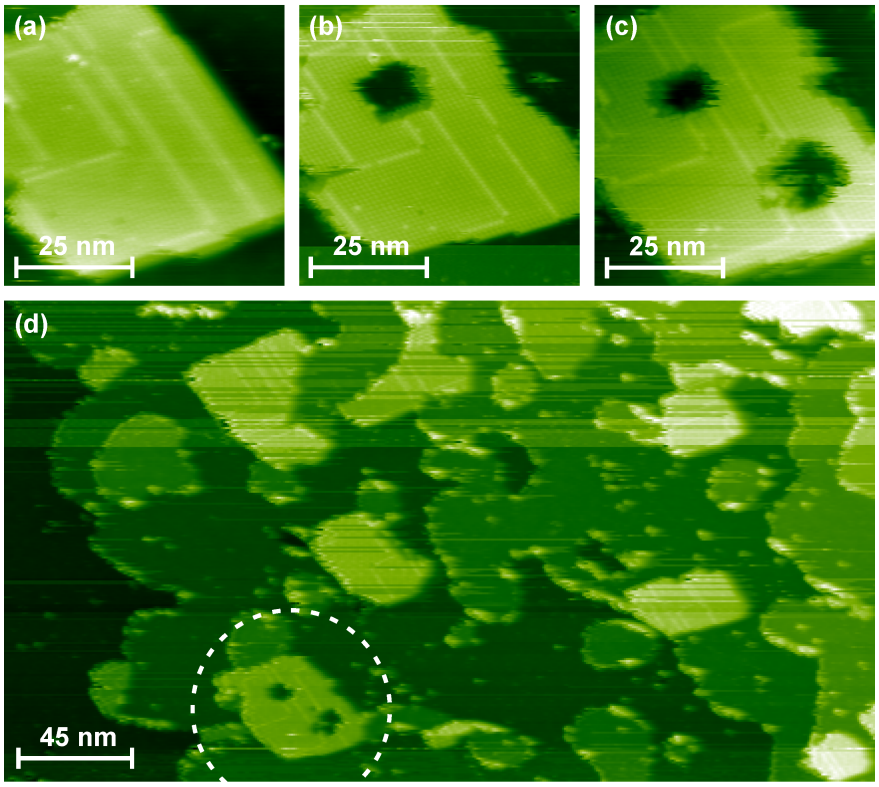

Figure 7.15: NC-AFM images (topography) of a C_{60} island and its surroundings. In (a) the island is in perfect order with straight outer edges and some domain boundaries running along the island surface. (b): Upon an increased tip-sample interaction, a hole was induced in the upper part of the island. Reproducibility is proven in (c). A further hole was created in the lower part of the island. In image (d) the modified island is shown with its surrounding islands. It is evident that only the island of interest was modified. All surrounding islands keep their perfect order.

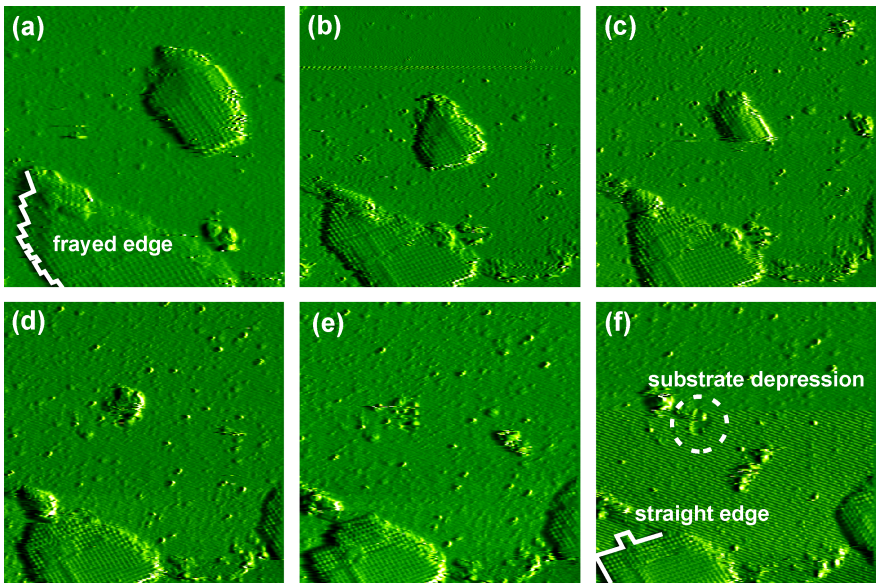

Figure 7.16: Series of NC-AFM images at almost the same frequency shift set-point (13.0 Hz to 15.0 Hz), 62 nm x 62 nm, frequency shift channel, backward scans. The first image is taken approximately 100 min after molecule deposition. All following images are taken successively with a time per frame of 9 min 20 s. The isolated island in the upper part of the image shrinks in size during scanning until it completely vanishes. In image (k) a substrate depression is observed, which is assumed to represent the nucleation seed for the island growth.

Removal of C_{60} islands

In Fig. 7.16(a), a C_{60} island of ~25 nm in length and ~14 nm in width is scanned. In Fig. 7.16(a)-(f) this island shrinks in size when scanning at frequency shift setpoints between -13.0 Hz and -15.0 Hz. In Fig. 7.16(c) the area has reduced to about one fourth of the initial size in Fig. 7.16(a). Fig. 7.16(a) suggests that the island has grown on the bare terrace, however, as can be seen in Fig. 7.16(f), a defect in the underlying substrate surface is observed. This defect might represent an anchoring site for the island, in agreement with the previous assumption that C_{60} molecules require nucleation seeds such as substrate step edges or other surface defects for island growth at room temperature. Additionally, the island in the lower left corner, which is attached to a substrate step edge, changed in shape while scanning. Interestingly, upon reshaping, the islands tend to form straight step edges. When comparing the shape of this island in Fig. 7.16(a) with (f) the initially frayed edges become straight. This indicates that straight edges are more stable than kinked edges, which can be explained by the increased coordination number of the C_{60} molecules forming the edges. For a straight edge, an edge C_{60} molecule has three neighbors while more corrugated edges would result in a smaller coordination number. The C_{60} molecules that have detached from the island are observed to move to nearby step edges or C_{60} islands in the vicinity. Moreover, they might be anchored to surface defects, which could explain the increase in single bright protrusions seen in this image series.

No significant manipulation events could be identified here. In particular, positive frequency shift values were not observed. Thus, despite the fact

that clear tip-induced repulsive manipulation processes exist as demonstrated in Fig. 7.13, the mechanism of manipulation in Fig. 7.16 is not as clear.

Conclusion

In summary, almost quadratic pits were created in ordered C_{60} islands using NC-AFM at room temperature. Upon gradually approaching the tip towards the surface, the interaction strength of the NC-AFM tip with the C_{60} molecules can be increased until manipulation is induced. Analyzing the frequency shift curves during manipulation allows for determining the manipulation mode and unambiguously assigning the observed manipulation to repulsive tip-sample interaction. Retracting the tip after manipulation allows for reproducible imaging and evaluating the manipulation result. Besides hole formation, the movement of a domain boundary by one repeat distance was observed. This movement is associated with the manipulation of a stacking fault and a rather large mass transport. Additionally, we observed reshaping and removal of islands. For the latter manipulation the detailed mechanism is not clarified yet.

8 C_{60} molecules on the CaF_2 (111) surface

Contents

To control the growth process for successfully employing self-assembly techniques in device fabrication, a detailed knowledge of both, intermolecular as well as molecule-substrate interactions is required.[9,39] Therefore, in this section, a prototypical molecule-insulator system, which is represented by C_{60} on the atomically flat CaF_2 (111) surface is selected to analyze and quantify the molecular diffusion and island formation in a wide temperature regime.

In the first part (Sec. 8.1), the parameters of diffusion, which are the diffusion barrier and attempt frequency, are determined employing the onset method (see Sec. 4.3). Using this method, the diffusion barrier has been determined for a few molecular systems on metallic and semiconducting surfaces.[59,60] On insulating surfaces, however, quantitative analysis of molecular diffusion has been performed very rarely so far,[61–65] revealing diffusion barriers ranging from 100 to 400 meV.[61–63] The latter experiments were, however, not accomplished under UHV conditions in all steps. Such experimental conditions result in an increased surface contamination and may, therefore, alter molecular diffusion and influence the

island density and island size distribution.[28] Therefore, the work was performed under UHV conditions, revealing quantitative results that were not affected by surface contaminants.

In the second part (Sec. 8.2), island structures are analyzed in more detail. Different C_{60} island structures emerged depending on the substrate temperature in a narrow regime around room temperature. Basically, peculiar hexagonal branched islands and triangular compact islands emerge. The observed island structures are explained by a thermally activated dewetting process of molecules hopping from the surface onto first layer islands. It was possible to monitor the dewetting process during island evolution in time-resolved imaging. Attention is especially paid to the hexagonal branched island structures. The formation of these peculiar islands on the CaF_2 (111) surface is attributed to the special order and spreading of the energies related to the molecular processes on the surface (see Sec. 4).

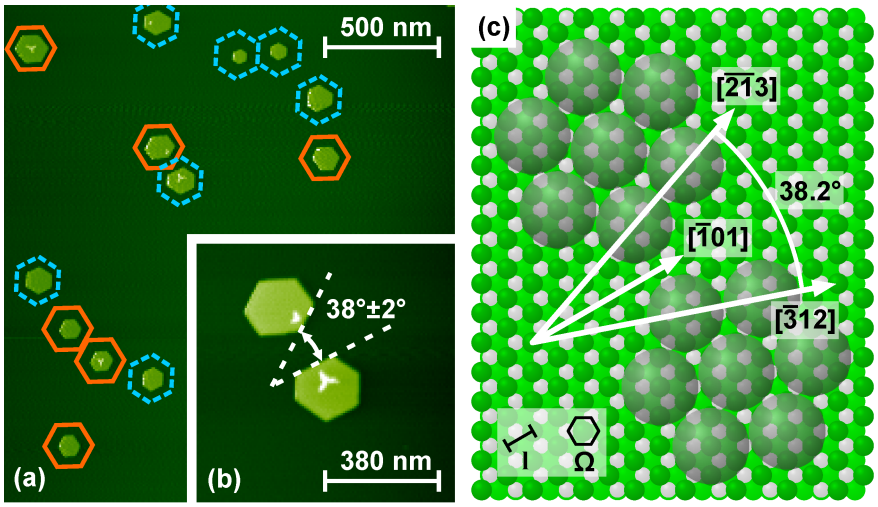

Figure 8.1: In (a) and (b) NC-AFM images (topography) are shown, prepared at a substrate temperature T_S = 169 K with subsequent quenching to 92 K. Clearly, two domains are observed. These domains are rotated with respect to each other by an angle of 38°±2°, in good agreement with the value determined in Ref. 165. (c) Model for the two different island types as previously suggested by Fölsch et al. using reflection high-energy electron diffraction.[165,166] The C_{60} molecules arrange in a hexagonal configuration, with a nearest-neighbor distance close to that of a bulk C_{60} crystal. Two different domains exist with close-packed C_{60} directions parallel to the CaF_2 [2̄13] and [3̄12] direction, respectively. The angle between both domains amounts to 38.2°. Note that the exact adsorption sites remain unknown and that arbitrary positions are chosen in the sketch.

8.1 Growth of C_{60} islands at low temperatures

Directly after the preparation of the bare CaF_2 (111) surface (see Sec. 5.2), the sample was cooled down to a defined substrate temperature between T_S = 96 K and T_S = 217 K by a liquid nitrogen flow cryostat thermally coupled to the sample holder. The temperature was adjusted and stabilized by regulating the liquid nitrogen flow through the cooling plate beneath the sample. Once the desired temperature was stabilized ($\approx$ 0.5 h), the C_{60} molecules were deposited with a deposition rate (flux) of $F = 5 \times 10^{-4}\,\mathrm{s^{-1}nm^{-2}}$ (see Sec. 6.1).

After C_{60} deposition, the sample was quenched to 92 K and transferred into the AFM situated in the same UHV system. Measurements were performed with the RHK 750 variable temperature force microscope under UHV conditions (see Sec. 3). Results shown in Fig. 8.1, however, were obtained with the Omicron VT-AFM 25 system. To minimize long-range electrostatic interactions, an appropriate bias voltage not exceeding ±10 V was applied to the tip. The temperature on the cleaved sample surface differs from the one measured at the cooling plate beneath the sample. Because the temperatures directly on the surface are of interest, the surface temperature was calibrated once with a type K thermocouple directly glued onto the sample surface. An error of ΔT_S = ±5 K for the temperature measurement is assumed.

Adsorption geometry

An overview image of the C_{60} island formation on CaF_2 (111) prepared at a substrate temperature of T_S = 169 K is shown in Fig. 8.1(a). As can clearly be seen, all islands exhibit an overall hexagonal shape. A closer

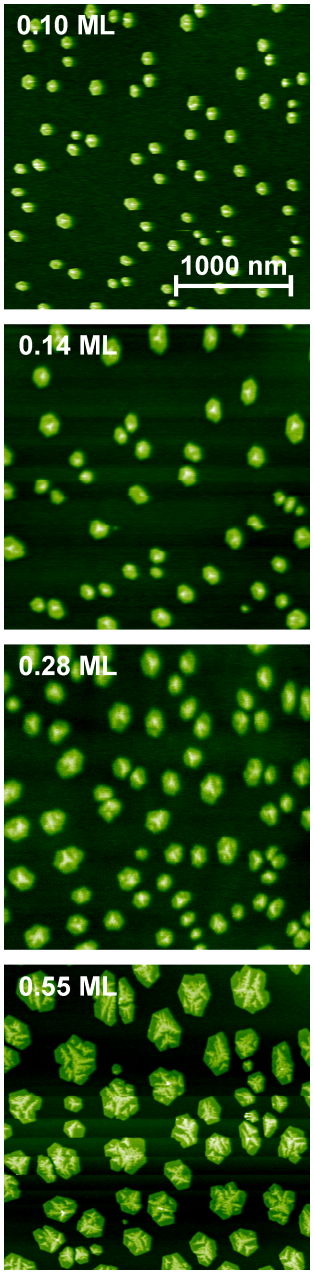

Figure 8.2: Overview images of C_{60} island on CaF_2 (111) prepared with coverages ranging from 0.10 ML to 0.55 ML at a substrate temperature of T_S = 217 K. On the islands second layer nuclei are evident.

inspection of the orientation of the islands with respect to the substrate reveals a grouping of islands into two different domains as illustrated in Fig. 8.1(a) by solid red and dashed blue hexagons, respectively. The sides of islands from different domains enclose an angle of 38°±2°, as shown in Fig. 8.1(b). In Fig. 8.1(c) a structural model for the possible arrangement of C_{60} molecules on the atomic lattice is presented that would result in an angle of 38.2° between the two domains. This model is in perfect agreement with previously presented results from Fölsch et al. who have studied the adsorption of C_{60} on the CaF_2 (111) by means of reflection high-energy electron diffraction.[165,166]

Assuming single jumps of molecules between the adsorption sites defined by this model, a single jump length of l = 386 pm (distance between two adsorption sites) is defined. The area of an adsorption site that is a hexagonal unit allowing for an area-filling coverage of the surface without overlap amounts to $\Omega = \sqrt{3}\,/\,2l^2 = 1.29 \cdot 10^5$ pm^2 (a single adsorbed C_{60} molecule covers about six adsorption sites). Jump length and adsorption site area are marked in Fig. 8.1(c).

When preparing islands at substrate temperatures larger than 220 K, C_{60} molecules appear to nucleate in the second layer, however, this will not be discussed here but in the following section. The second layer occupation does arise from direct impinging molecules as well as from molecules dewetting from the surface to the second layer.[46] To facilitate an unambiguous island size distribution analysis, care was taken to restrict this experiment to single-layer islands. Overview images from samples prepared with different coverages at a substrate temperature T_S = 217 K are shown in Fig. 8.2. The second layer's coverage is seen as tiny bright structures on top of islands. All of the different coverages exhibit a second layer nucleus. The first and second layer's coverage is compared with the total coverage in Fig. 8.3(a). It is evident that the percentage of the second layer nucleus rises with increasing coverage. Thus, the present study is limited to substrate temperatures $T_S \leq 220$ K and coverages $\theta \leq 0.28$ ML. In this regime, the islands exhibit only very few C_{60} molecules in the second layer. A detailed image of a second layer nucleus can be seen in Fig. 8.1(b). At the highest temperature used here (217 K) the second layer occupation is 5 % at 0.1 ML and rises to 14 % for 0.28 ML. At all lower temperatures, the second layer occupation is smaller than 5 % at a coverage of 0.1 ML.

Determining the critical island size

To obtain the critical island size from experiments, the island size distribution n_a is analyzed for different coverages at a fixed temperature and compared to the theoretical island size distributions for different i^* like described in Sec. 4.4.

This was accomplished in a series of molecular adsorption experiments

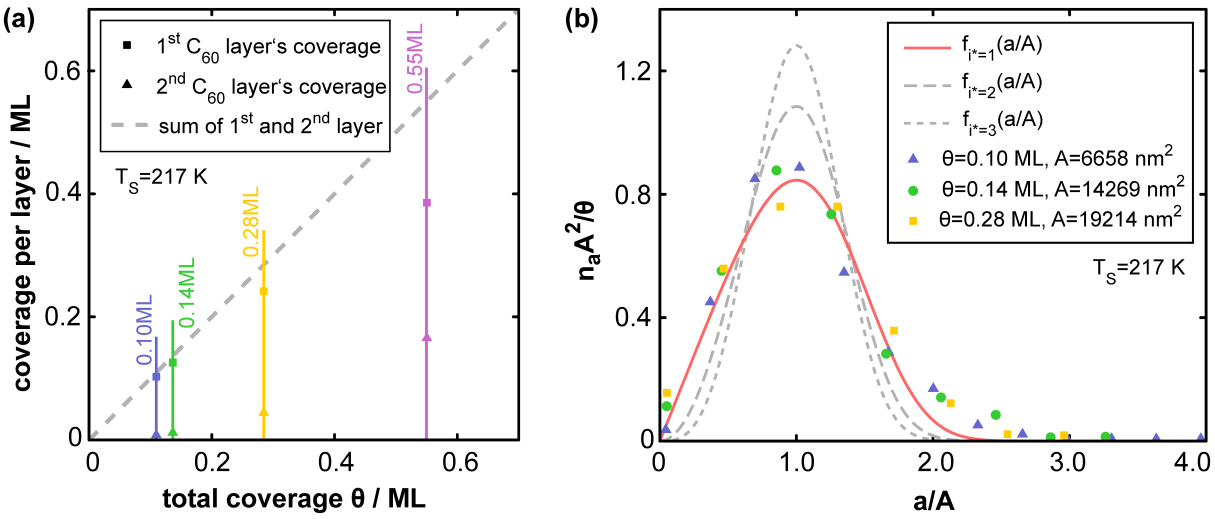

with coverages ranging from θ = 0.10 ML to θ = 0.28 ML performed at a substrate temperature of T_S = 217 K. Samples were quenched to 92 K for NC-AFM measurements. Island sizes were determined from topography images, using the threshold marking functionality from Gwyddion. Artifacts were manually removed before exporting the island size distributions. The island sizes may be shifted due to thermal drift, the size of the tip apex and feedback settings. These issues will be discussed in the following. To estimate the maximum error of drift effects, a rather large lateral drift of 0.1 nm/s for the slow scanning direction is assumed. Thus, for typical scanning parameters (frame size 3000 nm × 3000 nm and time 1000 s per frame) the relative error is about 3 %.[167] For the error arising from the size of the imaging tip, a typical tip size of 10 nm is assumed. This yields a relative error of 0.4 % at a frame size of 3000 nm × 3000 nm. Thus, the size of the tip is negligible for the analysis of large frames. Moreover, feedback settings may affect the apparent island size, e.g. with slow feedback settings the islands get elongated on the rear site along the fast scanning direction. In these cases, a comparison of the forward and backward scan clarified the outer shape of the island.

The data of the scaled island size distribution $n_a A^2 / \theta$ plotted against the normalized island size a / A for three different coverages is shown in Fig. 8.3(b). As expected, the scaled data points lie on one smooth curve except for the deviations due to experimental errors. Scaling functions $f_{i^*}(a / A)$ were calculated for $i^* = 1, 2, 3$ according to Eqn. 4.29. Clearly, the experimental data is best described by the model curve for $i^* = 1$ at T_S = 217 K. In other words, dimers and all larger clusters are stable at 217 K and are not assumed to decay.

Figure 8.3: (a) First and second layer's coverages in comparision to total coverages ranging from 0.10 ML to 0.55 ML. The percentage of the second layer is growing with increasing coverage. (b) Histogram of the island size distribution for different coverages θ. (Note that each data point represents an interval of island sizes, which is 2174 nm^2, 5731 nm^2 and 7984 nm^2 for the triangles, circles and squares, respectively.) Upon molecule deposition, the sample temperature was held at T_S = 217 K. For measurements, the sample was quenched to 92 K. The maximum relative error is ±8% for the abscissa and ±12% for the ordinate. The error mainly originates from thermal drift issues. Comparison with scaling functions $f_{i^*}(a / A)$ for different i^* gives strong evidence for a critical island size of $i^* = 1$.

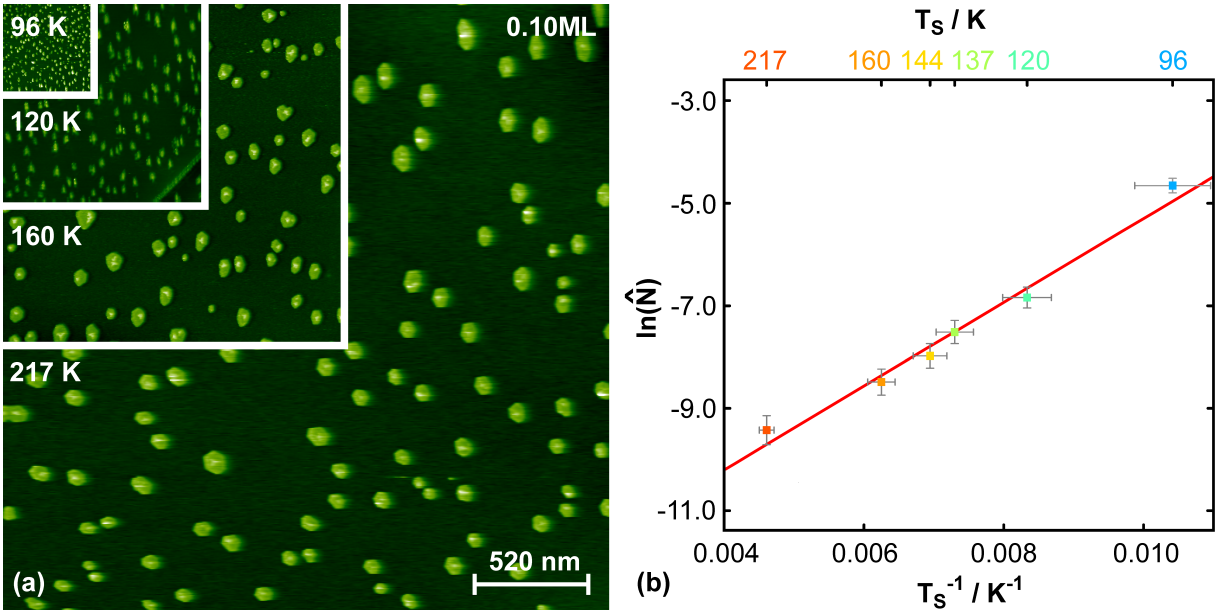

Figure 8.4: (a) NC-AFM images (topography) at a coverage of θ = 0.10 ML at different substrate temperatures between 96 K and 217 K. With decreasing temperature, the island density increases. Islands are one monolayer high, with an insignificant second layer nucleus (see main text). The scale bare applies to all images. (b) Upon decreasing substrate temperature T_S the island density $\hat{N}$ increases and is assumed to follow Eqn. 4.25. The slope reveals the diffusion barrier to E_d = (214 ± 16) meV.

Determining the diffusion barrier and attempt frequency

Using the critical island size from the previous experiment, the diffusion barrier E_d and the attempt frequency ν_0 can now be determined exploiting the dependence of the island density on temperature (see Sec. 4.3). This has been accomplished by procedures described in the following.

The sample was prepared with a fixed molecular coverage of θ = 0.10 ML at temperatures T_S between 96 K and 217 K and quenched to 92 K for NC-AFM measurements. Representative images obtained at several substrate temperatures are compiled in Fig. 8.4(a). At each temperature T_S, the island density per adsorption site $\hat{N}$ was determined from the images. A total of 1300 islands accounts for the statistics. For each temperature, an error of $\Delta\hat{N}$ = 4% for the island densitiy is assumed. In Fig. 8.4(b), $\ln \hat{N}$ versus T_S^{-1} is plotted and it can be seen that the data points follow a linear dependence.

The critical island size i^* = 1 was determined at T_S = 217 K and can also be applied to lower temperatures. This is reasonable by the following two self-sufficient arguments. The critical island size was determined to be i^* = 1 for the highest temperature (T_S = 217 K). For lower temperatures, the critical island size is expected to get smaller. Because islands are evident even at the lowest temperature (T_S = 96 K), the critical island size cannot be smaller than one. Therefore, i^* = 1 can be assigned to the whole temperature regime between 96 K and 217 K. The other argument relies on the linear dependence of the data points in Fig. 8.4(b). If the critical island size would change, a kink would be expected in plotting $\ln \hat{N}$ versus

T_S^{-1} (see Eqn. 4.25). However, in Fig. 8.4(b) no distinct variations from a linear dependence are observed for lower temperatures. Therefore $i^* = 1$ determined at $T_S = 217$ K, can safely be assigned for island growth between 96 K and 217 K.

From the slope of the linear regression of the data, a diffusion barrier of $E_d = (214 \pm 16)$ meV is derived according to Eqn. 4.25. The attempt frequency $\nu_0 = 1.4 \cdot 10^{12\pm0.6}\,\mathrm{s}^{-1}$ is taken from the axis intercept according to Eqn. 4.26.

Conclusion

In summary, the diffusion of C_{60} molecules on the atomically flat CaF_2 (111) surface at various substrate temperatures was analyzed under the clean conditions of an ultra-high vacuum. At low temperatures, the coexistence of two domains, with a hexagonal island shape was observed. For the determination of the diffusion parameters island densities and island sizes were analyzed instead of observing single-molecule hopping events. The critical island size ($i^* = 1$) and the diffusion barrier ($E_d = (214 \pm 16)$ meV) was determined for this system.

The value for the diffusion barrier agrees well with the general picture of a weak molecule-substrate interaction in the case of insulating surfaces ($E_d \lesssim 400$ meV).[61–65] The obtained diffusion barrier is much lower than the diffusion barrier of C_{60} molecules on metal surfaces, e.g. 1400 meV on Pd(110).[35] Moreover, the attempt frequency $\nu_0 \approx 10^{12}\,\mathrm{s}^{-1}$ lies within the range of previously reported values for large molecules (10^{10} to $10^{14}\,\mathrm{s}^{-1}$).[34–36]

The knowledge of the diffusion barrier plays a major role in exploiting molecular arrangements at different temperatures. It is, for example, possible to tune the island density by varying the substrate temperature. Thereby, a specific density of uniformly shaped C_{60} clusters can be created, which is of great importance for future molecular electronics, e.g., for the use as nano-pads.[145]

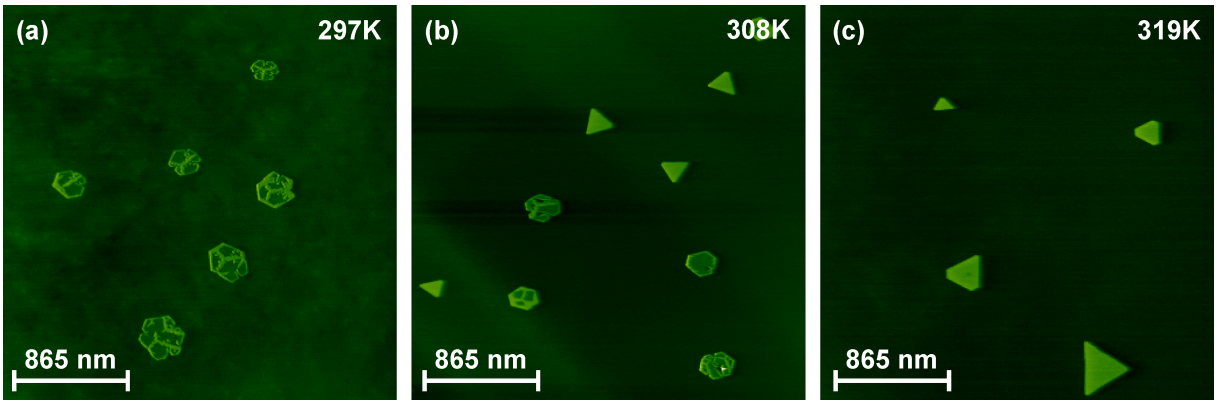

Figure 8.5: NC-AFM images (topography) of C_{60} molecules on the CaF_2 (111) at elevated temperatures. (a) At a substrate temperature T_S = 297 K branched islands emerge. Islands are one layer high but have a second-layer outer rim. The outer shape is hexagonal. (b) At T_S = 308 K branched and compact triangular two-layer high island coexist. (c) At T_S = 319 K only the triangular type of islands remains to exist.

8.2 Growth of C_{60} islands at and above room temperature

As described in Sec. 5.2, the CaF_2 (111) surface is heated after the cleavage procedure. After this heating interval the sample cools down to room temperature due to heat exchange with the surroundings. During this cooling process, C_{60} molecules were deposited for 2 min in different experiments with the sample temperature T_S at 319 K, 308 K and 297 K. At these temperatures the heat exchange is slow and the substrate temperature approximately falls with a rate of 0.2 K/min. Due to the slow heat exchange, the sample temperatures are assumed to be constant during the deposition interval of 2 min. Measurements took place when the sample was in thermal equilibrium with the surroundings ($T_S \approx 297$ K) and were performed with the RHK 750 variable temperature force microscope and the Omicron VT-AFM 25 system under UHV conditions (see Sec. 3).

Island shapes

Upon sublimating C_{60} molecules at substrate temperatures in the range of $297\,\text{K} \leq T_S \leq 319\,\text{K}$, island morphologies are different from the ones at low substrate temperatures.

Upon deposition at 297 K, the islands have an overall hexagonal outer shape (Fig. 8.5(a)). However, the inner structure is branched and the composition is complex. Two exemplary islands are shown in Fig. 8.6(a) and (b) with a corresponding line scan given in (d). These islands are one layer high but have second-layer outer rims, such that first-layer regions are enclosed by second-layer rims. Only very few first-layer regions without a second-layer rim were identified. In the following, this type of island is referred to as *T1*. This particular type of island has previously been observed on alkali halides.[46,111] Taking a closer look at *T1* islands, two subtypes can be distinguished. The first subtype *T1a* (Fig. 8.6(a)) does not exhibit a common

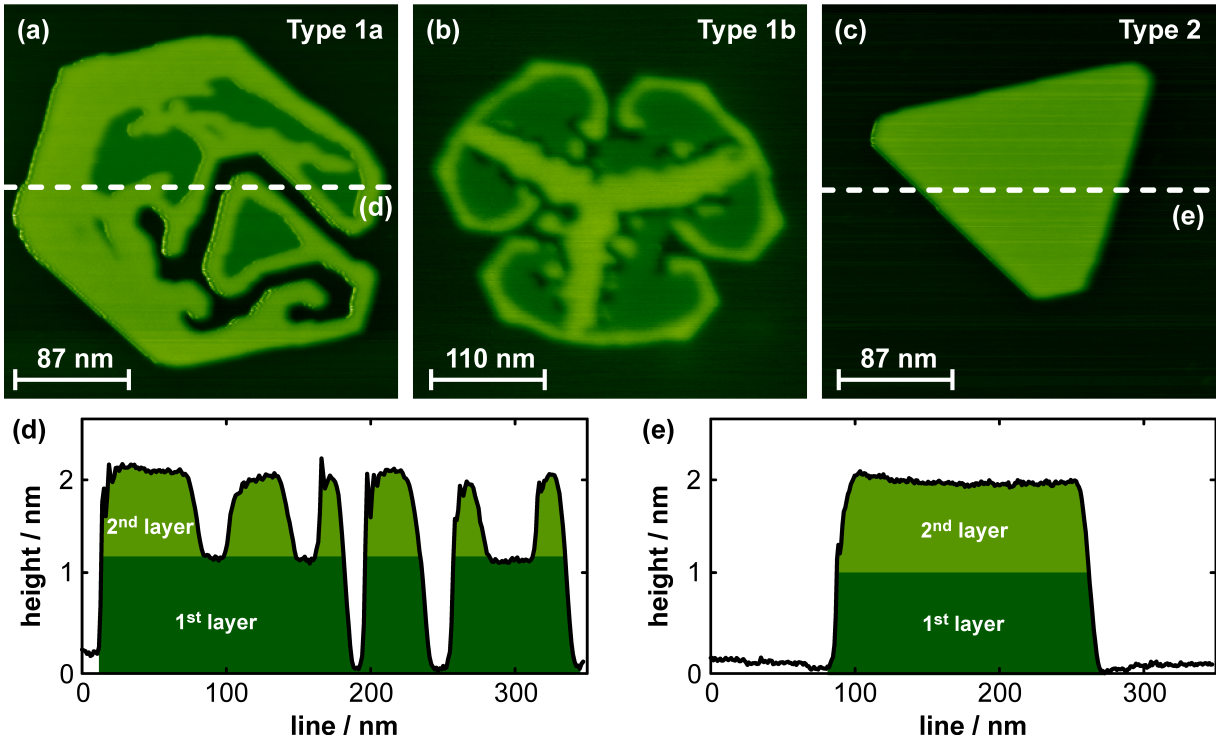

Figure 8.6: (a-c) NC-AFM images (topography) of C_{60} molecules on the CaF_2 (111) at elevated temperatures. (a) Hexagonal branched *T1a* island. (b) Hexagonal branched *T1b* island. (c) Triangular compact *T2* island. (d) and (e) are line scans from (b) and (c), respectively. The positions, where the line scans were taken, are indicated in (b) and (c), respectively

inner framework, whereas the second subtype *T1b* (Fig. 8.6(b)) exhibits a second-layer structure consisting of three branches in the middle of the islands.

Upon deposition at 319 K, islands are compact with a triangular shape (Fig. 8.5(c)). An exemplary island is shown in Fig. 8.6(c) with a corresponding line scan in (e). The triangular islands always consist of two complete C_{60} layers. This is evident even at very low coverages. At higher coverages, the third and every higher layer is growing in a dentritic manner on top of the underlying C_{60} layers. In the following, this type of island is referred to as *T2*.

Between 297 K and 319 K, a regime exists, where both distinct types of islands *T1* and *T2* coexist. At 308 K, e.g., the fractions of both types are approximately equal as can be seen in Fig. 8.5(b).

Evolution of the island growth

In the following, these different structures will be analyzed in more detail and the formation of the distinct types of islands will be described qualitatively. The model of island formation was developed in close collaboration with and (Universität Osnabrück).

As seen before (Fig. 8.1), the first C_{60} layer is growing with a perfect

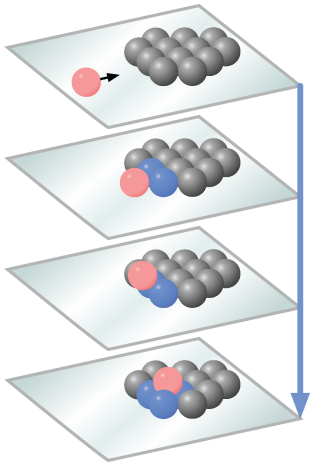

Figure 8.7: Dewetting process. A freely diffusing molecule attaches to two first-layer molecules and can dewet to the second layer, where it is attached to three molecules. During dewetting, the molecule is always attached to two molecules and has only to detach from the surface.

hexagonal shape at low temperatures. This was ascribed to the isotropic diffusion on the surface and the intermolecular interactions, which favor the hexagonal arrangement of the C_{60} molecules as in the bulk structure. At elevated temperatures (297 K $\leq T_S \leq$ 319 K), which are discussed now, the diffusivity on the surface is enhanced, thus, it is expected that the first layer again forms islands with a hexagonal arrangement like in the bulk structure.

However, elevated temperatures allow for a new process to be observed, resulting in qualitatively new island shapes. A thermally activated dewetting process favors C_{60} molecules attached at the outer edges of an island to jump to the second layer. This dewetting process is favored by the relatively weak molecule-substrate interaction compared to the intermolecular interaction. The dewetting process is responsible for the second-layer outer rims of *T1* islands and the completed second layers of *T2* islands. At low temperatures, the dewetting process is hindered. This can be concluded from the rather low second-layer occupation at temperatures $T_S \leq$ 217 K (see previous section). Thus, the dewetting process becomes significant in the temperature regime between 217 K and 297 K.

In Fig. 8.7, the dewetting process is sketched. Initially, molecules attached to an island edge are in-plane coordinated to two molecules of the first layer. Additionally they are bonded to the surface. However, such molecules can gain a higher coordination by dewetting to the second layer. Molecules in the second layer are coordinated to three underlying first-layer C_{60} molecules. For dewetting, molecules only have to detach from the surface, but keep coordinated to the initial two C_{60} molecules. Once molecules have dewetted, they can diffuse on the second layer. If diffusion in the second layer is slow, molecules will stay for a while at the island's border where they have dewetted. Such molecules promote the dewetting of further molecules: freely diffusing molecules on the substrate surface have an additional appeal to dewet, as they also gain an in-plane coordination in addition to the basic three-fold coordination to the underlying first layer.

Before, dewetting has been observed for various molecule species on different surfaces. On metal and semiconductor surfaces, molecular dewetting mainly results in compact islands.[168–173] Branched structures have not been observed on these surfaces. On many insulator surfaces molecular dewetting was observed.[46,108,111,135,174–178] However, branched structures similar to the ones presented within this section, have been appeared only for C_{60} molecules on the KBr(100) and NaCl(100) surface.[108,111] But no model has been presented yet, explaining the origin and evolution of these structures on a molecular level. This is accomplished here. In the following, a molecular model is proposed, explaining different paths of island evolution supported by temperature-dependent and time-resolved measurements.

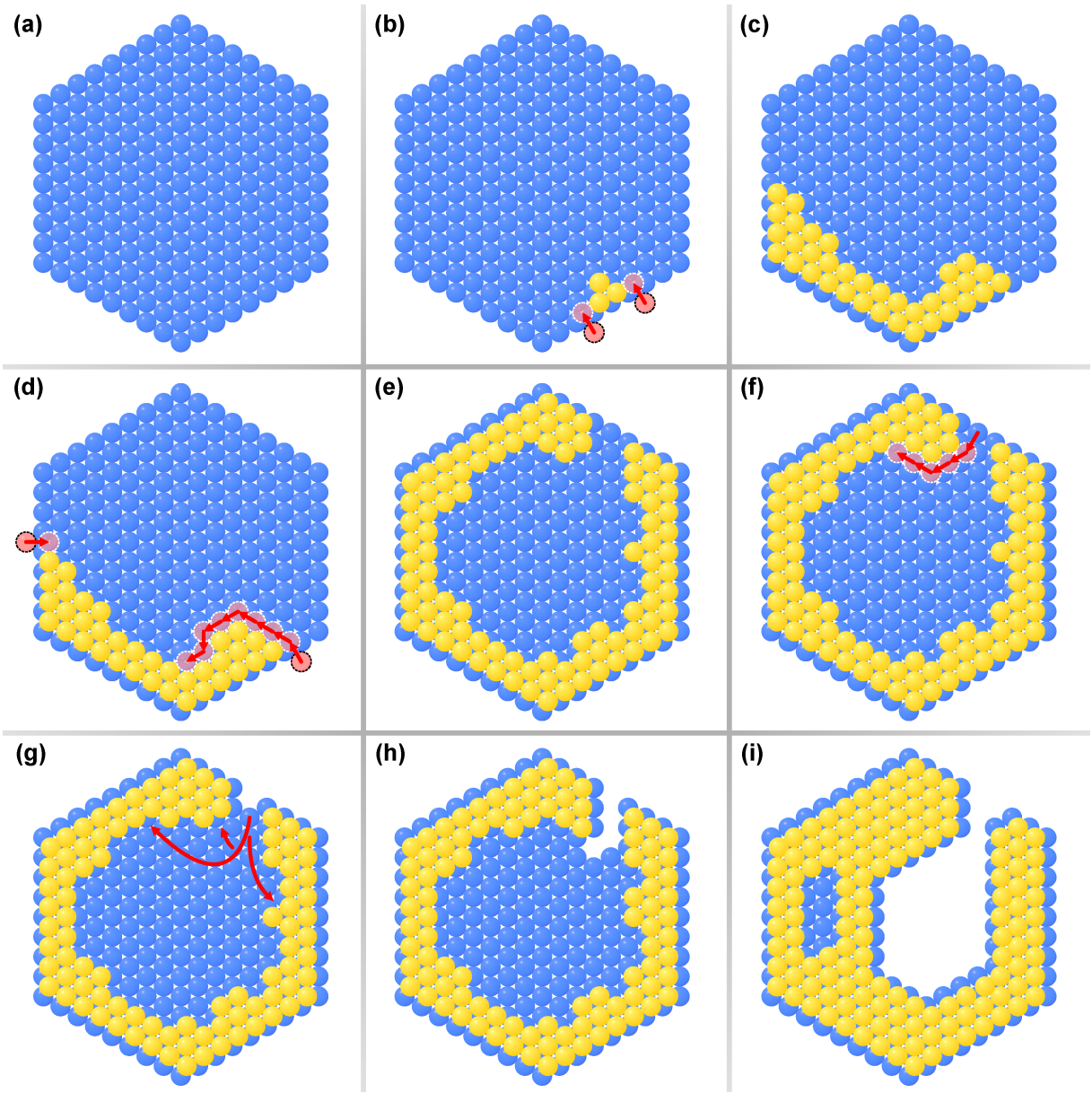

Figure 8.8: Model for the orgin of type *T1a* islands. A second-layer rim is growing around the hexagonal shaped first-layer island. When two rims approach, a cutout grows to the interior of the island.

For the evolution of a *T1a* islands, initially a hexagonal first layer exists. Assuming that the diffusion of single molecules on the surface and the formation of first-layer islands is faster than the dewetting process, in a first step, a hexagonal first layer grows (Fig. 8.8(a)). In a next step, due to rare dewetting processes or, very unlikely, due to direct deposition of molecules onto the first layer, a second-layer occupation at the border of the first-layer island can emerge (Fig. 8.8(b)). Nearby this nucleus, dewetting of diffusing molecules is promoted. Molecules dewetting at such a nuleus gain

a higher coordination than molecules dewetting without a second-layer nucleus nearby. Thus, molecules preferentially dewet to the two positions at both ends of the nucleus, likewise sketched in Fig. 8.8(b,d). Molecules, which have dewetted to these positions, are characterized by a three-fold coordination to the underlying first layer and (at least) one additional coordination to a second-layer's molecule. In this way, the nucleus grows like a wall around the island (Fig. 8.8(e)). Molecules, which dewetted to the second layer, can further diffuse and will not necessarily stay at the position where they have dewetted. Dewetted molecules will prefentially remain at the second-layer nucleus and diffuse along its border to keep a high coodrination rather than detaching from the nucleus. In this way, the dewetting positions can be used for more than one molecule to reach the second layer. Thus, the rim around the island does not consist of a single row of C_{60} molecules.

In principle, also molecules forming the straight edges of the island's first layer have the possibility to account to the second-layer occupation through dewetting. But, these molecules are four-fold coordinated and, therefore, dewetting is energetically much more unlikely than dewetting of freely diffusing molecules at the island's edges, which are only two-fold coordinated. In addition, the four-fold coodinated molecules have to detach from two of the four nearby molecules for dewetting. In contrast, freely diffusing molecules attached to two edge molecules do not need to detach from these molecules during detwetting, as explained before and sketched in Fig. 8.7. In consequence, the rims grow almost exclusively by dewetting of freely diffusing molecules. But, when the two rim terminations approach each other, the dewetting process changes in nature. The rims are not feed by freely diffusing molecules any more. Because dewetting of freely diffusing molecules becomes less likely, now, the much slower dewetting of molecules in the straight edges of the first layer is assumed to come forward (Fig. 8.8(f-i)). Thus, a cutout is formed extending the rim to the interior of the island. The growth process of this newly created rim is the same as described for the outer rim. In this way, inner first-layer regions get encapsulated by second-layer rims.

The sequence of NC-AFM images in Fig. 8.9, which was taken about 90 min after molecule deposition, supports the proposed mechanism for the evolution of *T1a* islands. In Fig. 8.9(a), a hexagonal island with a second-layer outer rim is shown, which is not yet closed. From Fig. 8.9(b) to (j), a cutout forms within 122 min. After the cutout has formed, the island was observed for further 96 min, but no further changes were recognized (Fig. 8.9(j-l)).

From this sequence of images, the speed of dewetting can be determined. Thereby, the evolution of a cutout can be quantified, which will be useful for a comparison with simulations. For this purpose, the evolution the

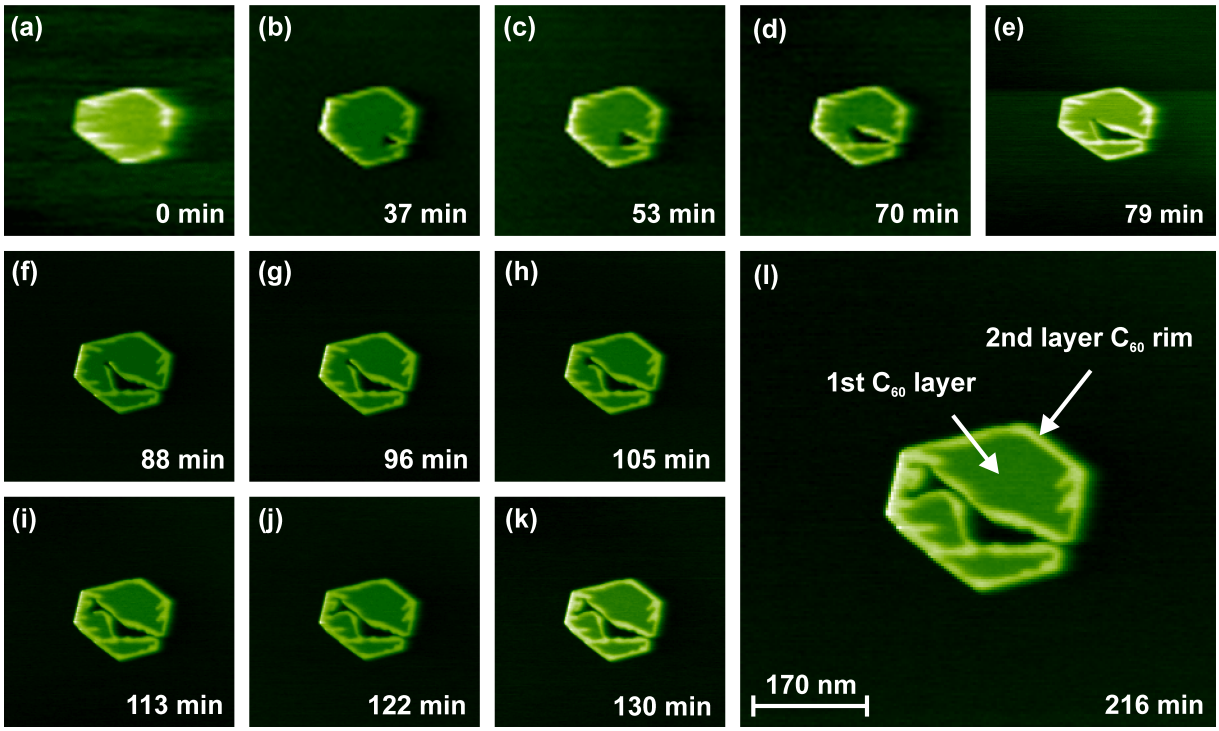

cutout's area is analyzed. Due to the fact that the molecules arrange in a close-packed structure, the area of the cutout can be converted to the number of dewetted molecules. Moreover, the perimeter of the cutout is measured and converted to the number of molecules along the cutout's perimeter. In Fig. 8.10, the time evolution of both, the number of dewetted molecules $N_a(t)$ and the number of molecules at the perimeter $N_p(t)$ is plotted. About 4500 molecules dewetted in total. From the ratio of $N_a(t)$ / $N_p(t)$ the average width of the second-layer's rim around the cutout can be estimated to be ten molecules. Analyzing the cutout's evolution within time, the development can be divided in two parts. First, a large main cutout is formed. From Fig. 8.10 it is apparent that the growth of the cutout is not linear, but accelerates. After 79 min the cutout is almost closed (Fig. 8.9(e)). However, the evolution of a further process emerge at which an appendix forms from 79 min to 122 min. A further evolution of the appendix with an accompanied acceleration of the dewetting process is hindered because the cutout reaches the outer rim of the island. For the appendix, about 700 molecules have dewetted within 43 min. This is similar to the initial speed of the main cutout, where about 650 molecules have dewetted within the first 37 min. Thus, both cutouts have formed with almost the same speed in the beginning.

Figure 8.9: Evolution of a cutout imaged with NC-AFM (topography). First, a second-layer rim is formed around the hexagonally shaped first layer. At the encounter of both ends of the rim, a cutout grows to the interior of the island. The molecules from the cutout dewet and form a rim around the cutout.

As noted before, the dewetting of the freely diffusing molecules, which

forms the outer rim, is assumed to be much faster than the dewetting of island's molecules forming the rim of the cutout. This is supported by the times scales in Fig. 8.9. The cutout with a perimeter of approximately 450 molecules has formed within 122 min, whereas the outer rim with a perimeter of 950 molecules has formed in less than 90 min. Both, the rim of the cutout and the outer rim have almost the same width of about 10 molecules. Therefore, the average speeds can be assigned to about 40 molecules per minute for the dewetting at the cutout and to approximately 100 molecules per minute for the dewetting forming the outer rim. This simple comparison indicates a larger speed of the evolution of the outer rim than the evolution of the cutout. It has to be emphasized that the 90 min for the forming of the outer rim of freely diffusing molecules is much overesimated. Freely diffusing molecules are assumed to decay rapidly after deposition. Thus, the outer rim must have formed in an about one order of magnitude smaller timescale.

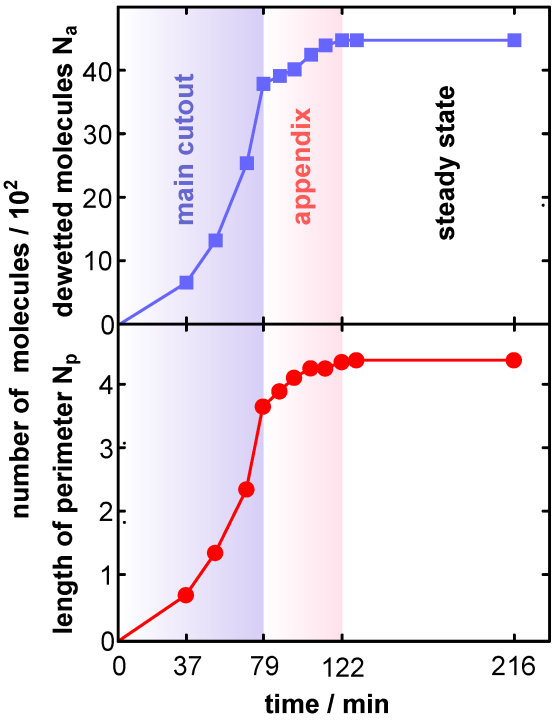

Figure 8.10: At the top, the total number of molecules that have dewetted form the cutout N_a is plotted against the time (data from Fig. 8.9). In total, about 4500 molecules have dewetted within 122 min. The process is not linear, but accelerates. The process can be divided in the forming of a main cutout and an additional appendix. At the bottom, the evolution of the perimeter N_p is shown.

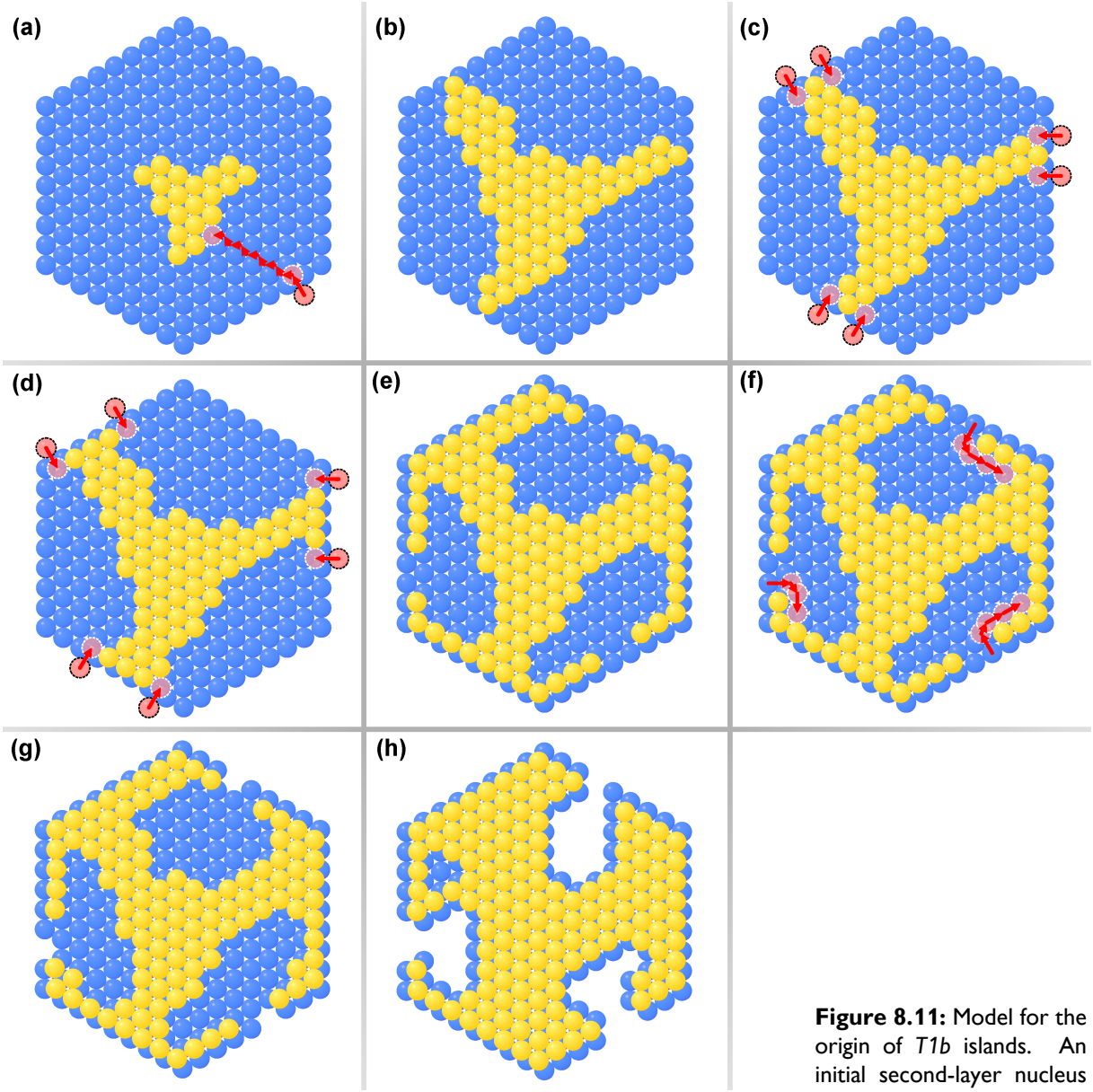

Figure 8.11: Model for the origin of *T1b* islands. An initial second-layer nucleus in the middle of a hexagonally shaped first-layer island grows until it reaches the border of the island. From the place, where a second-layer branch has reached a border, a second-layer rim is growing around the island. If two rims approach, a cutout grows to the interior of the island.

In contrast to *T1a* islands, *T1b* islands exhibit an initial second-layer nucleus in the middle of the island (Fig. 8.11(a)). This nucleus grows in each of its three directions by dewetting of diffusing first-layer molecules (Fig. 8.11(b)). At *T1b* islands, dewetted molecules are not detained at the border by other second-layer molecules. This is in contrast to the evolution of *T1a* islands, where dewetted molecules are hindered from free diffusion within the second layer by molecules at the borders of the island. But in comparison to *T1a* islands, the second-layer nucleus of *T1b* islands grows slower, because

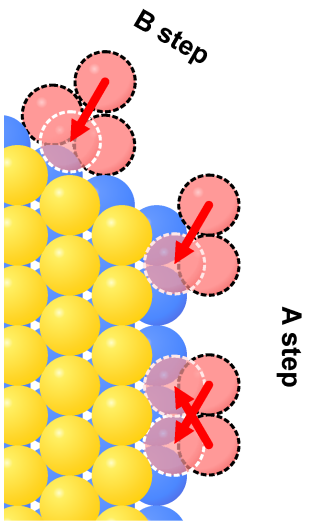

Figure 8.12: Dewetting at A and B edges and at corners. For dewetting at A edges two molecules have to encounter at an A edge. Thus, one of the molecules can jump over the other to attach to the second-layer nucleus. Like at A edges, two molecules also have to meet at the island's corners for dewetting. However, for dewetting at corners, the molecule, which dewets is only two-fold coordinated in the first layer. In contrast, at A edges the molecule, which dewets is coordinated to three molecules. Thus, dewetting at corners is more likely/faster than at A edges. In contrast, at B edges, three molecules have to meet in order for a dewetting event. Thus, this process is the slowest.

no second-layer molecules at the border promote the dewetting process.

Where a growing second-layer branch reaches the border of the island, the dewetting process is promoted (Fig. 8.11(c)). Thus, a second-layer rim is growing like for *T1a* islands, as sketched in Fig. 8.11(c-e). When two rims approach each other, a cutout is formed (Fig. 8.11(f-h)).

Islands of type *T2* are fundamentally different from *T1* islands. They have a triangular outer shape and always possess a complete second layer. In Fig. 8.13, the proposed mechanism for the evolution of this kind of islands is sketched. Prerequisite for the evolution of a *T2* island is a full second layer of a small nucleus (Fig. 8.13(a)) through dewetting or, very unlikely, through direct deposition in the second layer. For the further evolution, freely diffusing molecules are required. Freely diffusing molecules are most evident during the deposition regime. Shortly after deposition, almost all molecules are assumed to be involved in stable islands due to the small diffusion barrier on the surface. Because of the second layer's occupation, two different kinds of edges exist, A and B edges, as sketched in Fig. 8.12 and in Fig. 8.13(b) in more detail. At A edges the encounter of two molecules is required for a dewetting process. One of the molecules can jump over the other to attach to the second-layer nucleus. In contrast, dewetting at B edges requires three molecules to encounter. Thus, dewetting at B edges is less likely than at A edges. A special case are the island's corner positions. At corners two molecules have to encounter for a dewetting process, like at A edges. However, at corners molecules are only two-fold coordinated in the first layer before dewetting, whereas molecules are three-fold coordinated before dewetting at A edges. Thus, dewetting at corners is more favourable than dewetting at A edges and therefore the fastest of the three mentioned dewetting processes. In consequence, freely diffusing molecules arriving at islands edges most favorable dewet at the A edges and corners. Thus, considering the island's outer shape, islands are expanding faster perpendicular to A edges than perpendicular to B edges, which is pointed out in Fig. 8.13(c-f). In other words, B edges prolongate and A edges shrink. This yields a tapering of the B edges, resulting in the triangular outer shape (Fig. 8.13(f)). As a consequence, the island's shape is induced by the second layer. Note that A and B sites exist only for freely diffusing molecules dewetting at an island edge. On the second layer itself, no A or B sites exist.

As explained, *T2* islands establish through dewetting of freely diffusing molecules. Therefore its growth mainly takes place in the deposition regime. In contrast, the branched structures of *T1* islands do not need freely diffusing molecules, because the rims of the cutouts are fed with molecules from inner regions of the island. The evolution of the cutouts is rather slow, such it can mainly be assigned to be a post-deposition phenomenon. This is also evident from experiment (Fig. 8.9).

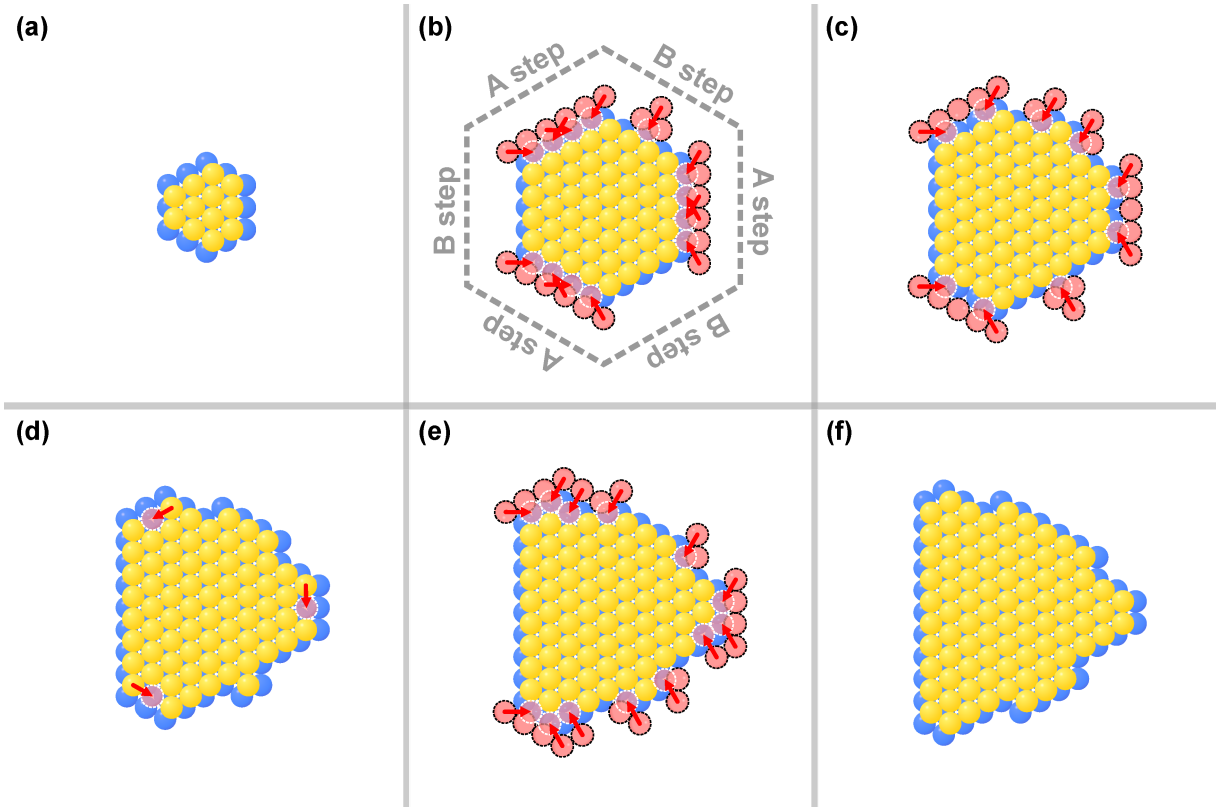

Figure 8.13: Model for the origin of *T2* islands. Due to an initial full second-layer nucleus, A and B edges occur. Dewetting at corners and A edges ist faster and more favorable than dewetting at B edges. Thus, B edges grow faster than A edges. Due to the tapering of the B edges, a triangular island is shaped.

From the model it is apparent that the evolution of *T2* islands requires a higher substrate temperature (at same deposition rate) compared to *T1* islands. A higher temperature favors the thermally activated dewetting process. For *T2* islands, dewetting has to be faster than the arrival of free diffusing molecules at the island edges to expose always the edges of the the second layer to newly attached first-layer molecules. However, if molecules would arrive faster than they can dewet, by means of a lower substrate temperature, the first layer would grow faster than the second layer. Thus, a large first layer would form with a smaller second-layer nucleus at the rim or in the middle of the island. This is exactly the initial state of *T1a* and *T1b* islands, respectively.

Thus, from the model, one would expect *T1* islands to be prevalent at lower temperature and *T2* islands to be prevalent at higher temperatures. Also a regime is expected, where both types of island coexist. This is in perfect agreement with experiment as demonstrated in Fig. 8.5.

In addition to the many experimental evidences supporting the proposed model of island evolution, ongoing Monte Carlo simulations (, Universität Osnabrück) support the picture given here. However, the simulation are not completed and will be presented elsewhere.

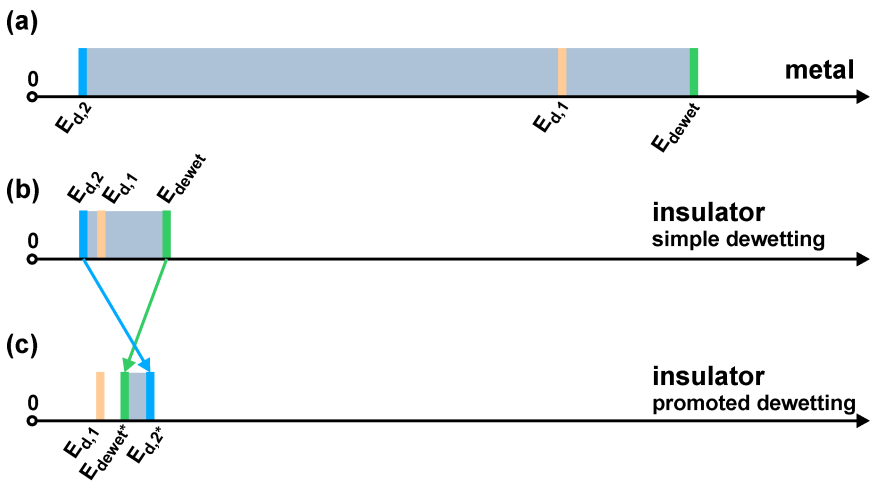

Figure 8.14: Order of energies at different circumstances as described in the main text and in Tab. 8.1

Island growth on metal and insulating surfaces

Comparing the diffusion and dewetting processes of a molecule on a metal surface with the same processes on an insulating surface, both systems basically differ in the diffusion barrier of the molecules on the surface $E_{d,1}$ and the dewetting barrier E_{dewet}. The barrier for diffusion in the second layer $E_{d,2}$ is very similar if not identical for both system, as it is mainly ruled by the intermolecular interactions. Assuming the temperature is chosen high enough to allow diffusion on the substrate (given by $E_{d,1}$), while still allowing stable first-layer islands to form, fundamentally different island shapes may arise due to these different energy barriers when comparing metal and insulating surfaces. This is sketched in Fig. 8.14 and explained in the following.

For a molecule-metal system (Fig. 8.14(a)), the molecule-substrate interaction is usually stronger than on an insulating surface. Therefore, both, the diffusion barrier on the substrate $E_{d,1}$ and the dewetting barrier E_{dewet} are larger on a metal surface compared to an insulating surface. By choosing a temperature activating diffusion ($E_{d,1}$) and first-layer formation on the substrate, the energy barrier for diffusion in the second layer is well overcome ($E_{d,2} < E_{d,1}$). Therefore, if dewetting occurs, the temperature will be sufficiently high for the molecules to easily migrate on the second layer away from the border where they have dewetted. Molecules will grow in a compact manner on top of the first layer. Thus, dewetting is possible, but no branched structures will arise.

In contrast, for a molecule-insulator system, like sketched in Fig. 8.14(b), the diffusion barrier on the substrate $E_{d,1}$ and the dewetting barrier E_{dewet} are strongly decreased due to a weaker molecule-substrate interaction. The barrier for diffusion in the second layer $E_{d,2}$ is the same as for the previously discussed molecule-metal systems. However, the vital difference is

Energy	Description
$E_{d,1}$	energy barrier for diffusion of molecules on the substrate
$E_{d,2}$	energy barrier for diffusion of free molecules in the second layer
$E_{d,2^*}$	energy barrier for diffusion of molecules along a second-layer nucleus
E_{dewet}	energy barrier for dewetting of molecules
E_{dewet^*}	energy barrier for dewetting of molecules, promoted by second layer molecules

Table 8.1: Descriptions of the energies sketched in Fig. 8.14

the much lower dewetting barrier E_{dewet} at the molecule-insulator system.

The dewetting barrier E_{dewet} and the barrier for diffusion on the second layer $E_{d,2}$ are in close vicinity so that both processes happen at about the same time scale. Thus, molecules which have dewetted have the chance to trigger more molecules to dewet before they have a chance to move away from the border to the interior of the island. Clusters of two or more molecules at the border are assumed to be stable and trigger more molecules to dewet.

In Fig. 8.14(c) the energetical situation is sketched, if a second layer nucleus has formed at the island border. The dewetting barrier E_{dewet^*} is lowered, as molecules can more easily dewet at both ends of the cluster and gain a higher coordination than dewetting without a second layer nucleus nearby. Molecules, which have dewetted will stay at the cluster and move along its edges. The diffusion barrier along these edges $E_{d,2^*}$ is larger than the barrier of free diffusion in the second layer $E_{d,2}$. In this way a rim is forming around the island and branched structures may arise, as described in detail before. Thus, the order of the dewetting barrier and the second-layer diffusion barrier has changed in comparison to the molecule-metal system in Fig. 8.14(a). This constitutes a new aspect for molecule-insulator systems in difference to molecule-metal systems. Due to the special energetic order for the presented molecule-insulator system, molecules will form a rim around the island and branched structures will arise, like evident for *T1* islands of C_{60} on the CaF_2 (111) surface.

Thus, as worked out from Fig. 8.14, branched structures are not expected on metal surfaces. The change in order of the dewetting energy and the barrier of second-layer diffusion represents the fundamental difference to a metal system and constitutes the origin of the observed branched structures on this insulator substrate surface.

Conclusion

For C_{60} molecules on the CaF_2 (111) surface, different island structures were observed depending of the substrate temperature during molecule deposition. In the studied temperature regime around room temperature, branched hexagonally shaped islands emerge at a temperature of 297 K, whereas deposition at higher substrate temperatures, e.g. 319 K, yields very compact stacked triangular islands. The path of island evolution is depicted qualitatively in agreement with temperature-dependent and time-resolved experimental observations. Dewetting is assumed to play a major role for the described island structures.

Thus, within this section, the processes for the evolution of unusually branched islands on a prototypical insulator surface were uncovered at the molecular level. Besides the expected quantitative differences (e.g. island sizes and island density) to molecule-metal systems, the molecular island formation presented here differs qualitatively from the ones usually observed on metal substrates. The qualitative difference is caused by the change in the order of the dewetting barrier and the barrier for second-layer diffusion. This allows for a second-layer induced dewetting, resulting in branched island structures.

This new and detailed insight into island formation on insulating surfaces may be exploited to further craft molecular nanostructures.

9 Coadsorption of C_{60} and SubPc molecules on the CaF_2 (111) surface

Contents

In the experiments described in the previous sections, the molecular diffusivity was changed as a strategy to tune the resulting assembly of molecules on surfaces. A directed self-assembly was accomplished by surface morphology (C_{60} on TiO_2 (110), Sec. 7) and temperature-dependent deposition (C_{60} on CaF_2 (111), Sec. 8). Now, the coadsorption with a second molecule is explored for tailoring the molecular assembly. Coadsorption of two or more molecule species has attracted great interest in recent years and was tested for a multitude of molecule-substrate combinations to create novel functional structures.[129,179–206] However, the coadsorption of C_{60} and SubPc molecules has only been tested on a metal surface, namely Ag(111).[129] For this system, different arrangements have been found, e.g., parallel-running straight, separated C_{60} rows decorated with SubPc molecule have been observed. Coadsorption has only been tested for simultaneous deposition at this system.

However, for the application of such coadsorbed structures, e.g., in molecular electronics, an insulating substrate surface is necessary. Thereto, within this section, the principles of coadsorption of C_{60} and SubPc molecules on an insulating surface, namely CaF_2 (111) are studied.

For each experiment, bare CaF_2 (111) surfaces were prepared according to Sec. 5.2. In a first step, the growth of pure SubPc islands is analyzed

shortly. Hereon, SubPc and C_{60} molecules were codeposited onto the surface. Two different paths of coadsorption were tested: sequential and simultaneous deposition. Measurements took place at room temperature and were performed with the RHK 750 variable temperature force microscope under UHV conditions (see Sec. 3). The present study revealed that the intermixing of both molecule species can be regulated by modifying the deposition order. Moreover, island structures were altered by thermal activation.

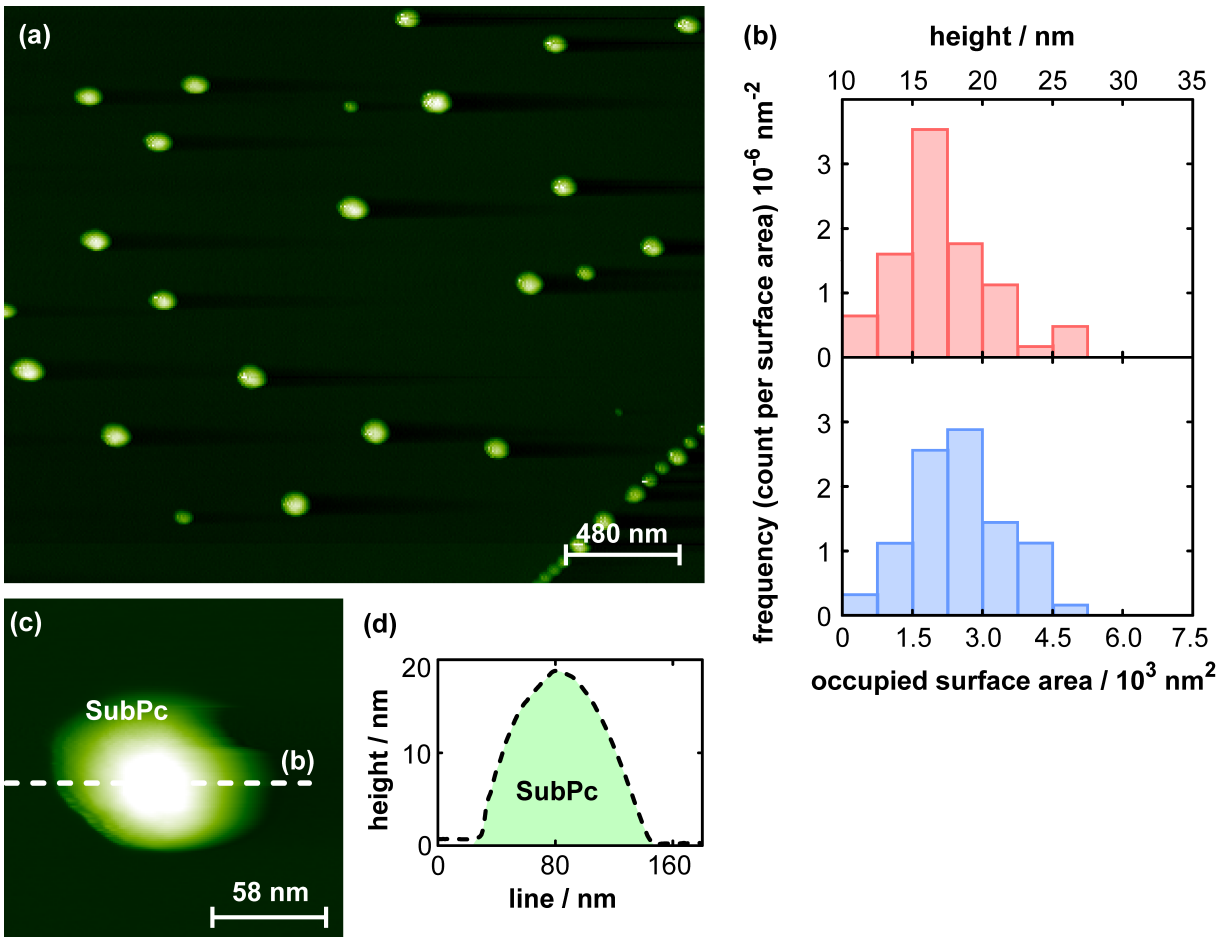

9.1 Growth of SubPc islands

SubPc molecules (see Sec. 6.2) were deposited on the CaF_2 (111) surface to a coverage of 0.6 ML within a period of 2 min. During deposition, the substrate was held at room temperature. An overview image is shown in Fig. 9.1(a). The density of islands is approximately 19 μm^{-2}. An analysis of sixty islands on flat surface terraces (Fig. 9.1(b)) yields a mean occupied surface area of 1500-3000 nm^2 and a height of about 17 nm. The small contact area compared to the extraordinary height of the islands is an expression of the low dewetting barrier and a small attractive interaction between the molecules and the substrate. A typical island is presented in Fig. 9.1(c) in more detail. A line scan in Fig. 9.1(d) reveals the rounded shape of the island. Although the atomic lattice of the substrate between the islands was resolved, it was not feasible to resolve the molecular structure of the islands. This can be attributed to the very compact and curved island structure, which does not allow for imaging of a flat island's area.

Figure 9.1: (a) NC-AFM overview image (topography). The image shows a large atomically flat terrace, with the SubPc islands equally distributed on the surface. In the lower right corner a substrate step edge is evident. SubPc islands nucleate along this step edge. (b) Statistic of sixty SubPc islands from terraces. Islands occupy a small surface area, but cluster very high. (c) NC-AFM image of a SubPc island with a corresponding line scan in (d).

9.2 Sequential deposition of SubPc and C_{60}

SubPc followed by C_{60}

On the SubPc coated sample as shown in Fig. 9.1, C_{60} molecules were deposited additionally (0.1 ML in 2 min). In Fig. 9.2(a) an overview image is shown after C_{60} deposition. The density of the islands is equal to the SubPc prepared sample. However, islands appear larger than observed for the pure SubPc islands. No pure C_{60} islands according to Sec. 8.2 were observed. Thus, the preexisting SubPc islands seem to act as nucleation sites for diffusing C_{60} molecules.

In Fig. 9.2(b) a common island is shown in detail. The island's outer shape is bulky and compact. The island consists of a high nucleus in the center and a flatter belt around. From the upper line scan in Fig. 9.2(d) it is apparent that the center nucleus has about the same height as a pure SubPc island, whereas the outer belt exhibits a height of 4 nm approximately. Thus, the center nucleus of the island can be dedicated to pure SubPc. The outer belt can be assigned to C_{60} molecules. A pure C_{60} arrangement would result in two layer high arrangement with straight edges as demonstrated in Sec. 8.2. Therefore, the bulky shape and the larger height of the belt allows to conclude an intermixed phase of C_{60} and SubPc molecules. The SubPc molecules of the intermixed phase are assumed to detach from the center nucleus.

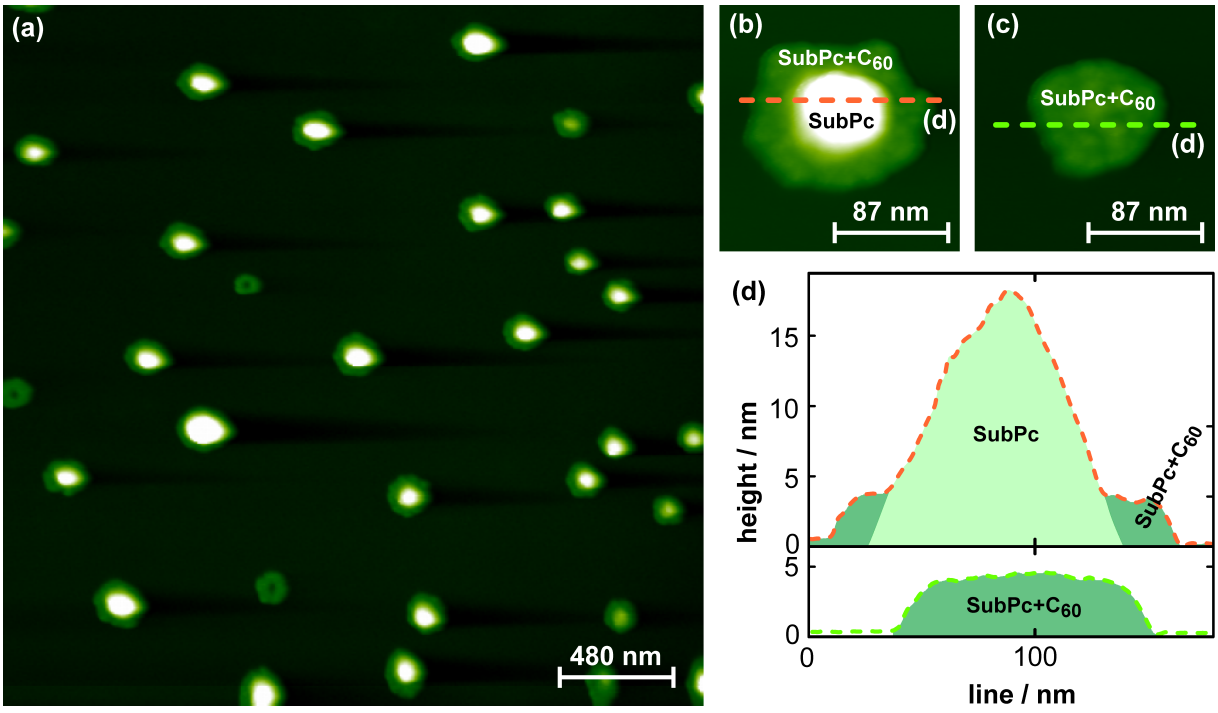

Figure 9.2: (a) Overview image (topography) of a SubPc prepared sample with subsequent desposition of C_{60}. C_{60} molecules nucleate at the initial SubPc islands. (b) Exemplary island with a SubPc nucleus in the center and an additional outer belt, consisting of a C_{60} /SubPc intermixed phase. (c) Exemplary island where the initial SubPc nucleus was small and has completely intermixed with the C_{60} molecules. (d) Line scans from (b) and (c).

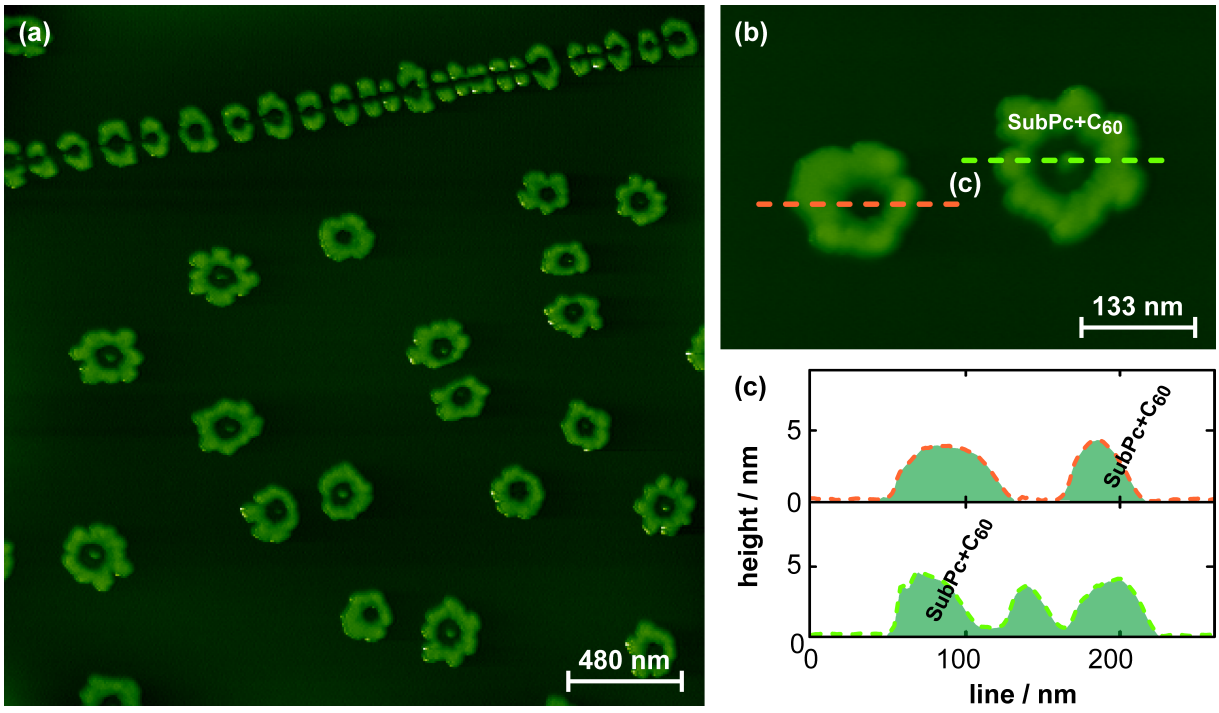

Figure 9.3: (a) Overview image (topography) after heating the sample presented in Fig. 9.2 to 505 K for 30 min. (b) Islands do preserve their intermixed outer belt, but the inner SubPc nucleus desorbs. (c) Line scans from (b).

As evident from NC-AFM images in Fig. 9.2(a) and (c) and the lower line scan in (d), some island do not possess a SubPc center nucleus. Rather, such islands often exhibit a small dip in the center. The islands can be assigned to a situation, where the initial SubPC nucleus was small and has completely mixed with C_{60} molecules. This assumption is strengthened by the fact that the height of these islands is about 4 nm, similar to the height of the intermixed phase of the outer belt of the previously described islands.

Trying to promote the intermixing, the sample was heated to approximately 505 K for 30 min and was subsequently imaged at room temperature. In Fig. 9.3(a) an overview image is presented. In the upper part of the image, a substrate step edge is apparent where islands are aligned. Details on the island structures are presented in Fig. 9.3(b). Like at the unheated sample, islands consist of a 4 nm high outer belt with bulky and compact shape. However, the inner SubPc nucleus is much smaller (right island) and in some cases has completely vanished (left island). The spot, where the former nucleus was situated is not occupied by the intermixed phase, but a gap occurs. If the whole nucleus has vanished, the bare substrate can be imaged. This is evident from line scans in Fig. 9.3(c). Thus, cavities were produced, surrounded by the intermixed phase. Because the outer belt does not enlarge in height or size in comparison to the unheated sample, it is assumed that the SubPc molecules desorb from the surface upon heating.

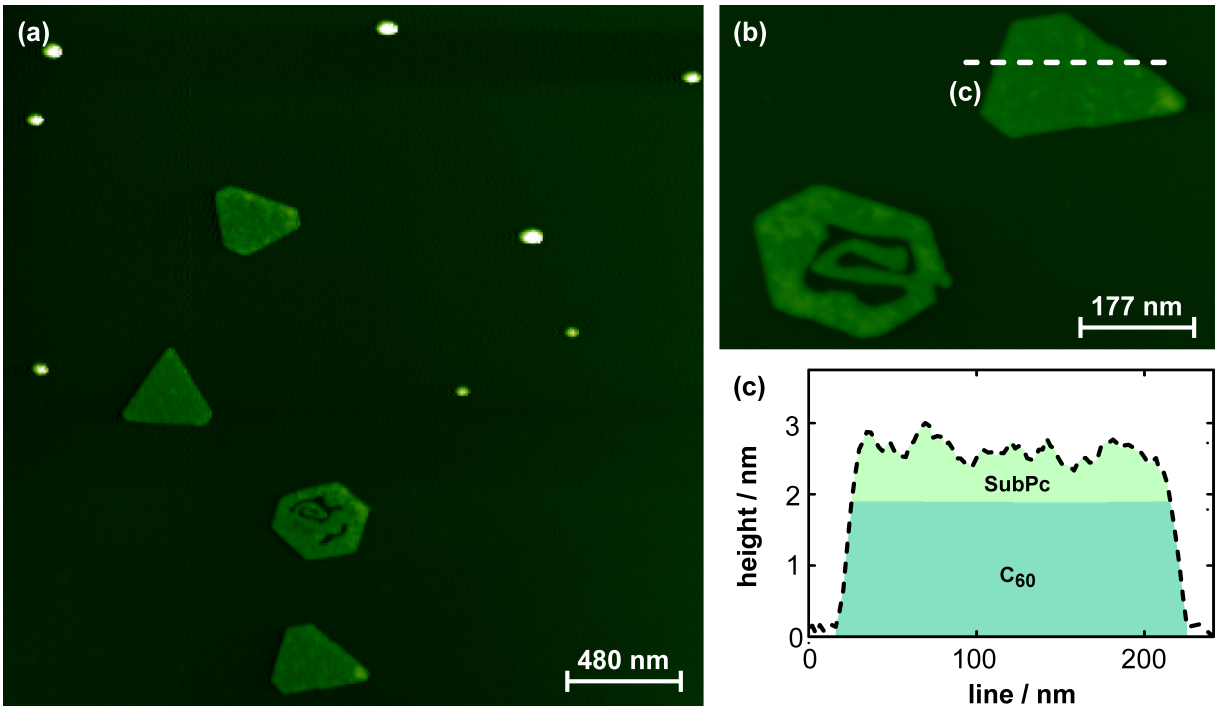

Figure 9.4: (a) Overview image (topography) after deposition of C_{60} followed by SubPc molecules. Pure SubPc islands can be identified as small and high islands, like in Fig. 9.1. C_{60} islands preserve their characteristic size and shape upon SubPc deposition. However, the C_{60} island surface appears rough, as evident in (b) and a corresponding line scan in (c). The line scan also reveals that the island is higher than a pure two layer C_{60} island would be. Thus, SubPc molecules dewet onto the C_{60} islands surfaces and form a relatively flat covering.

C_{60} followed by SubPc

In the following, the sequential growth of C_{60} followed by SubPc molecules is analyzed. In a first step, C_{60} molecules were deposited on the surface (0.1 ML within 2 min). Details on the C_{60} island's structures were presented previously in Sec. 8.2. The situation after subsequent deposition of SubPc (0.3 ML within 1 min) is shown in Fig. 9.4(a). In comparison to a solely C_{60} prepared sample some additional small islands are evident. These islands are similar to the pure SubPc islands described in Sec. 9.1. Therefore, these small islands are assigned to pure SubPc clusters. C_{60} islands keep their characteristic shape and size as they had before SubPc deposition. However, a closer look in Fig. 9.4(b) reveals a more ragged island surface than observed for pure C_{60} island. A corresponding line scan in Fig. 9.4(c) reveals, in addition, that the islands are more than the two expected C_{60} monolayers in height. Thus, it can be concluded that the C_{60} islands are covered by SubPc molecules. SubPc molecules seem to very easily dewet from the substrate surface on top of C_{60} island. Dewetted SubPc molecules do not cluster like on the bare CaF_2 (111), but lay comparatively flat on top of the C_{60} islands. Thus, a perfect stack with two layers of C_{60} molecules and SubPc layers on top was created, at which the C_{60} layers govern the outer shape. This indicates a stronger attractive interaction of the C_{60} with the SubPc molecules than the SubPc molecules

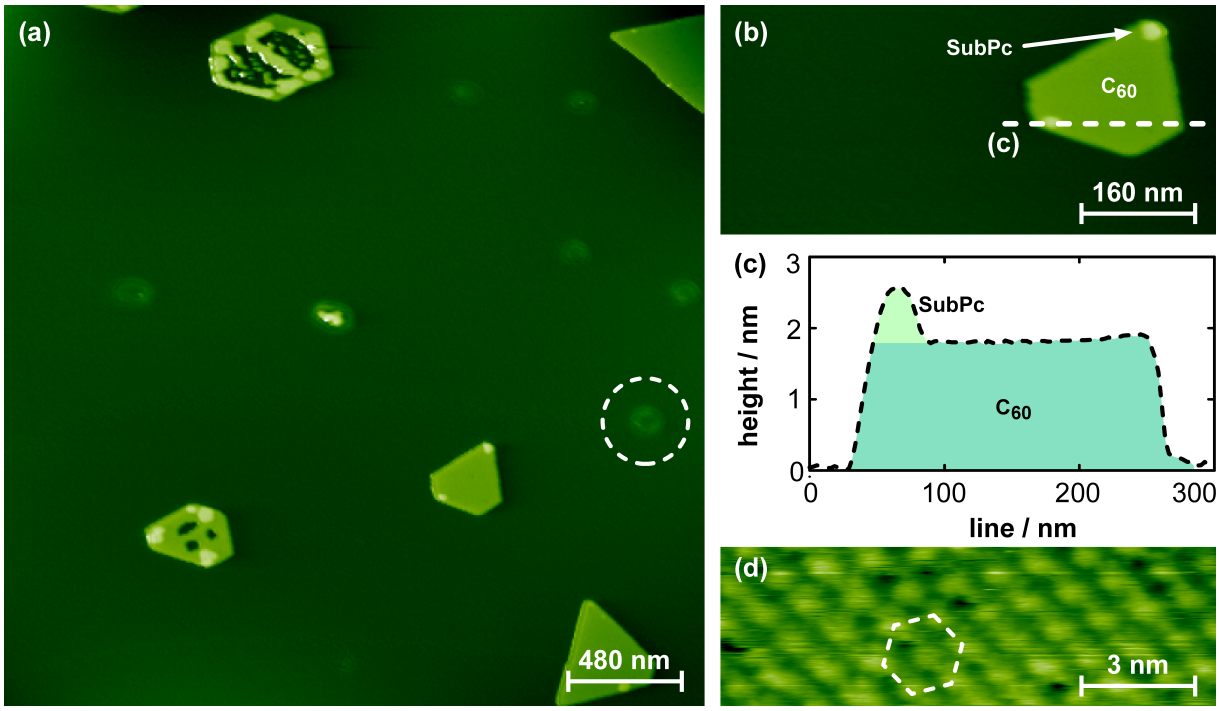

have with the substrate surface.

In Fig. 9.5(a) an overview image is shown after heating the sample to approximately 505 K for 30 min (imaging at room temperature). When heating the substrate, it can be seen that no intermixing had occurred at the interface of C_{60} and SubPc layers. Pure SubPc islands can be distinguished as faint structures in Fig. 9.5(a), one of which is encircled. Thus, similar to the SubPc center nucleus surrounded by C_{60} molecules, pure SubPc island dissolve upon heating. The C_{60} islands with on-top SubPc do preserve their characteristic shape and size. However, the SubPc layer on top desorbs to a large extend, which can be seen at the island in Fig. 9.5(b). The C_{60} island is only covered by some small residuals of SubPc, whereas the larger part of the island exhibits a pure C_{60} interface. A molecularly resolved image in Fig. 9.5(c) on top of the island proves the well ordered pure C_{60} island surface. This demonstrates that C_{60} molecules have not intermixed with the on-top SubPc layer. This can be assigned to the relatively stable, flat and close-packed C_{60} island surface.

Figure 9.5: (a) Overview image (topography) after heating the sample presented in Fig. 9.4 to 505 K for 30 min. Upon heating, SubPc islands nearly vanish. A faintly visible SubPc island is encircled. As evident in (b) and a corresponding line scan in (c), the SubPc covering the top of the C_{60} islands desorbs. The underlying arrangement of the C_{60} island is in perfect order, shown in (d). Thus, no intermixing has occurred at the C_{60}/SubPc interface.

9.3 Simultaneous deposition

In the preceding section, the sequential deposition of C_{60} and SubPc molecules was studied in both orders. Now, the simultaneous deposition is surveyed. Thereto, both molecules were deposited at the same time of 4 min onto the bare surface. This yields a coverage of C_{60} at 0.2 ML and a coverage of SubPc at 1.2 ML. An overview image is shown in Fig. 9.6(a). In the middle of the image, a substrate step edge is seen, where molecules nucleate. On the flat terraces, islands are equally distributed with a density of approximately 8 μm^{-2}. An island is presented in more detail in Fig. 9.6(b). Islands have a flower-like shape and are very equal to the previously observed outer shapes of C_{60}/SubPc intermixed phases, presented in Fig. 9.2 and Fig. 9.3. In addition, a line scan reveals an island height of about 4 nm, which is in agreement of the previously described intermixed phases. Thus, it can be concluded that a simultaneous deposition of C_{60} and SubPc molecules on the CaF_2 (111) results solely in intermixed islands.

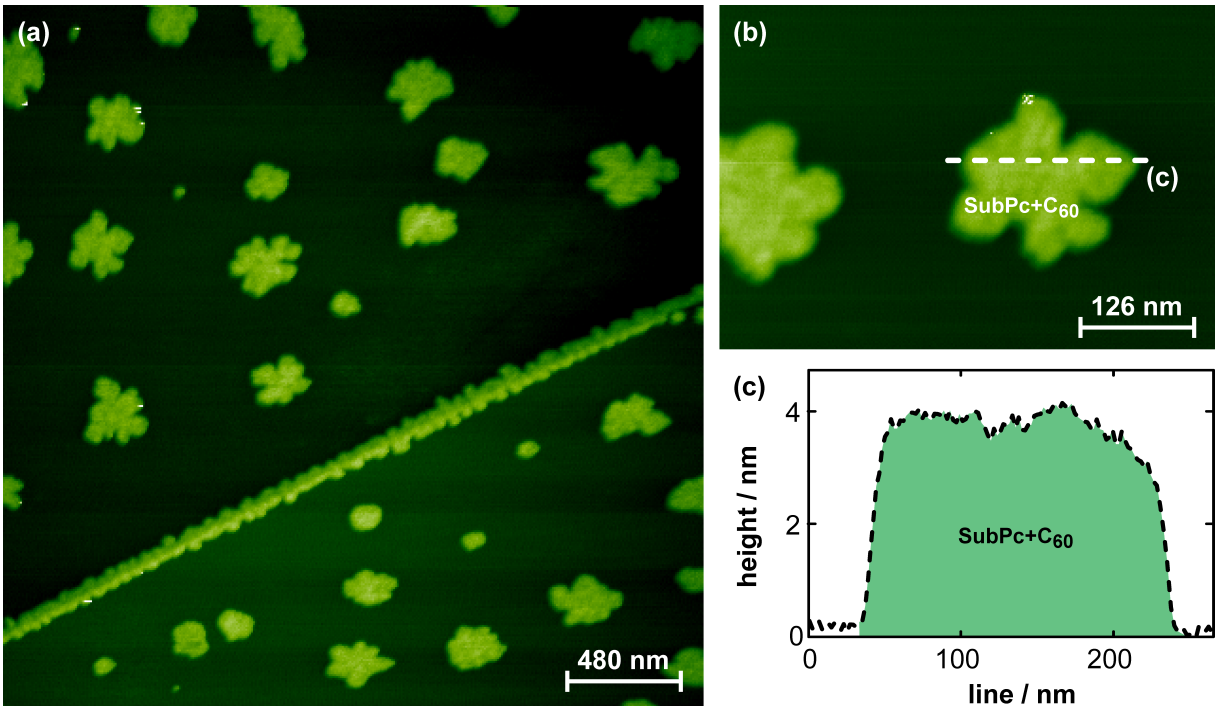

Figure 9.6: (a) Overview image (topography) of simultaneous deposition of SubPc and C_{60} molecules. Molecules cluster at the substrate step edge running through the image. (b) Islands on the flat terraces exhibit a flower-like outer shape. (c) Islands consist of a 4 nm high intermixed phase, similar to the outer belts in Fig. 9.2

9.4 Conclusion

On the CaF_2 (111) surface, the intermixing of C_{60} and SubPc depends on the order of deposition. Sequential deposition of first SubPc and second C_{60} yields an intermixed phase. In contrast, for the opposite deposition order, no intermixing takes place. Molecules arrange in two separated phases which lie on top of each other with the C_{60} phase facing the substrate and dictating the outer shape. The SubPc molecules form a relatively flat layer on top. This is in contrast to the strong clustering of SubPc molecules on the substrate surface. Upon heating, the SubPc molecules desorb from the C_{60} islands, whereas the C_{60} islands stay in perfect order.

Thus, it was demonstrated that the deposition order can strongly affect the molecular arrangement. For sequential deposition, intermixing of the molecule species may be promoted by deposition of the particular molecule species, which forms the less stable arrangement on the surface, in a first step. These less stable arrangements may easily be broken up in favor of an intermixing with the afterwards deposited molecule species. In contrast, intermixing may be reduced or completely inhibited by firstly depositing the molecule species with a more stable phase on the surface. These more stable arrangements may not be broken up so easily for an intermixing with the second molecule species.

10 Coadsorption of C_{60} and PTCDI molecules on the CaF_2 (111) surface

Contents

In the previous section the coadsorption of C_{60} and SubPc was explored. However, the SubPc have clustered very strongly which prohibited ordered structures to be observed in pure and coadsorbed phases. Thus, within this section, instead of SubPc, PTCDI (see Sec. 6.3) was chosen for codeposition with C_{60} on the CaF_2 (111) surface. PTCDI is known to arrange in ordered structures and nucleates in elongated, needle-shaped islands on another atomically flat insultaing substrate surface (NaCl(001)).[135] Thus, codepositing C_{60} and PTCDI, one may envision an arrangement at which the elongated PTCDI arrangements connect the compact, dot-like C_{60} islands. Thereto, the principles of coadsorption of C_{60} and PTCDI molecules are studied.

For each experiment, bare CaF_2 (111) surfaces were prepared according to Sec. 5.2. In a first step, the growth of pure PTCDI islands is analyzed shortly. Hereon, PTCDI and C_{60} molecules were codeposited onto the surface. Two different paths of coadsorption were tested: sequential and simultaneous deposition. Measurements took place at room temperature and were performed with the RHK 750 variable temperature force microscope under UHV conditions (see Sec. 3). The present study revealed that island formation can be regulated by modifying the deposition order, similar to the SubPC/C_{60} system described in the previous section.

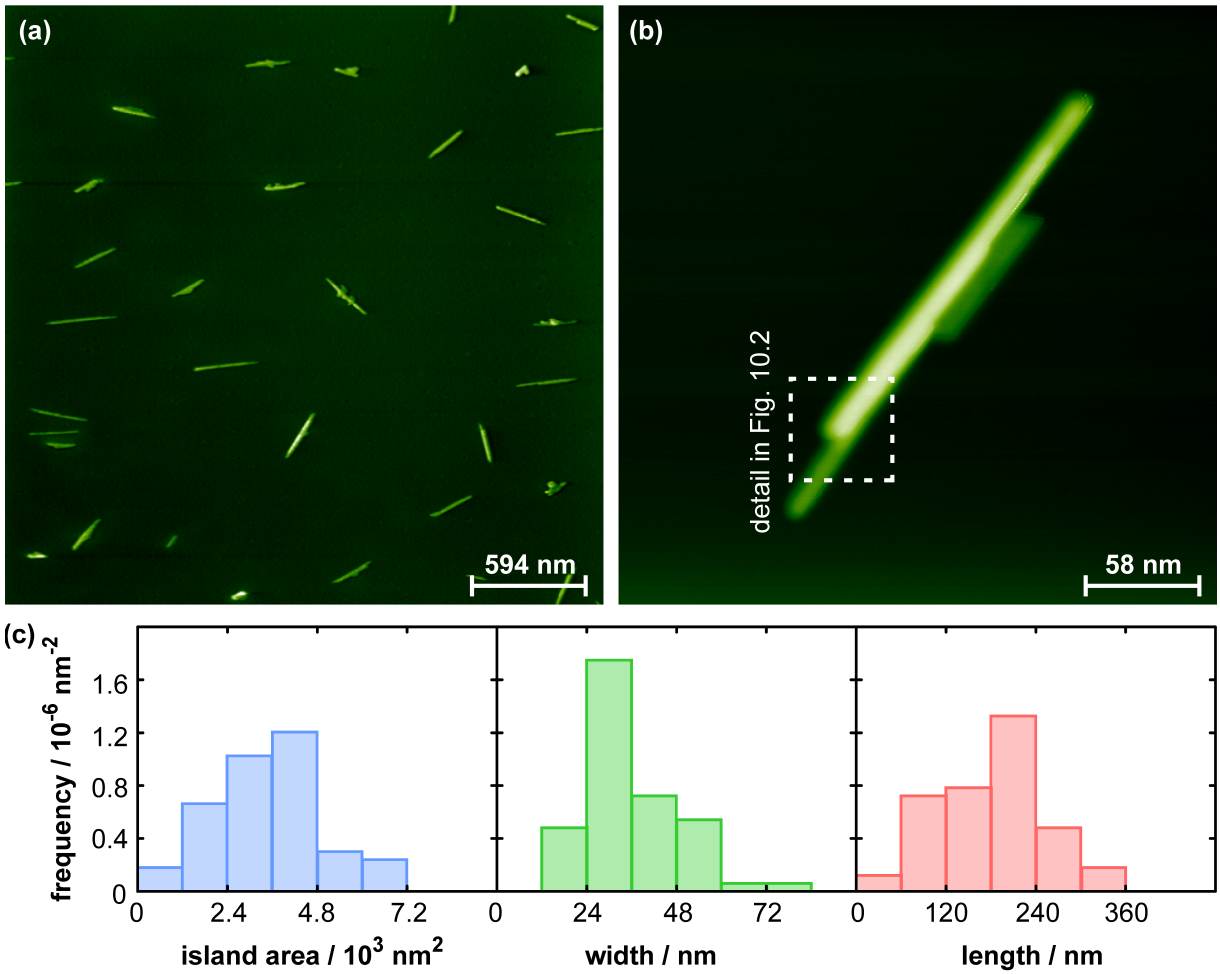

Figure 10.1: (a) NC-AFM overview image (topography). The image shows a large atomically flat terrace, with the PTCDI islands equally distributed on the surface. Islands are elongated and exhibit a needle-like shape. (b) PTCDI island revealing the elonagted shape and stepped arrangement. (c) Statistic of sixty PTCDI islands from terraces. The mean length-to-width ratio is about six.

10.1 Growth of PTCDI islands

PTCDI molecules (see Sec. 6.3) were deposited on the CaF_2 (111) surface to a coverage of 0.1 ML within a period of 2 min. During deposition, the substrate was held at room temperature. An overview image is shown in Fig. 10.1(a). The density of islands is approximately 4 μm^{-2}. Islands exhibit an elongated, needle-like shape as apperent from Fig. 10.1(b). An analysis of sixty islands on flat surface terraces (Fig. 10.1(c)) yields a mean occupied surface area of 3600-4800 nm^2. Island have mean dimensions of 30 nm $\times$ 180 nm. This yields a rather large length-to-width ratio of six. In Fig. 10.2(a) and (b) the internal structure of a PCTDI island is shown. It is apperent that the island is stepped and consists of up to six layers of PTCDI. The interlayer spacing is about 0.3 nm. Details of the molecular arrangement are shown in Fig. 10.2(d). Molecules are stringed in rows by intermolecular hydrogen-bonding. In alternating rows, molecules are con-

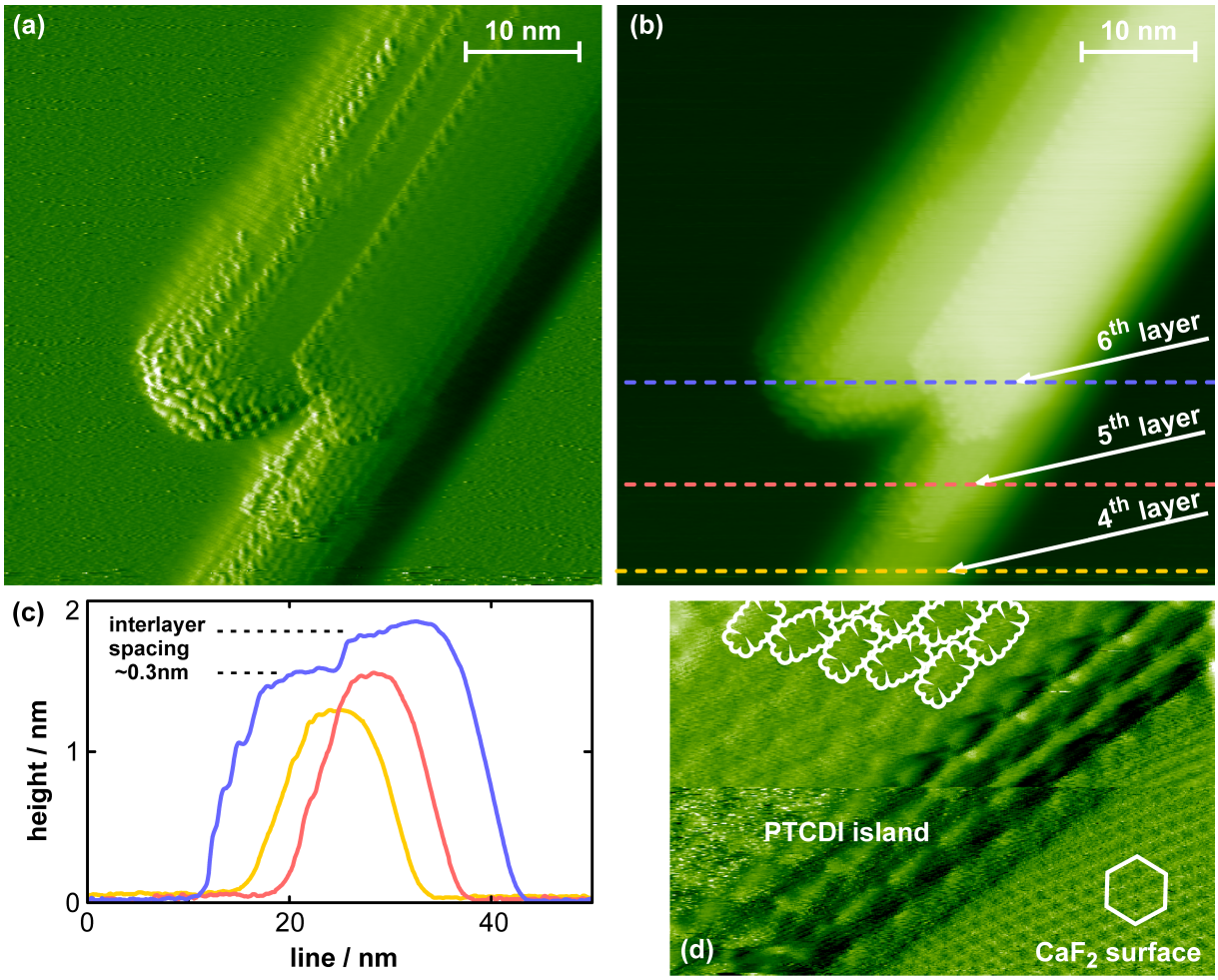

trarily rotated. This canted arrangement is in aggrement with the structure commonly observed for PTCDI molecules on metal and insulating surfaces, as described in Sec. 6.3. The molecular arrangement is similar to the $(10\bar{2})$ surface of a bulk PTCDI crystal. This suggests that the PTCDI molecules are not strongly affected by the CaF_2 (111) surface and arrange in their own, energetical favourable structure.

Figure 10.2: Detail on the PTCDI island shown in Fig. 10.1(b) with frequency shift (a) and topography channel (b), respecively. The NC-AFM images and corresponding line scans in (c) reveal that the island consists of flat, stacked PTCDI layers. Within the layers, molecules arrange in a canted phase as evident in (d).

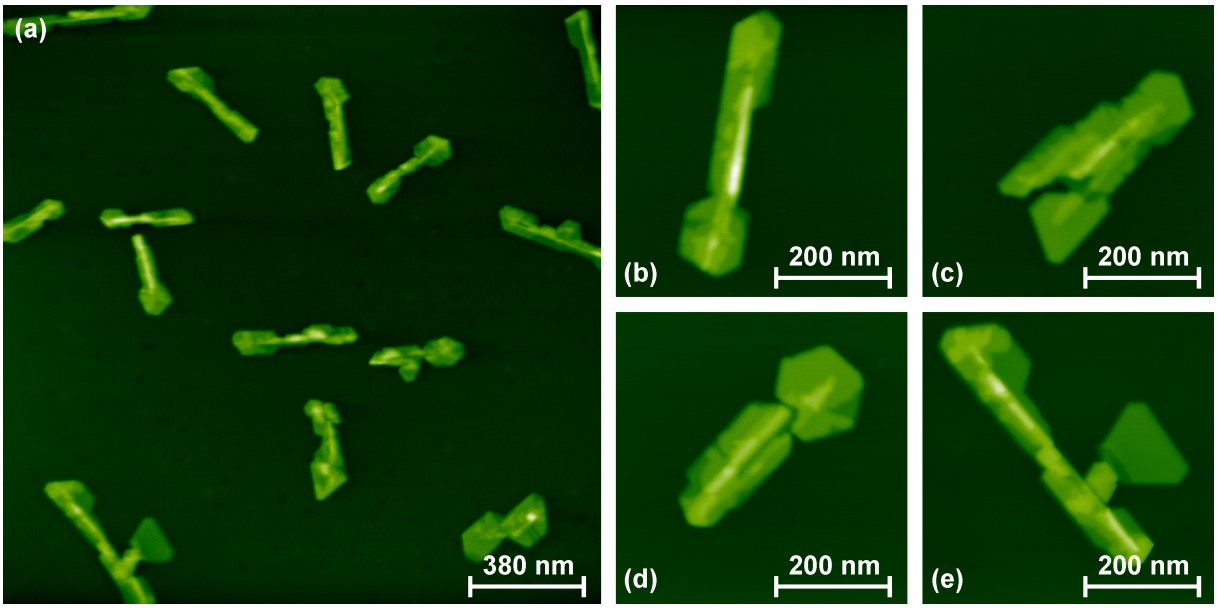

Figure 10.3: (a) Overview image (topography) of a sample with PTCDI islands with subsequent deposition of C_{60}. C_{60} molecules nucleate at the initial PTCDI islands. No isolated C_{60} islands were observed. (b)-(e) Detail images of C_{60} covered PTCDI islands. C_{60} molecules also form larger patches attached to the main elongated core.

10.2 Sequential deposition of PTCDI and C_{60}

PTCDI followed by C_{60}

On a PTCDI coated sample C_{60} molecules were deposited additionally (0.4 ML in 8 min). In Fig. 10.3(a) an overview image is shown after C_{60} deposition. Islands appear larger than observed for pure PTCDI islands. No pure C_{60} islands according to Sec. 8 were observed. Thus, the preexisting PTCDI islands seem to act as nucleation sites for diffusing C_{60} molecules.

In Fig. 10.3(b-e) common island formations are shown. A detailed view of the island in Fig. 10.3(e) is presented in Fig. 10.4(a). Islands consist of a narrow, elongated core. Arround this core, larger flat areas are attached. The stacked layers of the island are clearly visible. From line scans in Fig. 10.4(b) it is evident that the interlayer spacings are multiples of the spacing of close-packed C_{60}, which is 0.8 nm. In addition, the image in Fig. 10.4(c) shows a hexagonal close-packed arrangement on top of the island. Underneath the elevated broad body running from the lower right to the upper left, the PTCDI core is suspected. This indicates that the initial PTCDI island is completely covered by C_{60} molecules whereas also patches of pure C_{60} arrangement have formed around the PTCDI core. Thus, C_{60} molecules preferential attach to PTCDI islands and easily dewet on top of the PTCDI.

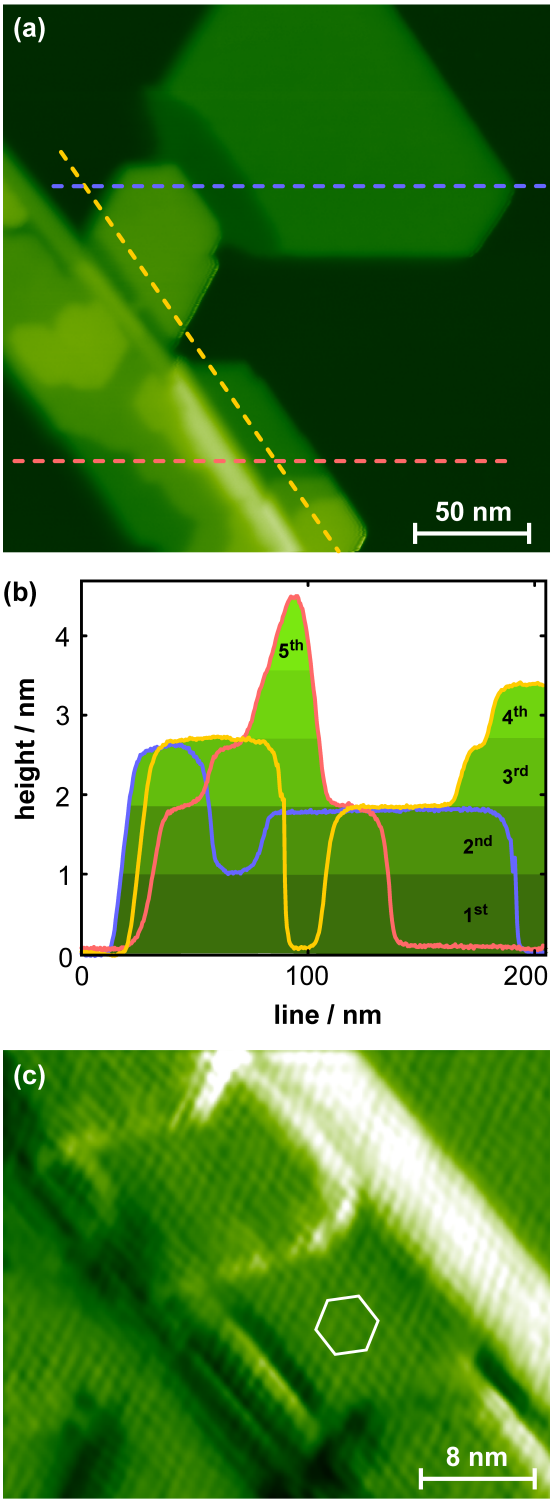

Figure 10.4: (a) Detail of Fig. 10.3(e), showing a C_{60} covered PTCDI island. The PTCDI core lies underneath the central elongated elevation. Line scans in (b) reveal an interlayer spacing of approximately 0.8 nm. (c) NC-AFM image (frequency shift, filtered) on top of a C_{60} covered PTCDI island showing a hexagonal arrangement, which can be identified as close-packed C_{60} layers.

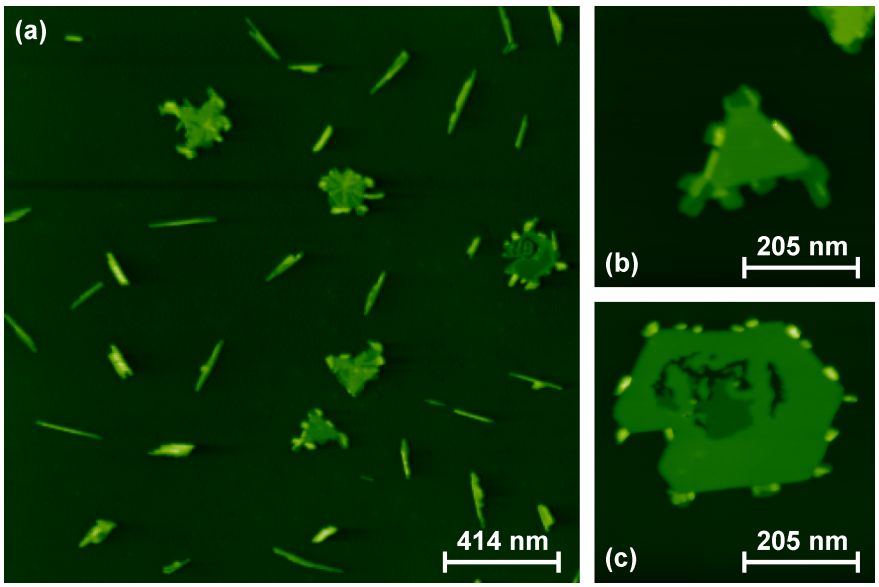

Figure 10.5: (a) Overview image (topography) of a sample covered with C_{60} islands with subsequent deposition of PTCDI molecules. PTCDI arrange in needle-shaped islands and only few PTCDI molecules attach to C_{60} islands. (a) and (b) C_{60} islands with small, attached PTCDI nuclei.

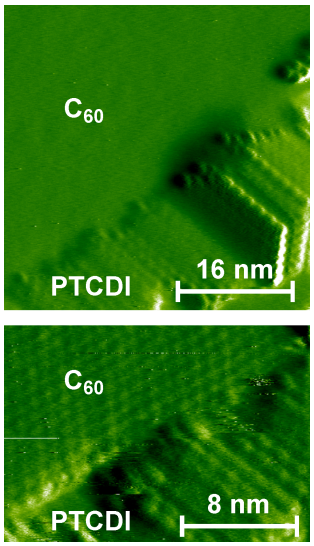

Figure 10.6: NC-AFM images (frequency shift) of PTCDI at C_{60} island edges. PTCDI molecules arrange in a canted phase.

C_{60} followed by PTCDI

Inspired by the observation of elongated, wire-like shape of pure PCTDI islands, it is envisioned that initially deposited C_{60} islands get connected through afterwards deposited PTCDI molecules. However, this is not the case. From Fig. 10.5(a) it is apparent that most of the deposited PTCDI arranges in needle-shaped islands, which are not attached to the initial C_{60} islands. Only few PTCDI clusters are observed at C_{60} islands, as evident in Fig. 10.5(b) and (c). Thus, C_{60} islands do not act as strong nucleation sites for freely diffusing PTCDI in contrast to PTCDI islands constituting nucleation sites for freely diffusing C_{60} molecules. In Fig. 10.6 edges of C_{60} islands are shown, which are decorated by PTCDI molecules. PTCDI molecules grow in a canted arrangement from the border. On top of the C_{60} islands, only few PTCDI molecules were observed. This suggests that PTCDI can not easily dewet from the surface on top of the C_{60} layer. This is in contrast to the sequential deposition of first C_{60} and second SubPc, described in the previous section. In the SubPc-C_{60} case, the SubPc molecules easily have dewetted from the surface on top the preexisting C_{60} islands.

10.3 Simultaneous deposition

In the preceding paragraphs, the sequential deposition of C_{60} and PTCDI molecules was studied in both orders. Now, the simultaneous deposition is surveyed. Thereto, both molecules were deposited at the same time of 2 min onto the bare surface. This yields the same coverage for C_{60}

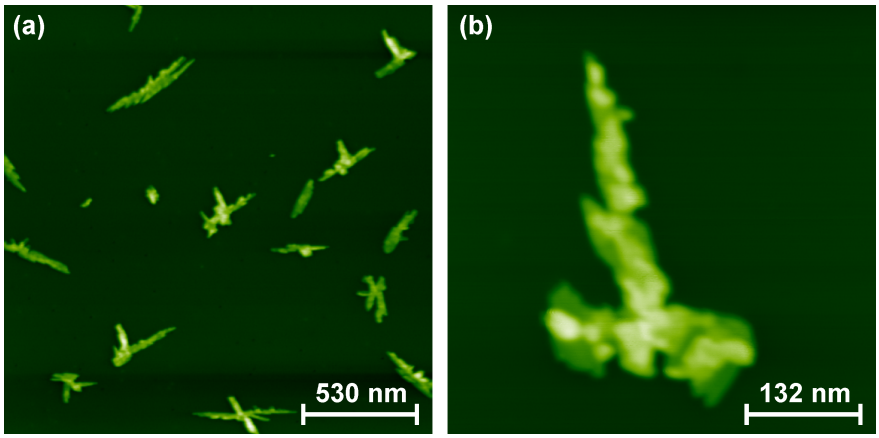

Figure 10.7: (a) Overview image (topography) of a CaF_2 (111) sample after simultaneous deposition of PTCDI and C_{60} molecules. (b) Islands exhibit a more ragged surface and shape than after sequential deposition.

and PTCDI at 0.1 ML. An overview image is shown in Fig. 10.7(a). On the flat terraces, islands are equally distributed with a density of approximately 4 μm^{-2}. An island is presented in more detail in Fig. 10.7(b). Islands have an elongated shape with attached branches. However, the outer edges and the island surface are rougher than for pure PTCDI islands and for C_{60}-covered PTCDI islands. This suggests a different arrangement of the PTCDI and C_{60} molecules, perhaps with an intermixed phase. However, molecular resolution was not achieved on these islands, hampering further clarification of the molecular arrangement after simultaneous deposition.

10.4 Conclusion

Deposition of PTCDI molecules on the CaF_2 (111) yields elongated, needle-shaped islands. Molecules arrange in a canted phase. Upon sequential deposition of C_{60} molecules, PTCDI islands become completely covered by C_{60}. In contrast, for the opposite deposition order, PTCDI molecules do not cover initial C_{60} islands. Most of the PTCDI molecules arrange in pure islands, only few PTCDI molecules nucleate at the edges of C_{60} islands. Thus, PTCDI molecules do not dewet as easily on top of C_{60} islands as C_{60} molecules dewet on top of PTCDI islands. In contrast to the SubPc/C_{60} bimolecular system, no intermixing of PTCDI and C_{60} takes place upon a sequential deposition. Thus, the PTCDI arrangement is assumed to be much more stable on the CaF_2 (111) surface than the SubPc arrangement. This can also be deduced from the fact that SubPc molecules cluster very strongly on the surface, whereas PTCDI molecules arrange in well ordered, relatively flat islands on the surface.

11 Summary

In the present thesis, NC-AFM was employed to explore self-assembled molecular arrangements on insulating substrate surfaces at various temperatures. Substrate preparation, molecule deposition and measurements took place under UHV conditions.

Within the first sections, C_{60} molecules were deposited on the TiO_2 (110) surface at room temperature. The C_{60} molecules were found to adsorb in the troughs between the substrate's bridging oxygen rows, forming a rhombic unit cell. Molecules arrange in compact and regularly-shaped islands. Although the TiO_2 (110) surface is known to exhibit a high density of defects, the C_{60} islands were of striking perfection. Protruding molecular rows within the islands were identified as domain boundaries between two adjacent C_{60} islands resulting from stacking faults. Upon increasing the tip-sample interaction during scanning, C_{60} islands were modified. A domain boundary was shifted along its entire length, by a tip-induced movement of the causative stacking fault. Besides, it was possible to reproducibly induce holes into the perfectly ordered C_{60} islands.

In the following section, C_{60} molecules were investigated on the CaF_2 (111) surface. In a first step, the growth of C_{60} islands was explored at low temperatures. At these temperatures, islands consist of hexagonally shaped first layers with small second layer nuclei on top. Analyzing island sizes and densities at various temperatures, the diffusion barrier was determined from experiments. As expected, the quantified diffusion barrier on this insualting substrate surface is much lower than for molecule-metal systems. In a second step, the shape of C_{60} islands was investigated at temperatures around room temperature. Deposition of C_{60} molecules at substrate temperatures in the range between 297 K and 319 K results in distinctly different island structures. At the lower temperature, branched hexagonally shaped first-layer islands with a second layer outer rim arise. At the higher temperature, compact triangular islands emerge. These islands consist of at least two completed C_{60} layers. For temperatures between, both types of islands coexist. Based on temperature-dependent and time-resolved measurements, a model at the molecular level was assumed for the origin and evolution of the different observed island structures. It

was found that a second-layer induced dewetting process plays the major role in island formation. In conclusion, for this molecule-insulator system, the island growth was found to be fundamentally different to molecule-metal systems.

In the next section, C_{60} molecules were codeposited with SubPc molecules on the CaF_2 (111) surface to further craft molecular arrangement. Sequential deposition of first SubPc and second C_{60} yields an intermixed phase. In contrast, for the opposite deposition order, no intermixing takes place. Molecules arrange in two separated phases which lie on top of each other with the C_{60} phase facing the substrate and dictating the outer shape. The SubPc molecules form a relatively flat layer on top. This is in contrast to the strong clustering of SubPc molecules on the substrate surface. Upon heating, the SubPc molecules desorb from the C_{60} islands, whereas the C_{60} islands stay in perfect order. Thus, for this bimolecular system, it was demonstrated that the deposition order can strongly affect the molecular arrangement.

In the last section, C_{60} molecules were codeposited with PTCDI molecules on the CaF_2 (111) surface. A deposition of pure PTCDI results in needle-shaped islands which are always more than two layers in height. Molecules arrange in adjacent rows driven by intermolecular hydrogen-bonding like in their bulk structure. Upon a sequential deposition of C_{60} molecules, the PTCDI islands act as nucleation sites for the C_{60} molecules and get covered by C_{60} molecules. No pure, separated C_{60} islands were observed in this case. At a sequential deposition of C_{60} followed by PCTDI, small PTCDI clusters grow at the edges of the C_{60} islands. The inner structure of the C_{60} islands is not affected by the PTCDI molecules. Thus, also at this bimolecular system, the deposition order affects the molecular arrangement.

In conclusion, molecule nanostructures were tailored by very different approaches. Structures were influenced by the surface morphology, the deposition temperature and the codeposition with second molecule species. Beyond, structures were further crafted after deposition by tip-induced manipulation and thermal activation (heating). Due to the very different approaches much is learnt about the impacts, which influence the island formation of molecules on insulating surfaces. This new and detailed insight into island formation may be exploited to produce advanced molecular nanostructures on insulating surfaces.

Appendices

App. A

The derivation of the density of stable clusters is given by

$$\frac{\mathrm{d}N}{\mathrm{d}t} = \sum_{s=i^*+1}^{\infty} \frac{\mathrm{d}n_s}{\mathrm{d}t} \tag{A.1}$$

Using Eqn. 4.15 gives

$$\begin{aligned} \frac{\mathrm{d}N}{\mathrm{d}t} &= \sum_{s=i^*+1}^{\infty} \Gamma_{s-1} - \Gamma_s \\ &= \Gamma_{i^*} - \underbrace{\Gamma_{i^*+1} + \Gamma_{i^*+1} - \Gamma_{i^*+2} + \Gamma_{i^*+2} - \dots}_{0} \\ &= \Gamma_{i^*} \end{aligned} \tag{A.2}$$

Using the identity for the netrate Γ_{i^*} from Eqn. 4.13 gives

$$\frac{\mathrm{d}N}{\mathrm{d}t} = \sigma_s D n_1 n_{i^*} - \gamma_{i^*+1} n_{i^*+1} \tag{A.3}$$

Finally, $\gamma_s = 0$ for $s > i^*$, i.e. $\gamma_{i^*+1} = 0$, yields

$$\frac{\mathrm{d}N}{\mathrm{d}t} = \sigma_s D n_1 n_{i^*} \tag{A.4}$$

App. B

Starting with

$$\frac{dn_1}{dt} = F - 2\Gamma_1 - \sum_{s=2}^{\infty} \Gamma_s \tag{B.1}$$

The thermal equilibrium among unstable cluster implies $\Gamma_s = 0$ for $1 \leq s \leq i^* - 1$ (see main text). Thus, the formula reads

$$\frac{dn_1}{dt} = F - \sum_{s=i^*}^{\infty} \Gamma_s \tag{B.2}$$

Using the identity Eqn. 4.13 and the assumption that stable clusters do not decay ($\gamma_s = 0$ for $s \geq i^* + 1$, see main text)

$$\begin{aligned} \frac{dn_1}{dt} &= F - \sum_{s=i^*}^{\infty} \sigma_s D n_1 n_s - \gamma_{s+1} n_{s+1} \\ &= F - \sum_{s=i^*}^{\infty} \sigma_s D n_1 n_s \\ &= F - \sigma_s D n_1 n_{i^*} - \sum_{s=i^*+1}^{\infty} \sigma_s D n_1 n_s \end{aligned} \tag{B.3}$$

Introducing the average capture number $\bar{\sigma}$ from Eqn. 4.18 yields

$$\frac{dn_1}{dt} = F - \sigma_s D n_1 n_{i^*} - \bar{\sigma} D n_1 N \tag{B.4}$$

App. C

For the solution of the differential equation

$$\frac{\mathrm{d}N}{\mathrm{d}t} = \frac{\sigma_{i^*}}{\bar{\sigma}^{i^*+1}}\Omega^{i^*-1}\left(\frac{F}{D}\right)^{i^*} F\mathrm{e}^{\beta E_{i^*}} N^{-(i^*+1)} \tag{C.1}$$

the following ansatz for the density of stable clusters $N(t)$ is choosen

$$N(t) = \left[c_1 t\,(1-c_2)\right]^{\frac{1}{1-c_2}} \tag{C.2}$$

Differentiating Eqn. C.2 with respect to time t yields

$$\begin{aligned}\frac{\mathrm{d}N}{\mathrm{d}t} &= \frac{1}{1-c_2}\left[c_1 t\,(1-c_2)\right]^{\frac{1}{1-c_2}-1} c_1(1-c_2)\\ &= c_1\left\{\left[c_1 t\,(1-c_2)\right]^{\frac{1}{1-c_2}}\right\}^{c_2}\\ &= c_1 N(t)^{c_2}\end{aligned} \tag{C.3}$$

Comparing Eqn. C.3 with Eqn. C.1 indicates straightforward

$$c_1 = \frac{\sigma_{i^*}}{\bar{\sigma}^{i^*+1}}\Omega^{i^*-1}\left(\frac{F}{D}\right)^{i^*} F\mathrm{e}^{\beta E_{i^*}} \tag{C.4}$$

$$c_2 = -(i^*+1) \tag{C.5}$$

By this means, the density of stable clusters $N(t)$ presents oneself as

$$N(t) = \left[(i^*+2)\left(\frac{\sigma_{i^*}}{\bar{\sigma}^{i^*+1}}\Omega^{i^*-1}\left(\frac{F}{D}\right)^{i^*} F\mathrm{e}^{\beta E_{i^*}}\right) t\right]^{\frac{1}{i^*+2}} \tag{C.6}$$

Finally, the time t is substituted in Eqn. C.6 with the simple relation $\theta = \Omega F t$. Thus, the number of stable clusters per adsorption site $\hat{N}$ reads

$$\hat{N} \equiv \Omega N = \left[(i^*+2)\frac{\sigma_{i^*}}{\bar{\sigma}^{i^*+1}}\theta\right]^{\frac{1}{i^*+2}}\left(\frac{\Omega^2 F}{D}\right)^{\frac{i^*}{i^*+2}} \mathrm{e}^{\frac{\beta E_{i^*}}{i^*+2}} \tag{C.7}$$

Bibliography

1. J. V. Barth, G. Costantini, K. Kern: Engineering atomic and molecular nanostructures at surfaces.
   Nature **437**, 671 (2005)

2. C. Joachim, J. K. Gimzewski, A. Aviram: Electronics using hybrid-molecular and mono-molecular devices.
   Nature **408**, 541 (2000)

3. G. E. Moore: Cramming more components onto integrated circuits.
   Electronics **38**, 114 (1965)

4. D. Eigler, E. Schweizer: Positioning single atoms with a scanning tunneling microscope.
   Nature **344**, 524 (1990)

5. G. Meyer, J. Repp, S. Zöphel, K.-F. Braun, S. W. Hla, S. Fölsch, L. Bartels, F. Moresco, K. H. Rieder: Controlled manipulation of atoms and small molecules with a low temperature scanning tunneling microscope.
   Single Mol. **1**, 79 (2000)

6. T. Junno, K. Deppert, L. Montelius, L. Samuelson: Controlled manipulation of nanoparticles with an atomic force microscope.
   Appl. Phys. Lett. **66**, 3627 (1995)

7. G. M. Whitesides, B. Grzybowski: Self-assembly at all scales.
   Science **295**, 2418 (2002)

8. A. Kühnle: Self-assembly of organic molecules at metal surfaces.
   Curr. Opin. Coll. Interf. Sci. **14**, 157 (2009)

9. J. V. Barth: Molecular architectonic on metal surfaces.
   Annu. Rev. Phys. Chem **58**, 375 (2007)

10. G. Binnig, C. Quate, C. Gerber: Atomic force microscope.
    Phys. Rev. Lett. **56**, 930 (1986)

11. T. R. Albrecht, P. Grütter, D. Horne, D. Rugar: Frequency-modulation detection using high-Q cantilevers for enhanced force microscope sensitivity.
    J. Appl. Phys. **69**, 668 (1991)

12. F. J. Giessibl: Advances in atomic force microscopy.
Rev. Mod. Phys. **75**, 949 (2003)

13. P. Rahe, R. Bechstein, J. Schütte, F. Ostendorf, A. Kühnle: Repulsive interaction and contrast inversion in noncontact atomic force microscopy imaging of adsorbates.
Phys. Rev. B **77**, 195410 (2008)

14. G. Meyer, N. M. Amer: Novel optical approach to atomic force microscopy.
Appl. Phys. Lett. **53**, 1045 (1988)

15. G. Meyer, N. M. Amer: Erratum: novel optical approach to atomic force microscopy.
Appl. Phys. Lett. **53**, 2400 (1988)

16. J. N. Israelachvili: Intermolecular and Surface Forces. Second Edition.
London, UK : Academic Press, 1985

17. H. C. Hamaker: The London-van der Waals attraction between spherical particles.
Physica **4**, 1058 (1937)

18. F. London: The general theory of molecular forces.
Trans. Faraday Soc. **33**, 8 (1937)

19. S. Sadewasser, M. C. Lux-Steiner: Correct height measurement in noncontact atomic force microscopy.
Phys. Rev. Lett. **91**, 266101 (2003)

20. M. Guggisberg, M. Bammerlin, C. Loppacher, O. Pfeiffer, A. Abdurixit, V. Barwich, R. Bennewitz, A. Baratoff, E. Meyer, H. J. Güntherodt: Separation of interactions by noncontact force microscopy.
Phys. Rev. B **61**, 11151 (2000)

21. J. E. Lennard-Jones: Cohesion.
Proc. Phys. Soc. **43**, 461 (1931)

22. photo used with permission from .

23. U. Zerweck, C. Loppacher, T. Otto, S. Grafström, L. M. Eng: Accuracy and resolution limits of Kelvin probe force microscopy.
Phys. Rev. B **71**, 125424 (2005)

24. S. Gritschneder, Y. Namai, Y. Iwasawa, M. Reichling: Structural features of CeO_2(111) revealed by dynamic SFM.
Nanotechnology **16**, S41 (2005)

25. J. C. Schütte: Abbildung organischer Moleküle auf dielektrischen Oberflächen, Universität Osnabrück, PhD thesis, 2009

26. R. Bechstein: Pristine and doped titanium dioxide studied by NC-AFM, Universität Osnabrück, PhD thesis, 2009

27. F. Ostendorf: Strukturuntersuchungen an mineralischen und polaren Oberflächen, Universität Osnabrück, PhD thesis, 2008

28. T. Michely, J. Krug: Islands, mounds and atoms: patterns and processes in crystal growth far from equilibrium. Berlin, Germany : Springer Verlag, 2004

29. J. A. Venables: Introduction to Surface and Thin Film Processes. Cambridge, United Kingdom : Cambridge University Press, 2000

30. E. Bauer: Phänomenologische Theorie der Kristallabscheidung an Oberflächen I.
Z. Kristallogr. **110**, 372 (1958)

31. J. H. Van't Hoff: Etudes de Dynamique Chimique. Frederik Muller and Co., Amsterdam, 1884

32. S. Arrhenius: Über die Reaktionsgeschwindigkeit bei der Inversion von Rohrzucker durch Säuren.
Z. Phys. Chem. **4**, 226 (1889)

33. S. Arrhenius: Zur Theorie der chemischen Reaktionsgeschwindigkeit.
Z. Phys. Chem. **28**, 317 (1899)

34. J. Weckesser, J. V. Barth, K. Kern: Direct observation of surface diffusion of large organic molecules at metal surfaces: PVBA on Pd(110).
J. Chem. Phys. **110**, 5351 (1999)

35. J. Weckesser, J. V. Barth, K. Kern: Mobility and bonding transition of C_{60} on Pd(110).
Phys. Rev. B **64**, 161403 (2001)

36. M. Schunack, T. R. Linderoth, F. Rosei, E. Lægsgaard, I. Stensgaard, F. Besenbacher: Long jumps in the surface diffusion of large molecules.
Phys. Rev. Lett. **88**, 156102 (2002)

37. R. Gomer: Diffusion of adsorbates on metal-surfaces.
Rep. Prog. Phys. **53**, 917 (1990)

38. H. Brune: Microscopic view of epitaxial metal growth: nucleation and aggregation.
Surf. Sci. Rep. **31**, 121 (1998)

39. J. V. Barth: Transport of adsorbates at metal surfaces: from thermal migration to hot precursors.
Surf. Sci. Rep. **40**, 75 (2000)

40. J. V. Barth, H. Brune, B. Fischer, J. Weckesser, K. Kern: Dynamics of surface migration in the weak corrugation regime.
Phys. Rev. Lett. **84**, 1732 (2000)

41. J. Krug: Four lectures on the physics of crystal growth.
Phys. Stat. Mech. Appl. **313**, 47 (2002)

42. P. Rahe, M. Nimmrich, A. Greuling, J. Schütte, I. Stará, J. Rybáek, G. Huerta-Angeles, I. Starý, M. Rohlfing, A. Kühnle: Toward molecular nanowires self-Assembled on an insulating substrate: heptahelicene-2-carboxylic acid on calcite (10-14).
J. Phys. Chem. C **114**, 1547 (2010)

43. J. Schütte, R. Bechstein, M. Rohlfing, M. Reichling, A. Kühnle: Cooperative mechanism for anchoring highly polar molecules at an ionic surface.
Phys. Rev. B **80**, 205421 (2009)

44. P. A. Gravil, M. Devel, P. Lambin, X. Bouju, C. Girard, A. A. Lucas: Adsorption of C_{60} molecules.
Phys. Rev. B **53**, 1622 (1996)

45. T. Kunstmann, A. Schlarb, M. Fendrich, T. Wagner, R. Möller, R. Hoffmann: Dynamic force microscopy study of 3,4,9,10-perylenetetracarboxylic dianhydride on KBr(001).
Phys. Rev. B **71**, 121403 (2005)

46. S. A. Burke, J. M. Topple, P. Gruetter: Molecular dewetting on insulators.
J. Phys. Condens. Matter **21**, 423101 (2009)

47. R. Lüthi, E. Meyer, H. Haefke, L. Howald, W. Gutmannsbauer, H. J. Güntherodt: Sled-type motion on the nanometer scale: determination of dissipation and cohesive energies of c_{60}.
Science **266**, 1979 (1994)

48. M. R. Sørensen, K. W. Jacobsen, H. Jónsson: Thermal diffusion processes in metal-tip-surface interactions: contact formation and adatom mobility.
Phys. Rev. Lett. **77**, 5067 (1996)

49. M. Bott, M. Hohage, M. Morgenstern, T. Michely, G. Comsa: New approach for determination of diffusion parameters of adatoms.
Phys. Rev. Lett. **76**, 1304 (1996)

50. Y. W. Mo: Direct determination of surface-diffusion by displacement distribution measurement with scanning-tunneling-microscopy.
Phys. Rev. Lett. **71**, 2923 (1993)

51. M. Ternes, C. P. Lutz, C. F. Hirjibehedin, F. J. Giessibl, A. J. Heinrich: The force needed to move an atom on a surface.
Science **319**, 1066 (2008)

52. Y. Sugimoto, P. Jelinek, P. Pou, M. Abe, S. Morita, R. Pérez, O. Custance: Mechanism for room-temperature single-atom lateral manipulations on semiconductors using dynamic force microscopy.
Phys. Rev. Lett. **98**, 106104 (2007)

53. S. Hirth, F. Ostendorf, M. Reichling: Lateral manipulation of atomic size defects on the CaF_2(111) surface.
Nanotechnology **17**, S148 (2006)

54. F. Loske, A. Kühnle: Manipulation of C_{60} islands on the rutile TiO_2 (110) surface using noncontact atomic force microscopy.
Appl. Phys. Lett. **95**, 043110 (2009)

55. D. Walton: Nucleation of vapor deposits.
J. Chem. Phys. **37**, 2182 (1962)

56. J. A. Venables: Rate equation approaches to thin-film nucleation kinetics.
Philos. Mag. **27**, 697 (1973)

57. J. A. Venables, G. D. T. Spiller, M. Hanbucken: Nucleation and growth of thin-films.
Rep. Prog. Phys. **47**, 399 (1984)

58. H. Brune, G. S. Bales, J. Jacobsen, C. Boragno, K. Kern: Measuring surface diffusion from nucleation island densities.
Phys. Rev. B **60**, 5991 (1999)

59. B. Krause, A. C. Durr, K. Ritley, F. Schreiber, H. Dosch, D. Smilgies: Structure and growth morphology of an archetypal system for organic epitaxy: PTCDA on Ag(111).
Phys. Rev. B **66**, 235404 (2002)

60. B. Müller, T. Kuhlmann, K. Lischka, H. Schwer, R. Resel, G. Leising: MBE growth of para-hexaphenyl on GaAs(001)-2×4.
Surf. Sci. **418**, 256 (1998)

61. G. Berlanda, M. Campione, M. Moret, A. Sassella, A. Borghesi: Evidence of postdeposition nucleation in organic molecular thin films.
Phys. Rev. B **69**, 085409 (2004)

62. M. Tejima, K. Kita, K. Kyuno, A. Toriumi: Study on the growth mechanism of pentacene thin films by the analysis of island density and island size distribution.
Appl. Phys. Lett. **85**, 3746 (2004)

63. Y. H. Tang, Y. Wang, G. Wang, H. B. Wang, L. X. Wang, D. H. Yan: Vacuum-deposited submonolayer thin films of a three-ring bent-core compound.
J. Phys. Chem. B **108**, 12921 (2004)

64. R. Ruiz, B. Nickel, N. Koch, L. C. Feldman, R. F. Haglund, A. Kahn, F. Family, G. Scoles: Dynamic scaling, island size distribution, and morphology in the aggregation regime of submonolayer pentacene films.
Phys. Rev. Lett. **91**, 136102 (2003)

65. B. Stadlober, U. Haas, H. Maresch, A. Haase: Growth model of pentacene on inorganic and organic dielectrics based on scaling and rate-equation theory.
Phys. Rev. B **74**, 165302 (2006)

66. S. Pratontep, F. Nüsch, L. Zuppiroli, M. Brinkmann: Comparison between nucleation of pentacene monolayer islands on polymeric and inorganic substrates.
Phys. Rev. B **72**, 136102 (2005)

67. F.-J. Meyer zu Heringdorf, M. C. Reuter, R. M. Tromp: The nucleation of pentacene thin films.
Appl. Phys. A **78**, 787 (2004)

68. T. Vicsek, F. Family: Dynamic scaling for aggregation of clusters.
Phys. Rev. Lett. **52**, 1669 (1984)

69. F. Family, P. Meakin: Scaling of the droplet-size distribution in vapor-deposited thin-films.
Phys. Rev. Lett. **61**, 428 (1988)

70. M. C. Bartelt, J. W. Evans: Scaling analysis of diffusion-mediated island growth in surface-adsorption processes.
Phys. Rev. B **46**, 12675 (1992)

71. J. G. Amar, F. Family, P. M. Lam: Dynamic scaling of the island-size distribution and percolation in a model of submonolayer molecular-beam epitaxy.
Phys. Rev. B **50**, 8781 (1994)

72. J. G. Amar, F. Family: Critical cluster-size - island morphology and size distribution in submonolayer epitaxial-growth.
Phys. Rev. Lett. **74**, 2066 (1995)

73. A. L. Linsebigler, G. Lu, J. T. J. Yates: Photocatalysis on TiO_2 surfaces: Principles, mechanisms, and selected results.
Chem. Rev. **95**, 735 (1995)

74. A. Fujishima, K. Honda: Electrochemical photolysis of water at a semiconductor electrode.
Nature **238**, 37 (1972)

75. F. A. Grant: Properties of rutile (titanium dioxide).
Rev. Mod. Phys. **31**, 646 (1959)

76. S. C. Abrahams, J. L. Bernstein: Rutile: normal probability plot analysis and accurate measurement of crystal structure.
J. Chem. Phys. **55**, 3206 (1971)

77. S. Wendt, R. Schaub, J. Matthiesen, E. K. Vestergaard, E. Wahlström, M. D. Rasmussen, P. Thostrup, L. M. Molina, E. Lægsgaard, I. Stensgaard, B. Hammer, F. Besenbacher: Oxygen vacancies on TiO_2(110) and their interaction with H_2O and O_2: A combined high-resolution STM and DFT study.
Surf. Sci. **598**, 226 (2005)

78. S. Wendt, J. Matthiesen, R. Schaub, E. K. Vestergaard, E. Lægsgaard, F. Besenbacher, B. Hammer: Formation and splitting of paired hydroxyl groups on reduced TiO_2(110).
Phys. Rev. Lett. **96**, 066107 (2006)

79. Z. Zhang, O. Bondarchuk, B. D. Kay, J. M. White, Z. Dohnalek: Imaging water dissociation on TiO_2(110): Evidence for inequivalent geminate OH groups.
J. Phys. Chem. B **110**, 21840 (2006)

80. M. Henderson, W. Epling, C. Peden, C. Perkins: Insights into photoexcited electron scavenging processes on TiO_2 obtained from studies of the reaction of O_2 with oh groups adsorbed at electronic defects on TiO_2(110).
J. Phys. Chem. B **107**, 534 (2003)

81. J. V. Lauritsen, A. S. Foster, G. H. Olesen, M. C. Christensen, A. Kühnle, S. Helveg, J. R. Rostrup-Nielsen, B. S. Clausen, M. Reichling, F. Besenbacher: Chemical identification of point defects and adsorbates on a metal oxide surface by atomic force microscopy.
Nanotechnology **17**, 3436 (2006)

82. G. H. Enevoldsen, A. S. Foster, M. C. Christensen, J. V. Lauritsen, F. Besenbacher: Noncontact atomic force microscopy studies of vacancies and hydroxyls of TiO_2(110): Experiments and atomistic simulations.
Phys. Rev. B **76**, 205415 (2007)

83. R. Bechstein, C. González, J. Schütte, P. Jelínek, R. Pérez, A. Kühnle: 'All-inclusive' imaging of the rutile TiO_2(110) surface using NC-AFM.
Nanotechnology **20**, 505703 (2009)

84. A. Yurtsever, Y. Sugimoto, M. Abe, S. Morita: NC-AFM imaging of the TiO_2(110)-(1×1) surface at low temperature.
Nanotechnology **21**, 165702 (2010)

85. NC-AFM images (a), (c) and (d) used with permission from .

86. M. Letz, L. Parthier: Charge centers in CaF_2: Ab initio calculation of elementary physical properties.
Phys. Rev. B **74**, 064116 (2006)

87. A. M. Stoneham: Dislocation-induced birefringence in CaF_2 for lithography optics.
Semicond. Sci. Tech. **17**, L15 (2002)

88. R. W. G. Wyckoff: Crystal Structures Vol. 1. 2nd Edition. John Wiley & Sons, New York, London, 1963

89. L. Tröger, J. Schütte, F. Ostendorf, A. Kühnle, M. Reichling: Concept for support and cleavage of brittle crystals.
Rev. Sci. Instrum. **80**, 063703 (2009)

90. M. Reichling, M. Huisinga, S. Gogoll, C. Barth: Degradation of the CaF_2(111) surface by air exposure.
Surface Science **439**, 181 (1999)

91. M. Reichling, C. Barth: Scanning force imaging of atomic size defects on the CaF_2 (111) surface.
Phys. Rev. Lett. **83**, 768 (1999)

92. P. W. Tasker: Stability of ionic-crystal surfaces.
J. Phys. C **12**, 4977 (1979)

93. A. S. Foster, C. Barth, A. L. Shluger, M. Reichling: Unambiguous interpretation of atomically resolved force microscopy images of an insulator.
Phys. Rev. Lett. **86**, 2373 (2001)

94. C. Barth, A. S. Foster, M. Reichling, A. L. Shluger: Contrast formation in atomic resolution scanning force microscopy on CaF_2(111): experiment and theory.
J. Phys. Condens. Matter **13**, 2061 (2001)

95. A. S. Foster, C. Barth, A. L. Shluger, R. M. Nieminen, M. Reichling: Role of tip structure and surface relaxation in atomic resolution dynamic force microscopy. CaF_2(111) as a reference surface.
Phys. Rev. B **66**, 235417 (2002)

96. H. W. Kroto, J. R. Heath, S. C. O'Brien, R. F. Curl, R. E. Smalley: C_{60}: Buckminsterfullerene.
Nature **318**, 162 (1985)

97. G. A. Samara, J. E. Schirber, B. Morosin, L. V. Hansen, D. Loy, A. P. Sylwester: Pressure dependence of the orientational ordering in solid C_{60}.
Phys. Rev. Lett. **67**, 3136 (1991)

98. W. Krätschmer, L. D. Lamb, K. Fostiropoulos, D. R. Huffman: Solid C_{60}: a new form of carbon.
Nature **347**, 354 (1990)

99. P. A. Heiney, J. E. Fischer, A. R. McGhie, W. J. Romanow, A. M. Denenstein, J. P. McCauley Jr., A. B. Smith, D. E. Cox: Orientational ordering transition in solid C_{60}.
Phys. Rev. Lett. **66**, 2911 (1991)

100. C. S. Yannoni, R. D. Johnson, G. Meijer, D. S. Bethune, J. R. Salem: 13C NMR-study of the C_{60} cluster in the solid-state - molecular-motion and carbon chemical-shift anisotropy.
J. Phys. Chem. **95**, 9 (1991)

101. D. H. Oh, Y. H. Lee: Orientational Ordering of Solid C_{70}.
Phys. Rev. Lett. **75**, 4230 (1995)

102. C. Pan, M. P. Sampson, Y. Chai, R. H. Hauge, J. L. Margrave: Heats of sublimation from a polycrystalline mixture of carbon clusters (C_{60} and C_{70}).
J. Phys. Chem. **95**, 2944 (1991)

103. W. I. F. David, R. M. Ibberson, J. C. Matthewman, K. Prassides, T. J. S. Dennis, J. P. Hare, H. W. Kroto, R. Taylor, D. R. M. Walton: Crystal structure and bonding of ordered carbon cluster C_{60}.
Nature **353**, 147 (1991)

104. E. I. Altman, R. J. Colton: Determination of the orientation of C_{60} adsorbed on Au(111) and Ag(111).
Phys. Rev. B **48**, 18244 (1993)

105. T. Hashizume, K. Motai, X. D. Wang, H. Shinohara, Y. Saito, Y. Maruyama, K. Ohno, Y. Kawazoe, Y. Nishina, H. W. Pickering, Y. Kuk, T. Sakurai: Intramolecular structures of C_{60} molecules adsorbed on the Cu(111)-(1×1) surface.
Phys. Rev. Lett. **71**, 2959 (1993)

106. S. Suto, K. Sakamoto, T. Wakita, M. Harada, A. Kasuya: Interaction of C_{60} with silicon dangling bonds on the Si(111)-(7×7) surface.
Surf. Sci. **402-404**, 523 (1998)

107. K. Kobayashi, H. Yamada, T. Horiuchi, K. Matsushige: Investigations of C_{60} molecules deposited on Si(111) by noncontact atomic force microscopy.
Appl. Surf. Sci. **140**, 281 (1999)

108. S. A. Burke, J. M. Mativetsky, S. Fostner, P. Grütter: C_{60} on alkali halides: Epitaxy and morphology studied by noncontact AFM.
Phys. Rev. B **76**, 035419 (2007)

109. K. Fukui, M. Sakai: Formation of one-dimensional C_{60} rows on $TiO_2$110)-1x2-cross-link structure and their local polymerization.
J. Phys. Chem. B **110**, 21118 (2006)

110. A. J. Maxwell, P. A. Brühwiler, D. Arvanitis, J. Hasselström, M. K.-J. Johansson, N. Mårtensson: Electronic and geometric structure of C_{60} on Al(111) and Al(110).
Phys. Rev. B **57**, 7312 (1998)

111. S. A. Burke, J. M. Mativetsky, R. Hoffmann, P. Grütter: Nucleation and submonolayer growth of C_{60} on KBr.
Phys. Rev. Lett. **94**, 096102 (2005)

112. H. Xu, D. M. Chen, W. N. Creager: Double domain solid C_{60} on Si(111)7×7.
Phys. Rev. Lett. **70**, 1850 (1993)

113. K. Kobayashi, H. Yamada, T. Horiuchi, K. Matsushige: Structures and electrical properties of fullerene thin films on Si(111)-7×7 surface

investigated by noncontact atomic force microscopy.
Jap. J. Appl. Phys. **39**, 3827 (2000)

114. K. Kobayashi, H. Yamada, T. Horiuchi, K. Matsushige: Imaging of fullerene molecules on Si(111)-7×7 surface with NC-AFM.
Appl. Surf. Sci. **157**, 228 (2000)

115. S. Suto, K. Sakamoto, T. Wakita, C.-W. Hu, A. Kasuya: Vibrational properties and charge transfer of C_{60} adsorbed on Si(111)-(7×7) and Si(100)-(2×1) surfaces.
Phys. Rev. B **56**, 7439 (1997)

116. A. Meller, A. Ossko: Phthalocyaninartige Bor-Komplexe.
Monatsh. Chem. **103**, 150 (1972)

117. H. Kietaibl: Crystal and molecular-structure of a new phthalocyanine-like boron complex.
Monatsh. Chem. **105**, 405 (1974)

118. M. K. Engel, J. Yao, H. Maki, H. Takeuchi, H. Yonehar, C. Pac: Synthesis, structural characterization and optical properties of several boron subphthalocyanines and a boron beta-isoindigo complex.
Kaw. Rik. Ken. Hok. **11**, 53 (1997)

119. S. Berner, M. de Wild, L. Ramoino, S. Ivan, A. Baratoff, H. J. Güntherodt, H. Suzuki, D. Schlettwein, T. A. Jung: Adsorption and two-dimensional phases of a large polar molecule: Sub-phthalocyanine on Ag(111).
Phys. Rev. B **68**, 115410 (2003)

120. V. R. Ferro, L. A. Poveda, R. H. González-Jonte, J. M. G. De la Vega, T. Torres, B. Del Rey: Molecular electronic structure of subphthalocyanine macrocycles.
J. Porphy. Phthalocyan. **4**, 610 (2000)

121. L. Nony, E. Gnecco, A. Baratoff, A. Alkauskas, R. Bennewitz, O. Pfeiffer, S. Maier, A. Wetzel, E. Meyer, C. Gerber: Observation of individual molecules trapped on a nanostructured insulator.
Nano Letters **4**, 2185 (2004)

122. H. Yanagi, K. Ikuta, H. Mukai, T. Shibutani: STM-induced flip-flop switching of adsorbed subphthalocyanine molecular arrays.
Nano Letters **2**, 951 (2002)

123. H. Yanagi, K. Ikuta: Stochastic switching of subphthalocyanine arrays triggered by scanning tunneling microscopy.
Surf. Sci. **581**, 9 (2005)

124. H. Yanagi, D. Schlettwein, H. Nakayama, T. Nishino: Site-specific physisorption and chemical reaction of subphthalocyanine molecules on silicon(111)-(7×7).
Phys. Rev. B **61**, 1959 (2000)

125. N. Jiang, Y. L. Wang, Q. Liu, Y. Y. Zhang, Z. T. Deng, K. H. Ernst, H. J. Gao: Polymorphism and chiral expression in two-dimensional subphthalocyanine crystals on Au(111).
Phys. Chem. Chem. Phys. **12**, 1318 (2010)

126. S. Mannsfeld, H. Relchhard, T. Fritz: LEED and STM investigation of chloro(subphthalocyaninato)boron on Au(111).
Surf. Sci. **525**, 215 (2003)

127. H. Suzuki, S. Berner, M. Brunner, H. Yanagi, D. Schlettwein, T. A. Jung, H. J. Güntherodt: Characterization of molecular overlayers on metal surface in dynamic equilibrium by scanning tunneling microscope.
Thin Solid Films **393**, 325 (2001)

128. S. Berner, M. Brunner, L. Ramoino, H. Suzuki, H. J. Güntherodt, T. A. Jung: Time evolution analysis of a 2D solid-gas equilibrium: a model system for molecular adsorption and diffusion.
Chem. Phys. Lett. **348**, 175 (2001)

129. M. De Wild, S. Berner, H. Suzuki, H. Yanagi, D. Schlettwein, S. Ivan, A. Baratoff, H.-J. Güntherodt, T. A. Jung: A novel route to molecular self-assembly. Self-intermixed monolayer phases.
ChemPhysChem **3**, 881 (2002)

130. V. Petrauskas, S. Lapinskas, E. E. Tornau: Phase diagram of subphtalocyanine ordering on Ag(111).
J. Chem. Phys. **120**, 11815 (2004)

131. G. Klebe: 3,4:9,10-Perylene-bis(dicarboximide).
Data deposited at the CCDC (1994)

132. K. Tojo, J. Mizuguchi: Structure of 3,4:9,10-perylene-bis(dicarboximide).
Z. Kristallogr. New Cryst. Struct. **217**, 45 (2002)

133. O. Guillermet, M. Mossoyan-Déneux, M. Giorgi, A. Glachant, J. C. Mossoyan: Structural study of vapour phase deposited 3,4,9,10-perylene tetracarboxylicacid diimide: Comparison between single crystal and ultra thin films grown on Pt(100).
Thin Solid Films **514**, 25 (2006)

134. M. Mura, F. Silly, G. A. D. Briggs, M. R. Castell, L. N. Kantorovich: H-bonding supramolecular assemblies of PTCDI molecules on the Au(111) surface.
J. Phys. Chem. C **113**, 21840 (2009)

135. J. M. Topple, S. A. Burke, S. Fostner, P. Grütter: Thin film evolution: Dewetting dynamics of a bimodal molecular system.
Phys. Rev. B **79**, 205414 (2009)

136. F. Silly, A. Q. Shaw, M. R. Castell, G. A. D. Briggs: A chiral pin-wheel supramolecular network driven by the assembly of PTCDI and melamine.
Chem. Comm. **2008**, 1907 (2008)

137. M. E. Cañas Ventura, W. Xiao, D. Wasserfallen, K. Müllen, H. Brune, J. V. Barth, R. Fasel: Self-assembly of periodic bicomponent wires and ribbons.
Angew. Chem. Int. **46**, 1814 (2007)

138. C. Ludwig, B. Gompf, J. Petersen, R. Strohmaier, W. Eisenmenger: STM investigations of PTCDA and PTCDI on graphite and MoS_2 - a systematic study of epitaxy and STM image-contrast.
Z. Phys. B **93**, 365 (1994)

139. O. Guillermet, A. Glachant, J. Y. Hoarau, J. C. Mossoyan, M. Mossoyan: Perylene tetracarboxylic diimide ultrathin film deposition on Pt(100): a LEED, AES, REELS and STM study.
Surf. Sci. **548**, 129 (2004)

140. K. Aït-Mansour, M. Treier, P. Ruffieux, M. Bieri, R. Jaafar, P. Gröning, R. Fasel, O. Gröning: Template-directed molecular nanostructures on the Ag/Pt(111) dislocation network.
J. Phys. Chem. C **113**, 8407 (2009)

141. J. C. Swarbrick, J. Ma, J. A. Theobald, N. S. Oxtoby, J. N. O'Shea, N. R. Champness, P. H. Beton: Square, hexagonal, and row Phases of PTCDA and PTCDI on Ag-Si(111)$\sqrt{3} \times \sqrt{3}$R30°.
J. Phys. Chem. B **109**, 12167 (2005)

142. B. Uder, C. Ludwig, J. Petersen, B. Gompf, W. Eisenmenger: STM characterization of organic-molecules on H-terminated Si(111).
Z. Phys. B **97**, 389 (1995)

143. C. W. Tang: Two-layer organic photovoltaic cell.
Appl. Phys. Lett. **48**, 183 (1986)

144. S. R. Forrest: The path to ubiquitous and low-cost organic electronic appliances on plastic.
Nature **428**, 911 (2004)

145. P. Zahl, M. Bammerlin, G. Meyer, R. R. Schlittler: All-in-one static and dynamic nanostencil atomic force microscopy/scanning tunneling microscopy system.
Rev. Sci. Instrum. **76**, 023707 (2005)

146. J. M. Mativetsky, S. A. Burke, R. Hoffmann, Y. Sun, P. Grütter: Molecular resolution imaging of C_{60} on Au(111) by non-contact atomic force microscopy.
Nanotechnology **15**, 40 (2004)

147. A. S. Foster, W. A. Hofer, A. L. Shluger: Quantitative modelling in scanning probe microscopy.
Curr. Opin. Solid State Mater. Sci. **5**, 427 (2001)

148. A. I. Livshits, A. L. Shluger, A. L. Rohl, A. S. Foster: Model of non-contact scanning force microscopy on ionic surfaces.
Phys. Rev. B **59**, 2436 (1999)

149. M. Abe, Y. Sugimoto, O. Custance, S. Morita: Room-temperature reproducible spatial force spectroscopy using atom-tracking technique.
Appl. Phys. Lett. **87**, 173503 (2005)

150. P. Rahe: Adsorptionseigenschaften von organischen Molekülen auf Titandioxid untersucht mit hochauflösender Rasterkraftmikroskopie, Universität Osnabrück, Diploma thesis, 2008

151. F. Loske, P. Rahe, A. Kühnle: Contrast inversion in non-contact atomic force microscopy imaging of C_{60} molecules.
Nanotechnology **20**, 264010 (2009)

152. H. Hölscher, A. Schwarz, W. Allers, U. D. Schwarz, R. Wiesendanger: Quantitative analysis of dynamic-force-spectroscopy data on graphite(0001) in the contact and noncontact regimes.
Phys. Rev. B **61**, 12678 (2000)

153. L. Bartels, G. Meyer, K. H. Rieder: Basic steps of lateral manipulation of single atoms and diatomic clusters with a scanning tunneling microscope tip.
Phys. Rev. Lett. **79**, 697 (1997)

154. A. J. Heinrich, C. P. Lutz, J. A. Gupta, D. M. Eigler: Molecule Cascades.
Science **298**, 1381 (2002)

155. N. Martsinovich, L. Kantorovich, R. H. J. Fawcett, M. J. Humphry, P. H. Beton: Constrained molecular manipulation mediated by attractive and repulsive tip-adsorbate forces.
Small **4**, 765 (2008)

156. Y. Sugimoto, M. Abe, S. Hirayama, N. Oyabu, O. Custance, S. Morita: Atom inlays performed at room temperature using atomic force microscopy.
Nat. Mater. **4**, 156 (2005)

157. Y. Sugimoto, P. Pou, O. Custance, P. Jelinek, M. Abe, R. Pérez, S. Morita: Complex patterning by vertical interchange atom manipulation using atomic force microscopy.
Science **322**, 413 (2008)

158. S. Morita, Y. Sugimoto, N. Oyabu, R. Nishi, O. Custance, Y. Sugawara, M. Abe: Atom-selective imaging and mechanical atom manipulation using the non-contact atomic force microscope.
J. Electron Microsc. **53**, 163 (2004)

159. R. Nishi, D. Miyagawa, Y. Seino, I. Yi, S. Morita: Non-contact atomic force microscopy study of atomic manipulation on an insulator surface by nanoindentation.
Nanotechnology **17**, S142 (2006)

160. S. Kawai, H. Kawakatsu: Mechanical atom manipulation with small amplitude dynamic force microscopy.
Appl. Phys. Lett. **89**, 023113 (2006)

161. N. Martsinovich, L. Kantorovich: Modelling the manipulation of C_{60} on the Si(001) surface performed with NC-AFM.
Nanotechnology **20**, 135706 (2009)

162. T. Trevethan, M. Watkins, L. N. Kantorovich, A. L. Shluger, J. Polesel-Maris, S. Gauthier: Modelling atomic scale manipulation with the non-contact atomic force microscope.
Nanotechnology **17**, 5866 (2006)

163. T. Trevethan, L. Kantorovich, J. Polesel-Maris, S. Gauthier, A. Shluger: Multiscale model of the manipulation of single atoms on insulating surfaces using an atomic force microscope tip.
Phys. Rev. B **76**, 085414 (2007)

164. N. Oyabu, Y. Sugimoto, M. Abe, O. Custance, S. Morita: Lateral manipulation of single atoms at semiconductor surfaces using atomic force microscopy.
Nanotechnology **16**, S112 (2005)

165. S. Fölsch, T. Maruno, A. Yamashita, T. Hayashi: Epitaxial C_{60} films on CaF_2(111) grown by molecular-beam deposition.
Appl. Phys. Lett. **62**, 2643 (1993)

166. S. Fölsch, T. Maruno, A. Yamashita, T. Hayashi: Structural-properties of heteroepitaxial C_{60} films on CaF_2(111).
Surf. Sci. **294**, L959 (1993)

167. P. Rahe, R. Bechstein, A. Kühnle: Vertical and lateral drift corrections of scanning probe microscopy images.
J. Vac. Sci. Technol. B **28**, C4E31 (2010)

168. G. Beernink, T. Strunskus, G. Witte, C. Wöll: Importance of dewetting in organic molecular-beam deposition: Pentacene on gold.
Appl. Phys. Lett. **85**, 398 (2004)

169. A. C. Dürr, F. Schreiber, K. A. Ritley, V. Kruppa, J. Krug, H. Dosch, B. Struth: Rapid roughening in thin film growth of an organic semiconductor (diindenoperylene).
Phys. Rev. Lett. **90**, 016104 (2003)

170. D. Käfer, C. Wöll, G. Witte: Thermally activated dewetting of organic thin films: the case of pentacene on SiO_2 and gold.
Appl. Phys. A **95**, 273 (2009)

171. B. Krause, A. C. Dürr, F. Schreiber, H. Dosch, O. H. Seeck: Thermal stability and partial dewetting of crystalline organic thin films: 3,4,9,10-perylenetetracarboxylic dianhydride on Ag(111).
J. Chem. Phys. **119**, 3429 (2003)

172. S. Rath, H. Port: Dewetting of thin UHV-deposited organic films.
Chem. Phys. Lett. **421**, 152 (2006)

173. G. Witte, K. Hanel, S. Söhnchen, C. Wöll: Growth and morphology of thin films of aromatic molecules on metals: the case of perylene.
Appl. Phys. A **82**, 447 (2006)

174. R. Lüthi, H. Haefke, E. Meyer, L. Howald, H. P. Lang, G. Gerth, H. J. Güntherodt: Frictional and atomic-scale study of C_{60} thin-films by scanning force microscopy.
Z. Phys. B **95**, 1 (1994)

175. Y. Kim, L. Jiang, T. Iyoda, K. Hashimoto, A. Fujishima: AFM study of surface phenomena based on C_{60} film growth.
Appl. Surf. Sci. **130**, 602 (1998)

176. S. A. Burke, W. Ji, J. M. Mativetsky, J. M. Topple, S. Fostner, H. J. Gao, H. Guo, P. Grütter: Strain induced dewetting of a molecular system: Bimodal growth of PTCDA on NaCl.
Phys. Rev. Lett. **100**, 186104 (2008)

177. T. Dienel, C. Loppacher, S. C. B. Mannsfeld, R. Forker, T. Fritz: Growth-mode-induced narrowing of optical spectra of an organic adlayer.
Adv. Mater. **20**, 959 (2008)

178. M. Fendrich, M. Lange, C. Weiss, T. Kunstmann, R. Möller: N,N'-dimethylperylene-3,4,9,10-bis(dicarboximide) on alkali halide (001) surfaces.
J. Appl. Phys **105**, 094311 (2009)

179. E. Barrena, D. G. de Oteyza, H. Dosch, Y. Wakayama: 2D supramolecular self-assembly of binary organic monolayers.
ChemPhysChem **8**, 1915 (2007)

180. D. Bonifazi, H. Spillmann, A. Kiebele, M. de Wild, P. Seiler, F. Cheng, J. Güntherodt, T. Jung, F. Diederich: Self-assembly on surfaces: Supramolecular patterned surfaces driven by cooperative assembly of C_{60} and porphyrins on metal substrates.
Angew. Chem. Int. Ed. **43**, 4759 (2004)

181. W. Chen, H. Li, H. Huang, Y. X. Fu, H. L. Zhang, J. Ma, A. T. S. Wee: Two-dimensional pentacene : 3,4,9,10-perylenetetracarboxylic dianhydride supramolecular chiral networks on Ag(111).
J. Am. Chem. Soc. **130**, 12285 (2008)

182. M. De Wild, S. Berner, H. Suzuki, L. Ramoino, A. Baratoff, T. A. Jung: Molecular assembly and self-assembly: molecular nanoscience for future technologies.
Ann. New York Acad. Sci. **1006**, 291 (2003)

183. H. Huang, W. Chen, L. Chen, H. L. Zhang, X. Sen Wang, S. N. Bao, A. T. S. Wee: "Zigzag" C_{60} chain arrays.
Appl. Phys. Lett **92**, 023105 (2008)

184. J. Ma, B. L. Rogers, M. J. Humphry, D. J. Ring, G. Goretzki, N. R. Champness, P. H. Beton: Dianhydride-amine hydrogen bonded perylene tetracarboxylic dianhydride and tetraaminobenzene rows.
J. Phys. Chem. B **110**, 12207 (2006)

185. L. M. A. Perdigão, N. R. Champness, P. H. Beton: Surface self-assembly of the cyanuric acid-melamine hydrogen bonded network.
Chem. Comm. **5**, 538 (2006)

186. L. M. A. Perdigão, G. N. Fontes, B. L. Rogers, N. S. Oxtoby, G. Goretzki, N. R. Champness, P. H. Beton: Coadsorbed NTCDI-melamine mixed phases on Ag-Si(111).
Phys. Rev. B **76**, 245402 (2007)

187. L. M. A. Perdigão, E. W. Perkins, J. Ma, P. A. Staniec, B. L. Rogers, N. R. Champness, P. H. Beton: Bimolecular networks and supramolecular traps on Au(111).
J. Phys. Chem. B **110**, 12539 (2006)

188. L. M. A. Perdigão, P. A. Staniec, N. R. Champness, P. H. Beton: Entrapment of decanethiol in a hydrogen-bonded bimolecular template.
Langmuir **25**, 2278 (2009)

189. M. Ruiz-Osés, N. González-Lakunza, I. Silanes, A. Gourdon, A. Arnau, J. E. Ortega: Self-assembly of heterogeneous supramolecular structures with uniaxial anisotropy.
J. Phys. Chem. **110**, 25573 (2006)

190. L. Sánchez, R. Otero, J. M. Gallego, R. Miranda, N. Martín: Ordering fullerenes at the nanometer scale on solid surfaces.
Chem. Rev. **109**, 2081 (2009)

191. P. A. Staniec, L. M. A. Perdigão, B. L. Rogers, N. R. Champness, P. H. Beton: Honeycomb networks and chiral superstructures formed by cyanuric acid and melamine on Au(111).
J. Phys. Chem. C **111**, 886 (2007)

192. P. A. Staniec, L. M. A. Perdigão, A. Saywell, N. R. Champness, P. H. Beton: Hierarchical organisation on a two-dimensional supramolecular network.
ChemPhysChem **8**, 2177 (2007)

193. M. Stöhr, M. Wahl, H. Spillmann, L. H. Gade, T. A. Jung: Lateral manipulation for the positioning of molecular guests within the confinements of a highly stable self-assembled organic surface network.
Small **3**, 1336 (2007)

194. J. C. Swarbrick, B. L. Rogers, N. R. Champness, P. H. Beton: Hydrogen-bonded PTCDA-melamine networks and mixed phases.
J. Phys. Chem. B **110**, 6110 (2006)

195. J. A. Theobald, N. S. Oxtoby, N. R. Champness, P. H. Beton, T. J. S. Dennis: Growth induced reordering of fullerene clusters trapped in a two-dimensional supramolecular network.
Langmuir **21**, 2038 (2005)

196. J. A. Theobald, N. S. Oxtoby, M. A. Phillips, N. R. Champness, P. H. Beton: Controlling molecular deposition and layer structure with supramolecular surface assemblies.
Nature **424**, 1029 (2003)

197. W. Xiao, D. Passerone, P. Ruffieux, K. Ait-Mansour, O. Gröning, E. Tosatti, J. S. Siegel, R. Fasel: C_{60}/corannulene on Cu(110): A surface-supported bistable buckybowl-buckyball host-guest system.
J. Am. Chem. Soc. **130**, 4767 (2008)

198. B. Xu, C. G. Tao, W. G. Cullen, J. E. Reutt-Robey, E. D. Williams: Chiral symmetry breaking in two-dimensional C_{60}-ACA intermixed systems.
Nano Lett. **5**, 2207 (2005)

199. B. Xu, C. G. Tao, E. D. Williams, J. E. Reutt-Robey: Coverage dependent supramolecular structures: C_{60}:ACA monolayers on Ag(111).
J. Am. Chem. Soc. **128**, 8493 (2006)

200. H. L. Zhang, W. Chen, L. Chen, H. Huang, X. S. Wang, J. Yuhara, A. T. S. Wee: C_{60} molecular chains on a-sexithiophene nanostripes.
Small **3**, 2015 (2007)

201. H. L. Zhang, W. Chen, H. Huang, L. Chen, A. T. S. Wee: Preferential trapping of C_{60} in nanomesh voids.
J. Am. Chem. Soc. **130**, 2720 (2008)

202. N. A. A. Zwaneveld, R. Pawlak, M. Abel, D. Catalin, D. Gigmes, D. Bertin, L. Porte: Organized formation of 2D extended covalent organic frameworks at surfaces.
J. Am. Chem. Soc. **130**, 6678 (2008)

203. M. O. Blunt, J. C. Russell, N. R. Champness, P. H. Beton: Templating molecular adsorption using a covalent organic framework.
Chem. Comm. **46**, 7157 (2010)

204. A. G. Phillips, L. M. A. Perdigão, P. H. Beton, N. R. Champness: Tailoring pores for guest entrapment in a unimolecular surface self-assembled hydrogen bonded network.
Chem. Comm. **46**, 2775 (2010)

205. X. N. Sun, H. T. Jonkman, F. Silly: Tailoring two-dimensional PTCDA-melamine self-assembled architectures at room temperature by tuning molecular ratio.
Nanotechnology **21**, 165602 (2010)

206. K. Tahara, S. B. Lei, J. Adisoejoso, S. De Feyter, Y. Tobe: Supramolecular surface-confined architectures created by self-assembly of triangular phenylene-ethynylene macrocycles via van der Waals interaction.
Chem. Comm. **46**, 8507 (2010)

Publications

Publications in peer-reviewed journals

- **Growth of ordered C_{60} islands on TiO_2 (110)**
  F. Loske, R. Bechstein, J. Schütte, F. Ostendorf, M. Reichling, A. Kühnle
  Nanotechnology **20**, 065606 (2009)

- **Contrast inversion in non-contact atomic force microscopy imaging of C_{60} molecules**
  F. Loske, P. Rahe, A. Kühnle
  Nanotechnology **20**, 264010 (2009)

- **Manipulation of C_{60} islands on the rutile TiO_2 (110) surface using non-contact atomic force microscopy**
  F. Loske, A. Kühnle
  Applied Physics Letters **95**, 043110 (2009)

- **Quantitative description of C_{60} diffusion on an insulating surface**
  F. Loske, J. Lübbe, J. Schütte, M. Reichling, A. Kühnle
  Physical Review B **82**, 155428 (2010)

Web publications

- **Creating molecular nano-structures**
  F. Loske, R. Bechstein, J. Schütte, F. Ostendorf, M. Reichling, A. Kühnle
  Lab Talk on nanotechweg.org (2009)
  Web address: http://nanotechweb.org/cws/article/lab/37553

- **Contrast inversion in non-contact atomic force microscopy imaging of C_{60} molecules**
  F. Loske, P. Rahe, A. Kühnle
  Result of the Month on omicron.de (2009)
  Web address: http://www.omicron.de/results/microscopy_imaging_c60

Conference contributions

Talks

(presenting author is underlined)

- **Growth of C_{60} islands on TiO_2 (110)**
  F. Loske, R. Bechstein, F. Ostendorf, M. Reichling, A. Kühnle
  72th DPG Frühjahrstagung (2008), Berlin (Germany)
- **Repulsive interaction and contrast inversion in NC-AFM imaging of adsorbates**
  P. Rahe, R. Bechstein, J. Schütte, F. Ostendorf, F. Loske, A. Kühnle
  11th International Conference on NC-AFM (2008), Madrid (Spain)
- **Modification of C_{60} islands on the rutile TiO_2 (110) surface using non-contact atomic force microscopy**
  F. Loske, A. Kühnle
  1st European Nanomanipulation Workshop (2010), Cascais (Portugal)

Posters

- **Growth of C_{60} islands on TiO_2 (110) investigated by NC-AFM**
  F. Loske, F. Ostendorf, M. Reichling, A. Kühnle
  1st Workshop Towards Reality in Nanoscale Materials (2007), Levi (Finnland)
- **Growth and manipulation of C_{60} islands on TiO_2 (110)**
  F. Loske, F. Ostendorf, M. Reichling, A. Kühnle
  11th International Conference on NC-AFM (2008), Madrid (Spain)
- **Temperature-dependent growth of C_{60} on CaF_2 (111)**
  F. Loske, J. Schütte, A. Kühnle
  12th International Conference on NC-AFM (2009), Yale (USA)

- **Bucky ball island morphologies on CaF_2 (111): theory and experiment**
  M. Körner, F. Loske, M. Einax, A. Kühnle, P. Maaß
  75th DPG Frühjahrstagung (2010), Dresden (Germany)
- **Noise figures of optimised, cantilever-based NC-AFM systems for high resolution imaging in the ultra-high vacuum**
  J. Lübbe, F. Loske, A. Kühnle, M. Reichling
  13th International Conference on NC-AFM (2010), Kanazawa (Japan)
- **Comparison of tapping and FM-AFM in various environments**
  S. Rode, F. Loske, M. Reichling, A. Kühnle
  13th International Conference on NC-AFM (2010), Kanazawa (Japan)

Acknowledgements

Removed to protect privacy.

Curriculum vitae (educational)

Removed to protect privacy.